Vol. 47, No. 6
June 2025

ISSN 1024-1809

METALLOPHYSICS and ADVANCED TECHNOLOGIES

МЕТАЛОФІЗИКА ТА НОВІТНІ ТЕХНОЛОГІЇ

METALLOFIZIKA I NOVEISHIE TEKHNOLOGII

Том 47, № 6 (2025)

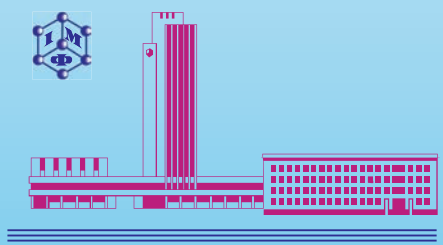

G.V. Kurdyumov Institute for Metal Physics
National Academy of Sciences of Ukraine
https://mfint.imp.kiev.ua

Засновник: Національна академія наук України, Інститут металофізики ім. Г. В. Курдюмова НАН України
Видавець: ВД «Академперіодика» НАН України

«Металофізика та новітні технології» ● **'Metallophysics and Advanced Technologies'**

Щомісячний науковий журнал ○ A Monthly Research Journal

NATIONAL ACADEMY OF SCIENCES OF UKRAINE ● G. V. KURDYUMOV INSTITUTE FOR METAL PHYSICS

A MONTHLY RESEARCH JOURNAL

METALLOPHYSICS AND ADVANCED TECHNOLOGIES

(Metallofizika i Noveishie Tekhnologii)

FOUNDED IN SEPTEMBER, 1979

Volume 47, No. 6; June 2025

CONTENTS

CONTENTS, No. 6 (Vol. 47)

Scientific Editors of Issue—*O. S. Gatsenko, V. A. Tatarenko*
Executive Managing Editor—*O. S. Gatsenko*
Editors—*L. I. Makarenko, M. V. Manilo, I. V. Zagorulko*
The artwork for direct reproduction is made by computer group of EPD of the G. V. Kurdyumov Institute for Metal Physics, N.A.S. of Ukraine

Editorial Office Address:
G. V. Kurdyumov Institute for Metal Physics, N.A.S. of Ukraine, EPD—'MNT',
36 Academician Vernadsky Boulevard, UA-03142 Kyiv, Ukraine
Telephone: +380 44 4249042. Fax: +380 44 4242561. E-mail: mfint@imp.kiev.ua
Media Identifier R30-03171

Approved for publication by the Academic Council of the G. V. Kurdyumov Institute for Metal Physics of the National Academy of Sciences of Ukraine
Published in English or Ukrainian languages according to resolution of Editorial Board of the journal

Printed by Publishing House 'Akademperiodyka', of the NAS of Ukraine
4 Tereshchenkivs'ka Str., UA-01024 Kyiv, Ukraine
Registration Certificate of Publishing Subject: ДК № 544 on 27.07.2001

Journal website: http://mfint.imp.kiev.ua
Journal DOI: https://doi.org/10.15407/mfint

Issue DOI: https://doi.org/10.15407/mfint.47.06

НАЦІОНАЛЬНА АКАДЕМІЯ НАУК УКРАЇНИ ● ІНСТИТУТ МЕТАЛОФІЗИКИ ім. Г. В. Курдюмова

МЕТАЛОФІЗИКА ТА НОВІТНІ ТЕХНОЛОГІЇ

ЩОМІСЯЧНИЙ НАУКОВИЙ ЖУРНАЛ
ЗАСНОВАНИЙ У ВЕРЕСНІ 1979 р.

Том 47, № 6; червень, 2025

ЗМІСТ

Наукові редактори випуску: *О. С. Гаценко, В. А. Татаренко*
Відповідальний секретар редакційної колеґії *О. С. Гаценко*
Редактор-коректор *О. С. Гаценко*
Технічні редактори: *І. В. Загорулько, Л. І. Макаренко, М. В. Маніло*
Художні редактори: *І. В. Загорулько, Л. І. Макаренко, М. В. Маніло*
Оригінал-макет для прямого репродукування виготовлено комп'ютерною групою РВВ Інституту металофізики ім. Г. В. Курдюмова НАН України

Адреса редакції:
Інститут металофізики ім. Г. В. Курдюмова НАН України, РВВ—Редакція «МНТ»
бульв. Акад. Вернадського, 36; 03142 Київ, Україна
Тел.: +380 44 4249042; факс: +380 44 4242561
Ел. пошта: mfint@imp.kiev.ua
Ідентифікатор медіа R30-03171

Затверджено до друку вченою радою Інституту металофізики ім. Г. В. Курдюмова НАН України
Друкується за постановою редакційної колеґії журналу англійською або українською мовами

Підписано до друку 10.07.2025 р. Формат 70×100/16.
Ум. друк. арк. 8,78. Обл.-вид. арк. 8,07.
Тираж 57 пр. Зам. № 7719 від 27.06.2025 р.

Віддруковано ВД «Академперіодика» НАН України
вул. Терещенківська, 4; 01024 Київ, Україна
Свідоцтво суб'єкта видавничої справи ДК № 544 від 27.07.2001 р.

Сайт журналу: http://mfint.imp.kiev.ua
DOI (журналу): https://doi.org/10.15407/mfint

DOI (випуску): https://doi.org/10.15407/mfint.47.06

INFORMATION (GUIDELINES) FOR CONTRIBUTORS

Submission of Manuscripts: Manuscripts should be sent by e-mail (mfint@imp.kiev.ua). Additionally, they can be sent by regular mail to Executive Managing Editor, Editorial Office, G. V. Kurdyumov Institute for Metal Physics, N.A.S. of Ukraine, 36 Academician Vernadsky Boulevard, UA-03142 Kyiv, Ukraine. Manuscripts may also be submitted to a member of the Editorial Advisory Board or to the appropriate Regional Editor who is familiar with the research presented.
Submission of a paper to '*Metallophysics and Advanced Technologies*' (transliteration: '*Metallofizika i Noveishie Tekhnologii*', *i.e.*, '*MfNT*') will be taken to imply that it represents original work not previously published, that it is not being considered for publication elsewhere, and that, if accepted for publication, it will not be republished without the consent of the Editors and Publisher. It is a condition of acceptance by the Editor of a manuscript for publication that the Publishers acquire automatically the copyright in the manuscript throughout the world. Journal '*MfNT*' supports the generally accepted principles described in documents on publication ethics and unacceptable practices, which are presented on the journal website.
Scope of the Journal: *Electronic Structure and Properties, Crystal-Lattice Defects, Phase Transformations, Physics of Strength and Plasticity, Metallic Surfaces and Films, Structure and Properties of Nanoscale and Mesoscopic Materials, Amorphous and Liquid States, Interactions of Radiation and Particles with Condensed Matter, Materials in Extremal Conditions, Reactor and Aerospace Metals Science, Medical Metals Science, New Metallic Materials and Synthetic Metals, Metal-Containing Smart Materials, Physical and Technical Basis of Experiment and Diagnostics, Articles under Discussion*.
Language: The language of publication may be English (preferably) or Ukrainian.
Abstract: Each paper requires an abstract of 200–250 words summarizing the significant coverage and findings (the use of mathematical symbols and expressions in abstract is not recommended).
Keywords and PACS numbers: 5–7 keywords and PACS numbers reflecting the content of the contribution should be supplied (see 'Physics and Astronomy Classification Scheme 2010').
Manuscript Preparation: Papers should be formatted according to the template, which can be downloaded from the Journal's website. The length of **research papers** should not in general exceed 5000 words and 10 figures; **review articles** should not exceed 10000 words and 30 figures, including tables and diagrams. Authors are urged to arrange the subject matter clearly under headings such as: 1. Introduction, 2. Experimental/Theoretical Details, 3. Results, 4. Discussion, 5. Conclusion, References. Subsections should be identified with section and subsection numbers (such as 6.1. Second-Value Subheading).
References and Notes: Notes are indicated in the text by consecutive superior Arabic numbers (without parentheses). References should be numbered consecutively (in square brackets) throughout the text. The full list should be collected and typed at the end of the paper in numerical order. Listed references should be completed in all details including **DOI** (if available) but excluding article titles in journals. **All authors'** initials should precede their names. Examples of references preparation:

1. S. O. Firstov and T. G. Rogul, *Metallofiz. Noveishie Tekhnol.*, **44**, No. 1: 127 (2022) (in Ukrainian). https://doi.org/10.15407/mfint.44.01.0127
2. V. B. Tarelnyk, O. P. Gaponova, and Ye. V. Konoplianchenko, *Prog. Phys. Met.*, **23**, No. 1: 27 (2022). https://doi.org/10.15407/ufm.23.01.027
3. A. Meisel, G. Leonhardt, and R. Szargan, *Röntgenspektren und Chemische Bindung* [X-Ray Spectra and Chemical Bond] (Leipzig: Akademische Verlagsgesellschaft Geest & Portig K.-G.: 1977) (in German).
4. J. M. Ziman, *Printsipy Teorii Tverdogo Tela* [Principles of the Theory of Solids] (Moscow: Mir: 1974) (Russian translation).
5. M. A. Stucke, D. M. Dimiduk, and D. M. Hazzledine, *High Temperature Ordered Intermetallic Alloys. V* (Eds. I. Baker and R. Darolia) (Pittsburgh, PA, USA: MRS: 1993), p. 471.
6. *Handbook of Mathematical Functions with Formulas, Graphs and Mathematical Tables* (Eds. M. Abramowitz and I. A. Stegun), Nat'l Bureau of Standards. Appl. Math. Ser. Vol. **55** (Washington, D.C.: U.S. Govt. Printing Office: 1964).
7. B. B. Karpovych and O. B. Borovkoff, *Proc. of Symp.* '*Micromaterials Engineering*' *(Dec. 25–31, 1999)* (Kyiv: RVV IMF: 2000), vol. **2**, p. 113 (in Russian).
8. A. E. Krug, *Abstr. Int. Conf. Phys. Phenomena (Dec. 25–31, 1991, Alushta)* (Kharkiv: 1991), p. 12.
9. T. M. Radchenko, *Vplyv Uporyadkuvannya Defektnoyi Struktury на Transportni Vlastyvosti Zmishanykh Krystaliv* [Influence of Ordering of the Defect Structure on Transport Properties of the Mixed Crystals] (Thesis of Disser. for the Degree of Dr. Phys.-Math. Sci.) (Kyiv: G. V. Kurdyumov Institute for Metal Physics, N.A.S.U.: 2015) (in Ukrainian). https://doi.org/10.13140/RG.2.2.35430.22089

10. E. M. Gololobov, V. B. Shipilo, N. I. Sedrenok, and A. I. Dudyak, *Sposob Polucheniya Karbonitridov Metallov* [Production Method of Metal Carbonitrides], Authors' Certificate 722341 SSSR (Publ. November 21, 1979) (in Russian).
11. V. G. Trubachev, K. V. Chuistov, V. N. Gorshkov, and A. E. Perekos, *Sposob Polucheniya Metallicheskikh Poroshkov* [The Technology of Metallic Powder Production]: Patent 1639892 SU. MKI, B22 F9/02, 9/14 (Otkrytiya i Izobreteniya, **34**, No. 13: 11) (1991) (in Russian).
12. Yu. M. Koval' and V. V. Nemoshkalenko, *O Prirode Martensitnykh Prevrashcheniy* [On the Nature of Martensitic Transformations] (Kyiv: 1998) (Prepr./N.A.S. of Ukraine. Inst. for Metal Physics. No. 1, 1998) (in Russian).

Journal title abbreviations should conform to generally accepted styles:
https://www.cas.org/support/documentation/references/corejournals;
https://cdn.journals.aps.org/files/rmpguapb.pdf;
https://images.webofknowledge.com/WOK46P9/help/WOS/A_abrvjt.html;
https://mathscinet.ams.org/msnhtml/serials.pdf.

Equations and Formulae: Formulas in the text should be inserted by **MathType**, fully compatible with MS Office. Vectors should be typed in bold without arrows above. Note that complicated formulae, mathematical expressions or (de)notations are not recommended in the title, abstract, and keywords.

Tables: Number tables consecutively with Arabic numerals and give a clear descriptive caption at the top.

Figures: All figures should be numbered with consecutive Arabic numbers, have descriptive captions and be mentioned in the text. Keep figures separate at the end of the text and clearly label each figure with author's name and figure number. The labels at axis should contain the designation (or notation) of quantities and their units.

Preparation: Figures submitted must be of a high enough standard for reproduction with 300–600 dpi resolution (including half-tone illustrations). Redrawing or retouching of unusable figures will be charged to the authors.

Colour Plates: Whenever, the use of colour is an integral part of the research, or where the work is generated in colour, the Journal will publish (in paper version) the colour illustrations with charge to the author. Reprints in colour will carry a surcharge. Please write to the Publisher for details.

Submission of Electronic Text: Authors should submit the electronic version of their paper by e-mail to the Editorial Office. The text file should be saved in the native formats of the MS Word with a name consisting the name of the first author, for example, Hotovchenko.docx. The electronic form of figures (in TIF, EPS, JPG, PNG formats preferably and with name consisting the name of the first author also, for example, Hotovchenko_fig2a.jpg) should be planned so that they reduce to 12.7 cm column width (or less), and keep them separated from the text file. It is desirable to submit additionally all the **figures** within the format of the program, in which they were created.

Proofs: Contributors will receive page proofs for correction by e-mail as a PDF document. These must be returned to Kyiv office (mfint@imp.kiev.ua with subject beginning by word 'mfint') within 5 days of receipt.

Page Charges: There are no page charges to individuals or institutions.

Reprints: Authors can freely download a PDF version of their published article from journal website: https://mfint.imp.kiev.ua. The printed issues may be ordered by completing the appropriate form sent with proofs and prepaid by authors under the terms as for subscription.

Further Information: All questions arising during the **peer review** or after acceptance of manuscripts, especially those relating to reprints, should be directed to G. V. Kurdyumov Institute for Metal Physics, N.A.S. of Ukraine, Executive Managing Editor, Editorial Office, 36 Academician Vernadsky Blvd., UA-03142 Kyiv, Ukraine;
Fax: +380 44 4242561, e-mail: mfint@imp.kiev.ua (with subject beginning by word 'mfint').
We ask the authors to apply with their manuscript Copyright Transfer Agreement form.

Copyright Transfer Agreement

We, the undersigned authors of the manuscript '_____', transfer to the Founders, Publisher, and Editorial Board of the Journal 'Metallophysics and Advanced Technologies' (according to agreements between them) the right to publish this manuscript in original language or in translation to the other languages. We confirm that publication of this manuscript **will not** infringe a copyright of other persons or organizations and publication ethics.

Author(s):_____
(Last Name, First Name, Affiliation)

Correspondence Address:_____
Phone and e-mail: _____

_____ _____
(Signature) *(Date)*

ІНФОРМАЦІЯ (ПРАВИЛА) ДЛЯ АВТОРІВ

Науковий журнал «Металофізика та новітні технології» (МфНТ) щомісяця публікує статті, які раніше ще не публікувалися та не перебувають на розгляді для опублікування в інших виданнях. Статті мають містити результати експериментальних і теоретичних досліджень в області фізики та технологій металів, стопів і сполук з металічними властивостями; рецензії на монографії; інформацію про конференції, семінари; відомості з історії металофізики; рекламу нових технологій, матеріялів, приладів. Журнал дотримується загальноприйнятих принципів, зазначених на його сайті в документах з публікаційної етики та щодо неприйнятних практик.

Тематика журналу: *Електронні структура та властивості, Дефекти кристалічної ґратниці, Фазові перетворення, Фізика міцности та пластичности, Металічні поверхні та плівки, Будова та властивості наномасштабних і мезоскопічних матеріялів, Аморфний і рідкий стани, Взаємодії випромінення та частинок із конденсованою речовиною, Матеріяли в екстремальних умовах, Реакторне й авіакосмічне металознавство, Медичне металознавство, Нові металеві матеріяли та синтетичні метали, Металовмісні смарт-матеріяли, Фізико-технічні основи експерименту та діягностики, Дискусійні повідомлення.*

Статті публікуються однією з двох мов: англійською (віддається перевага) або українською.

Статті, в оформленні яких не дотримано наступних правил для опублікування в МфНТ, повертаються авторам без розгляду по суті. (Датою надходження вважається день повторного надання статті після дотримання зазначених нижче правил.)

1. Стаття має бути підписаною всіма авторами (із зазначенням їхніх адрес електронної пошти); слід вказати прізвище, ім'я та по батькові автора, з яким редакція буде вести листування, його поштову адресу, номери телефону та факсу й адресу електронної пошти.

2. Виклад матеріялу має бути чітким, **структурованим** (розділами, наприклад, «1. Вступ», «2. Експериментальна/Теоретична методика», «3. Результати та їх обговорення», «4. Висновки», «Цитована література»), стислим, без довгих преамбул, відхилень і повторів, а також без дублювання в тексті даних таблиць, рисунків і підписів до них. Анотація та розділ «Висновки» мають не дублювати один одного. Числові дані слід наводити в загальноприйнятих одиницях.

3. Об'єм оригінальної (неоглядової) статті має бути не більше 5000 слів (з урахуванням основного тексту, таблиць, підписів до рисунків, списку використаних джерел) і 10 рисунків. **Об'єм оглядової статті** — до 10000 слів та 30 рисунків.

4. За потреби до редакції може надаватися друкований (A4, подвійний інтервал) примірник рукопису з ілюстраціями.

5. До редакції обов'язково надається (по **e-mail**) файл статті, набраний у текстовому редакторі Microsoft Word, з назвою, що складається з прізвища першого автора (латиницею), наприклад, Hotovchenko.docx.

6. Електронна версія рукопису та його друкований варіянт (в разі його надання) мають бути ідентичними. Вони мають оформлюватися за шаблоном, який можна завантажити з сайту журналу, і містити 5–7 **індексів PACS** в редакції 'Physics and Astronomy Classification Scheme 2010'. Тексти статей мають також містити **назву статті**, **список авторів**, **повні назви** та **поштові адреси установ**, в яких вони працюють, **анотацію статті** (200–250 слів), **5–7 ключових слів** двома мовами **(англійською** та **українською)**, а заголовки таблиць і підписи до рисунків мають подаватися **як мовою рукопису, так і англійською мовою**; англомовна анотація може бути представленою в більш розгорнутому варіянті (до 500 слів). Назва статті, її анотація та ключові слова мають не містити складні формули, математичні вирази чи позначення.

7. Електронні версії рисунків мають бути представленими у вигляді окремих файлів (у форматах TIF, EPS, JPG, PNG з розріжненням у 300–600 dpi) з назвами, що складаються з прізвища першого автора (латиницею) та номера рисунка, наприклад, Hotovchenko_fig2a.jpg. Додатково рисунки надаються у форматі програми, в якій вони створювалися.

8. Написи на рисунках (особливо на півтонових) слід по можливості замінити літерними позначеннями (набраними на контрастному фоні), а криві позначити цифрами або різними типами ліній/маркерів, які мають бути роз'ясненими в підписах до рисунків або в тексті. На графіках усі лінії/маркери мають бути достатньої товщини/розміру для якісного відтворення їх у зменшеному в 2–3 рази вигляді (рекомендована початкова ширина рисунка — 12,7 см). Світлини мають бути чіткими та контрастними, а написи та позначення мають не закривати істотні деталі (для чого можна використовувати стрілки). Замість зазначення в підтекстовці збільшення під час зйомки бажано проставити масштаб (на контрастному фоні) на одній з ідентичних світлин. На графіках підписи до осей, **виконані мовою статті**, мають містити позначення (або найменування) величин, що відкладаються вздовж осей, і відділені комою їхні одиниці вимірювання.

9. Формули в текст треба вставляти за допомогою редактора формул **MathType**, сумісного з MS Office. **Вектори** слід набирати напівтовстим шрифтом без стрілок зверху.

10. Рисунки, таблиці, формули, а також підрядкові **примітки (виноски)** мають нумеруватися поспіль по всій статті.

11. Посилання на літературні джерела слід давати у вигляді порядкового номера, надрукованого в рядок у квадратних дужках. Список цитованої літератури складається почергово за першою згадкою джерела. Приклади оформлення посилань наведено нижче (просимо звернути увагу на порядок розташування ініціалів і прізвищ авторів, бібліографічних відомостей і на розділові знаки, а також на необхідність зазначення **всіх** співавторів цитованої роботи та її ідентифікатора **DOI**, якщо він є):

1. S. O. Firstov and T. G. Rogul, *Metallofiz. Noveishie Tekhnol.*, **44**, No. 1: 127 (2022) (in Ukrainian). https://doi.org/10.15407/mfint.44.01.0127
2. V. B. Tarelnyk, O. P. Gaponova, and Ye. V. Konoplianchenko, *Prog. Phys. Met.*, **23**, No. 1: 27 (2022). https://doi.org/10.15407/ufm.23.01.027
3. A. Meisel, G. Leonhardt, and R. Szargan, *Röntgenspektren und Chemische Bindung* [X-Ray Spectra and Chemical Bond] (Leipzig: Akademische Verlagsgesellschaft Geest & Portig K.-G.: 1977) (in German).
4. J. M. Ziman, *Printsipy Teorii Tverdogo Tela* [Principles of the Theory of Solids] (Moscow: Mir: 1974) (Russian translation).
5. M. A. Stucke, D. M. Dimiduk, and D. M. Hazzledine, *High Temperature Ordered Intermetallic Alloys. V* (Eds. I. Baker and R. Darolia) (Pittsburgh, PA, USA: MRS: 1993), p. 471.
6. *Handbook of Mathematical Functions with Formulas, Graphs and Mathematical Tables* (Eds. M. Abramowitz and I. A. Stegun), Nat'l Bureau of Standards. Appl. Math. Ser. Vol. **55** (Washington, D.C.: U.S. Govt. Printing Office: 1964).
7. B. B. Karpovych and O. B. Borovkoff, *Proc. of Symp. 'Micromaterials Engineering' (Dec. 25–31, 1999)* (Kyiv: RVV IMF: 2000), vol. **2**, p. 113 (in Russian).
8. A. Eh. Krug, *Abstr. Int. Conf. Phys. Phenomena (Dec. 25–31, 1991, Alushta)* (Kharkiv: 1991), p. 12.
9. T. M. Radchenko, *Vplyv Uporyadkuvannya Defektnoyi Struktury на Transportni Vlastyvosti Zmishanykh Krystaliv* [Influence of Ordering of the Defect Structure on Transport Properties of the Mixed Crystals] (Thesis of Disser. for the Degree of Dr. Phys.-Math. Sci.) (Kyiv: G. V. Kurdyumov Institute for Metal Physics, N.A.S.U.: 2015) (in Ukrainian). https://doi.org/10.13140/RG.2.2.35430.22089
10. E. M. Gololobov, V. B. Shipilo, N. I. Sedrenok, and A. I. Dudyak, *Sposob Polucheniya Karbonitridov Metallov* [Production Method of Metal Carbonitrides], Authors' Certificate 722341 SSSR (Publ. November 21, 1979) (in Russian).
11. V. G. Trubachev, K. V. Chuistov, V. N. Gorshkov, and A. E. Perekos, *Sposob Polucheniya Metallicheskikh Poroshkov* [The Technology of Metallic Powder Production]: Patent 1639892 SU. MKI, B22 F9/02, 9/14 (Otkrytiya i Izobreteniya, **34**, No. 13: 11) (1991) (in Russian).
12. Yu. M. Koval' and V. V. Nemoshkalenko, *O Prirode Martensitnykh Prevrashcheniy* [On the Nature of Martensitic Transformations] (Kyiv: 1998) (Prepr./N.A.S. of Ukraine. Inst. for Metal Physics. No. 1, 1998) (in Russian).

Слід використовувати загальноприйняті скорочення назв журналів:
https://www.cas.org/support/documentation/references/corejournals;
https://cdn.journals.aps.org/files/rmpguapb.pdf;
https://images.webofknowledge.com/WOK46P9/help/WOS/A_abrvjt.html;
https://mathscinet.ams.org/msnhtml/serials.pdf.

Необхідною вимогою є також надання авторами додаткового списку цитованої літератури (**References**) в **латинській транслітерації** (система **BGN/PCGN**; рекомендовані транслітератори: http://www.slovnyk.ua/services/translit.php; http://ru.translit.net/?account=bgn).

Після транслітерованих назв книг, дисертацій, патентів та ін. слід у квадратних дужках наводити їхній англомовний переклад (див. приклади вище). При транслітерації статей з МфНТ слід використовувати написання П.І.Б. авторів, наведені **лише** в англомовному змісті відповідного випуску, і **офіційну** транслітеровану назву журналу (див. також першу сторінку кожної статті та сайт).

12. Коректура авторам надсилається електронною поштою у вигляді pdf-файлу після завершення етапу **рецензування**. На перевірку коректури авторам відводяться 5 робочих днів. Після закінчення зазначеного терміну стаття автоматично направляється до друку. Виправлення слід відмітити та прокоментувати в самому pdf-файлі або оформити у вигляді переліку виправлень (підписаного уповноваженим представником колективу авторів) і переслати електронною поштою на адресу редакції.

Електронний варіянт статті надсилається на e-mail: mfint@imp.kiev.ua (з темою, що починається словом 'mfint'). Друкована версія рукопису (якщо у ній є потреба) надсилається за адресою: **Інститут металофізики ім. Г. В. Курдюмова НАН України, редакція МфНТ; бульвар Акад. Вернадського, 36; 03142 Київ, Україна** або відповідному регіональному редактору (див. сайт).

Автори можуть вільно завантажити pdf-файли опублікованих статей з сайту журналу (https://mfint.imp.kiev.ua), а також замовити друковані примірники випуску журналу зі своєю статтею, надіславши до редакції журналу **разом з коректурою відповідну заявку та квитанцію про оплату** друку необхідної кількості примірників випуску на умовах, аналогічних передплатним.

Відповідно до угод між редакцією МфНТ, засновниками та видавцем журналу, редакція вважає, що автори, надсилаючи їй рукопис статті, передають засновникам, видавцю та редколеґії право опублікувати цей рукопис мовою ориґіналу та в перекладі іншими мовами, і просить авторів відразу прикладати до рукопису «Угоду про передачу авторського права».

Угода про передачу авторського права

Ми, що нижче підписалися, автори рукопису «_____», передаємо засновникам, видавцю та редколеґії журналу «Металофізика та новітні технології» (згідно з угодами між ними) право опублікувати цей рукопис мовою ориґіналу та в перекладі іншими мовами. Ми підтверджуємо, що ця публікація **не** порушує авторського права інших осіб або організацій і принципів наукової етики. При цьому за авторами зберігаються всі інші права як власників цього рукопису.

Підписи авторів: _____ (П.І.Б., дата, адреса, тел., e-mail)

Metallophysics and Advanced Technologies
Металофіз. новітні технол.
Metallofiz. Noveishie Tekhnol.
2025, vol. 47, No. 6, pp. 567–573
https://doi.org/10.15407/mfint.47.06.0567
Reprints available directly from the publisher

PACS numbers: 61.46.Df, 61.80.Ed, 68.35.Ct, 68.37.Ps, 68.55.J-, 81.70.Pg

Morphological Properties of Manganese Ferrite Nanoparticles

A. F. Gochuyeva

Azerbaijan State Oil and Industry University,
20 Azadlig Ave.,
AZ-1010 Baku, Azerbaijan

The paper discusses the results for the sample with a high degree of purity (nanopowder with true density of 4.96 g/cm^3, particle size of 60 nm and purity of 98.5%; SkySpring Nanomaterials, USA) and, in comparison with it, prepared one in the form of a pill of size 4×15×5 mm for 1 hour; the surface morphology of the irradiated sample under the influence of γ-rays is studied. The AFM (atomic force microscopy) results show that the phases included in the composition of the ordinary $MnFe_2O_4$ nanoparticle are compactly assembled into different parts, and the presence of slight surface roughness is observed. In the irradiated sample, the phases are evenly distributed, and the surface roughness is clearly visible.

Key words: manganese ferrite, nanoparticles, γ-rays, surface morphology, AFM.

У статті обговорюються результати стосовно зразка високого ступеня чистоти (нанопорошок зі справжньою густиною у 4,96 г/см^3, розміром частинок у 60 нм і чистотою у 98,5%; SkySpring Nanomaterials, США) і, в порівнянні з ним, приготованого у формі пігулки розміром 4×15×5 мм упродовж 1 години; досліджено морфологію поверхні опроміненого зразка під впливом γ-променів. Результати АСМ (атомно-силової мікроскопії) показують, що фази, які входять до складу звичайної наночастинки $MnFe_2O_4$, компактно зібрані в різні частини; також спостерігається наявність невеликої шерсткости поверхні. В опроміненому зразку фази розподілені рів-

Corresponding author: Aynura F. Gochuyeva
E-mail: aynuragochuyeva@gmail.com

Citation: A. F. Gochuyeva, Morphological Properties of Manganese Ferrite Nanoparticles, *Metallofiz. Noveishie Tekhnol.*, **47**, No. 6: 567–573 (2025); DOI: 10.15407/mfint.47.06.0567

номірно, та чітко видно шерсткість поверхні.

Ключові слова: ферит Манґану, наночастинки, γ-промені, морфологія поверхні, АСМ.

(Received 13 August, 2024; in final version, 4 June, 2025)

1. INTRODUCTION

As we know, compared to large-scale materials and microparticles, nanoparticles exhibit more sophisticated and greater properties and enable their application in a large number of different fields. As a key member of the ferrite family, $MnFe_2O_4$ has been the subject of extensive research due to its special magnetic and electromagnetic properties. Understanding the magnetic properties of nanoparticles in magnetic materials is one of the important topics. The magnetic transitions present in nanostructured $MnFe_2O_4$ oxides with a spinel ferrite structure are widely used in industrial and medical biology. This nanoparticle is also a non-toxic compound and an environmentally friendly non-corrosive material, resistant to high temperature and impact. In $MnFe_2O_4$, about 80% of the Mn^{2+} ions are in the tetrahedral site and 20% in the octahedral site, so it is a partially inverted spinel. Spinel ferrites have the structure AB_2O_4, where A and B represent the tetrahedral and octahedral cation sites, respectively, and O represents the oxygen anion site. In the normal spinel structure, site A is occupied by Fe^{3+} ions, and in the reverse spinel structure, site A is occupied by Mn^{2+} ions. It is possible to control the shape and particle size of the $MnFe_2O_4$ compound, as well as adjust the catalytic, magnetic, dielectric, electronic, optical and electrical properties [1, 2]. By adding certain cations or anions to change the concentration of electrons and holes, the magnetic, optical and electrical properties of ferrites can be improved or adjusted. Spinel-containing ferrites have several advantages over inverse spinel ferrites, in part because they are cheaper, easier to manufacture, and have different magnetic properties. Furthermore, the radius, charge, lattice energy and crystal site stabilization energy of the solute ion added in sites A and B significantly affect the distribution of cations. Manganese ferrite ($MnFe_2O_4$) nanoparticles, which belong to spinel ferrites, are used in magnetic applications, such as recording media devices, drug delivery, ferrofluids, biosensors and contrast enhancement agents for MRI technology. There are many experimental synthesis methods to obtain $MnFe_2O_4$ ferrites. Among them, thermal decomposition, sol–gel, colloidal emulsion, solvo/hydrothermal and laser pyrolysis, *etc.* methods can be shown. Solvo/hydrothermal synthesis is an environmentally friendly approach to produce small and uniformly distributed nanostructures. It also makes

it easy to add particles to create composite materials [11]. The solvothermal synthesis method, usually obtained using a microwave oven, allows precise control of the parameters of compound properties, phase purity, high productivity, reproducibility, uniform particle morphology. Manganese ferrites at the nanoscale exhibit interesting morphological characteristics. Considering these and other characteristics, it can be assumed that manganese ferrite nanoparticles can be used in elements used in telecommunications by forming a composite with the polymer materials used in our previous work [3–10]. They have a wide range of applications ranging from fundamental research to industrial applications. In the present study, the surface morphology of ferrite nanoparticles was investigated.

2. EXPERIMENTAL DETAILS

Nanopowder sample with a true density of 4.96 g/cm^3, a particle size of 60 nm and a purity of 99.95% (SkySpring Nanomaterials, USA) was used during the studies. The $MnFe_2O_4$ nanoparticle has a spherical shape depending on the synthesis process. These particles in powder form are manufactured by pressing. Pressing process Model No. FTIR hydraulic press with ATHP-15 is made. The process was carried out under complete laboratory conditions. To do this, the nanoparticle in powder form is poured into a special mold of 4 mm wide, 15 mm long and 5 mm high and pressed at room temperature to form a pill. The pressure during pressing was 50 kg/cm^2. The samples obtained in the form of pills were irradiated with a gamma ray with a radiation power of $\dot{D} = 1.41$ gray/sec and a radiation dose of 50 gray. Nanoeducator, Scanning probe microscope (Northern Ireland), AFM (atomic force microscopy) also studied the surface morphology of the sample at the nanoscale.

3. RESULTS AND DISCUSSION

In our research, atomic force microscopy (AFM) of a nanoparticulate antiferromanganese-based sample was studied. Despite the wide application of AFM in materials science and its scientific and engineering impact, atomic force microscopy has been rarely used in magnetic nanoparticles. When doping is performed on various samples, TEM, SEM, *etc.* are used when studying their structure. It is very suitable to learn AFM analysis at the same time as analysis. In our work, the AFM images of the pure $MnFe_2O_4$ nanoparticle and pellet of size 4×15×5 mm prepared and irradiated under the influence of gamma rays for 1 hour were examined. The surface morphology, topology and coating thickness of the $MnFe_2O_4$ composite elements were determined using AFM

images. The AFM images were taken at 24°C, being stable and reproducible. Figure 1(*a*) shows a topographical image of a typical contact mode AFM top view of a $MnFe_2O_4$ nanoparticle. The nanoparticles with a spherical diameter of 60 nm are irregularly distributed in the thin layer. In Figure 1(*b*), a large number of bumps are observed on the surface of the joint, indicating that this feature belongs, for example, to $MnFe_2O_4$, a magnetic nanoparticle. In some areas, a compact agglomeration of magnetic particles caused by strong attraction between nanoparticles can be observed [12, 13].

Figure 1(*c*) shows the AFM image of the same point in front three-dimensional topographic format, *i.e.*, 3*D*. At 24°C, a few particles of a nanoparticle size mentioned above mixed with medium-size particles form a relatively irregular surface with a given and increasing roughness. Looking at a 3*D* topographic image, we see many protrusions that break up the flat surface, causing roughness. Moreover, as shown in the 2*D* and 3*D* topographic images of $MnFe_2O_4$, it is clear that the thickness increases due to the precipitation of Mn^+ ions in the ferrites, which increase the thickness with the increase of the coating layer. The morphological study shows that the thickness of the coating increases due to the accumulation of particles in the surface layers. Figure 1(*d*)

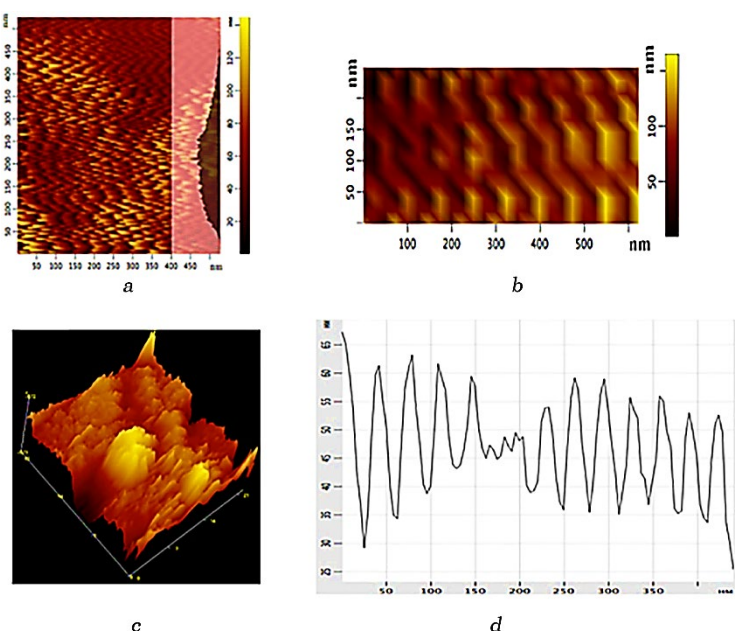

Fig. 1. *a*) typical topographic AFM image of a $MnFe_2O_4$ nanoparticle (in contact mode), *b*) 2*D* topographic image of a nanoparticle, *c*) 3*D* topographic image of a nanoparticle, *d*) height histogram of a nanoparticle obtained from data from a scanned surface 3×3 μm^2.

shows a histogram of the height size distribution of a $MnFe_2O_4$ nanoparticle obtained from data of a scanned area of 3×3 μm^2. This figure shows the elevation of the cross section produced by the irregular surface, which causes the roughness associated with the typical topographic image of a nanoparticle. From the data of the 3×3 μm^2 scanned area of the $MnFe_2O_4$ nanoparticle, it can be observed that the total surface roughness is approximately 67 nm [14, 15].

Figure 2(*a*) shows AFM images of a sample of $MnFe_2O_4$ nanoparticles prepared as 4×15×5 mm pellets and irradiated under the influence of γ-rays for 1 hour. Here, there is a topographic image of the AFM in contact mode. According to the topographic image, the crystal phases of the sample irradiated under the influence of γ-rays for 1 hour are distributed more evenly, and it is proven that the crystal phase is better. Spherical nanoparticles with a diameter of 60 nm are regularly distributed in the thin layer. Figure 2(*b*) shows that the phases are regularly distributed on the surface of the $MnFe_2O_4$ composite, unlike the 2*D* topographic image of the unirradiated sample. In the topographic image of the sample irradiated under the influence of γ-rays, the re-

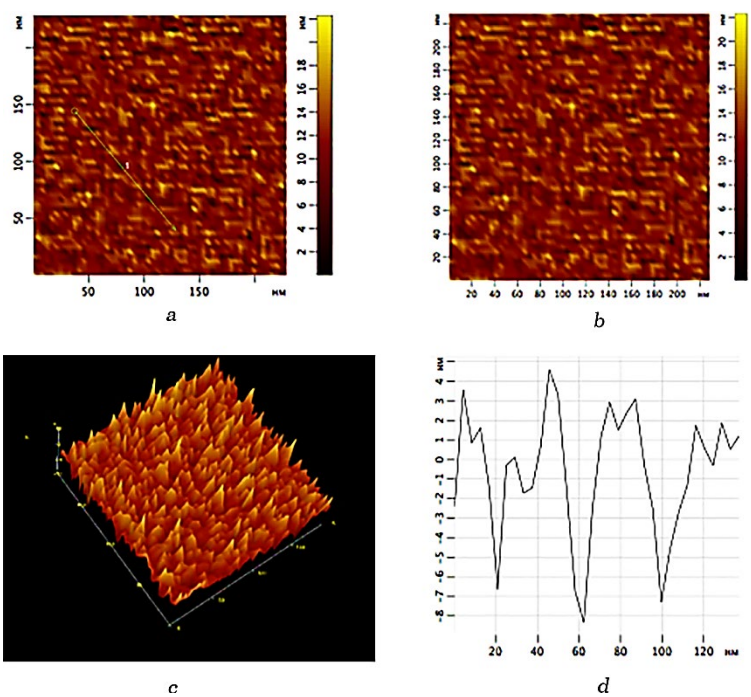

Fig. 2. *a*) typical AFM topographic image (in contact mode), *b*) 2*D* topographic image, *c*) 3*D* topographic image, *d*) height histogram obtained from data of a 3×3 μm^2 scanned area of a sample irradiated under the influence of γ-rays for 1 hour.

verse agglomeration process occurs in the entire area, *i.e.*, due to the lack of attraction between the nanoparticles, compact aggregation of the nanoparticles is not observed. The reason for this may be that the magnetic moment of the substance takes on an average value, depending on the valence of iron oxides (Fe^{2+} and Fe^{3+}) and also due to the effect of the given temperature during pressing.

Figure 2(*c*) shows the three-dimensional topographical image before AFM, *i.e.*, 3*D*, of the same point of the sample irradiated under the influence of γ-rays for 1 hour. Looking at the 3*D* topographic image, we see that the sample surface consists of roughness, which leads to an irregular layer. Even the roughness created along the surface appears in a regular form in terms of appearance. As shown in the two topographic images, the thickness also increased due to the precipitation of Mn^{+} ions in the ferrites, which increased the thickness with the increase of the coating layer. Figure 2(*d*) shows a histogram of the height size distribution obtained from data of a 3×3 μm^2 scanned area of a sample irradiated under the influence of γ-rays for 1 hour. This figure shows the elevation of the cross section produced by the irregular surface, which causes the roughness associated with the typical topographic image of a nanoparticle. From the data of the 3×3 μm^2 scanned area of the $MnFe_2O_4$ nanoparticle, it can be observed that the total surface roughness is approximately 4.7 nm.

4. CONCLUSIONS

In our research work, the necessary data for the important characteristics of the $MnFe_2O_4$ nanoparticle and the sample prepared in pill form of the above-mentioned size and subjected to the influence of gamma rays by AFM were presented. It was shown the similarities and differences observed in the polydispersity parameters obtained from the AFM data of the $MnFe_2O_4$ nanoparticle and the gamma-irradiated sample prepared as a pellet. As can be seen, the agglomeration process is clearly manifested on the surface of an ordinary nanoparticle. In the irradiated sample, no compact agglomeration is observed; on the contrary, the individual phases of the compound are arranged in an orderly manner. The reason for this regularity may be due to changes in valence of ferrite oxide.

REFERENCES

1. A. F. Gochuyeva, *J. Mod. Phys. B*, **36**, No. 2: 2150542 (2022).
2. A. F. Gochuyeva, *J. Mod. Phys. B*, **37**, No. 10: 350057 (2023).
3. M. A. Kurbanov, G. Z. Suleymanov, N. A. Safarov, A. F. Gochuyeva, I. N. Orujov, and Z. M. Mamedova, *Semicond.*, **45**: 503 (2011).
4. A. F. Gochuyeva, M. A. Kurbanov, B. H. Khudayarov, and A. M. Aliyeva, *Dig.*

J. Nanomater. Biostruct., **13**, No. 1: 185 (2018).
5. Z. M. Mammadova, M. A. Gurbanov, A. F. Gochuyeva, G. Z. Suleymanov, and D. B. Taghiyev, *EUFH*, No. 11, Section 13: 108 (2014).
6. A. F. Gochuyeva and Kh. Kh. Hashimov, *NMC&A*, **7**, No. 3: 194 (2023).
7. G. Z. Suleymanov, M. A. Gurbanov, A. Kh. Akbarov, Z. M. Mammadova, and A. F. Gochuyeva, *Azerbaijan Chem. J.*, No. 4: 50 (2017).
8. M. K. Kerimov, M. A. Kurbanov, A. A. Bayramov, N. A. Safarov, and A. F. Gochuyeva, *J. Scientific Israel – Technological Advantages*, **14**, No. 4: 9 (2012).
9. A. F. Gochuyeva, A. M. Mehdiyeva, and S. V. Bakhshaliyeva, *NMC&A*, **8**, No. 1: 87 (2024).
10. A. F. Gochuyeva, Kh. Kh. Hashimov, and I. Y. Bayramov, *Chalcogenide Lett.*, **20**, No. 4: 285 (2023).
11. A. F. Gochuyeva, *Semicond. Phys. Quantum Electron. Optoelectron.*, **27**, No. 3: 298 (2024).
12. S. H. Hosseini, R. Rahimi, and H. Kerdari, *Polym. J.*, **43**: 745 (2011).
13. L. P. Silva, Z. G. M. Lacava, N. Buske, P. C. Morais, and R. B. Azevedo, *J. Nanoparticle Res.*, **6**: 209 (2004).
14. Y. Yan, F. Shu, H. Chen, Zh. Dun, W. Lv, Zh. Zhang, W. Sun, and M. Liu, *Adv. Mater. Interfaces*, **10** (2023).
15. S.-K. Tong, P.-W. Chi, S.-H. Kung, and D.-H. Wei, *Sci. Rep.*, **8**: 1338 (2018).

Metallophysics and Advanced Technologies
Металофіз. новітні технол.
Metallofiz. Noveishie Tekhnol.
2025, vol. 47, No. 6, pp. 575–580
https://doi.org/10.15407/mfint.47.06.0575
Reprints available directly from the publisher

PACS numbers: 29.20.Ej, 29.25.Lg, 29.25.Ni, 29.27.Ac, 41.75.Ak, 41.75.Cn, 61.72.U-

Development of a Highly-Efficient Cold-Cathode Ion Source for Ion Implantation

O. V. Kosulya[*], B. M. Romaniuk[*], O. S. Oberemok[*], V. A. Baturin[*], O. Yu. Roenko[**], S. O. Yeryomin[**], P. O. Litvinov[**]

[*]*V. Ye. Lashkaryov Institute of Semiconductor Physics, N.A.S. of Ukraine, 41 Nauky Prosp., UA-03028 Kyiv, Ukraine*
[**]*Institute of Applied Physics, N.A.S. of Ukraine, 58 Petropavlivska Str., UA-40000 Sumy, Ukraine*

This article describes the design of a highly-efficient ion source with a Penning-system cold cathode for ion implantation. The ion source is intended for receiving large currents (> 10 μA) from solid materials whose boiling point is higher than the melting point. The ion source on the BALZERS MPB-202 ion implanter is also tested.

Key words: ion implantation, ion source, ion implanter, metal ions, semiconductor structures.

В даній статті описано конструкцію високоефективного джерела йонів із холодною катодою Пеннінґової системи для йонної імплантації. Джерело йонів призначене для одержання великих струмів (> 10 μA) з твердих матеріялів, температура кипіння яких вище за температуру топлення. Також проведено апробацію джерела йонів на йонному імплантері BALZERS MPB-202.

Ключові слова: йонна імплантація, джерело йонів, йонний імплантер, йони металів, напівпровідникові структури.

Corresponding author: Oleksandr Valeriyovych Kosulya
E-mail: alexandr250990@gmail.com

Citation: O. V. Kosulya, B. M. Romaniuk, O. S. Oberemok, V. A. Baturin, O. Yu. Roenko, S. O. Yeryomin, and P. O. Litvinov, Development of a Highly-Efficient Cold-Cathode Ion Source for Ion Implantation, *Metallofiz. Noveishie Tekhnol.*, **47**, No. 6: 575–580 (2026), DOI: 10.15407/mfint.47.06.0575

(Received 9 October, 2024; in final version, 4 June, 2025)

1. INTRODUCTION

One of the main methods of introducing impurities for the production of semiconductor devices is ion implantation using a gaseous or solid-state source of ions. Ion implantation systems use hot and cold cathode sources (Penning source). The hot cathode ion source allows implantation of ions from gases and solids. However, such a source cannot be used to implant elements with melting points lower than the boiling point. Such elements include Fe, Cu, Mo, Al, Ti, Be and others. In this regard, doping of the specified elements must be carried out using an ion source with a cold cathode [1–3].

The principle of operation of the source consists in atomization of a solid substance by plasma in a longitudinal magnetic field. However, such ion sources do not provide ion currents greater than 10 μA when spraying a solid-phase substance. That is why there was a need to develop an effective source of ions with a cold cathode of the Penning system, which would provide significantly larger ion currents [4].

2. CONSTRUCTION OF THE ION SOURCE

The design of the ion source was carried out using mathematical modelling of individual elements of the source, in particular the configuration of the magnetic field. An available type of magnet was selected, the dimensions of the source and its power supply system were calculated for further integration into the MVR-202 ion implanter of the 'BALZERS' company of the V. Lashkaryov Institute of Semiconductor Physics of the National Academy of Sciences of Ukraine. The implanter is used to work out the operating modes of the source during the generation of beryllium ions and demonstration implantation of beryllium ions into a plate made of indium antimonide [5, 6].

The physical and technical features of the development of plasma ion sources are fundamentally similar. However, the development requirements in the case of beryllium ion generation are specific and are regulated by the 'Sanitary rules for working with beryllium and its compounds' [7]. The latter requires specially equipped premises and imposes some restrictions on the use of standard methods of organizing work with ion sources. It is known that beryllium is similar to aluminium in many ways (diagonal similarity in Mendeleev's periodic system of elements). Therefore, at the development stage, the ion source was tested in the aluminium ion generation mode.

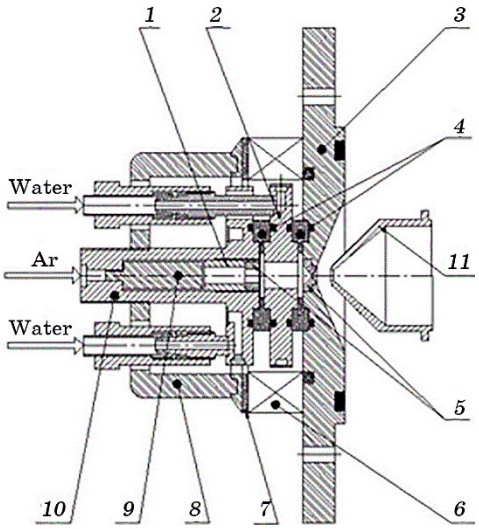

Fig. 1. Construction of the source of metal ions: *1*—hollow cathode; *2*—anode; *3*—anticathode; *4*, *7*—insulators; *5*—sputter inserts; *6*—NdFeB magnet; *8*—ion source case; *9*—ferromagnetic insert; *10*—cathode unit; *11*—extracting electrode.

Modern sources of metal ions require a stable plasma discharge of the working gas, effective atomization and ionization of the atoms of the implanted substance, acceleration of the formed ions and formation of an ion beam [8]. The design of such a source is schematically shown in Fig. 1.

The gas discharge chamber of the source consists of a hollow cathode (*1*), anode (*2*), anticathode (*3*) and body (*8*), which form the Penning discharge geometry. A uniform magnetic field in the gas discharge chamber is created by an NdFeB magnet (*6*) and magnetic conductors (*3*), (*8*), (*9*). The magnetic wire is highlighted in the figure with dashed lines.

The construction of the source is based on the formation of a plasma ion emitter using a Penning glow discharge. Ionization of sputtered atoms is ensured by the oscillation of electrons in the discharge chamber at low pressure. Modelling of the magnetic field of the ion source was carried out using the TRUCK program [9, 10]. The magnetic field in the cathode–anticathode gap was set in the range of 0.1–0.2 T. The simulation showed that when using a permanent NdFeB magnet (ring size 100×70×20 mm), the magnetic field strength (B) in the middle of the hollow cathode (*1*), anode (*2*) and the anticathode (*3*) reaches values of 0.16–0.2 T. These are acceptable values for the created ion source.

The supply of gas (Ar) for the formation of stable gas-discharge plasma is carried out through a hole in the back of the cathode (*1*). To avoid discharge burning near the cathode hole in the source, a gas

distribution cavity is provided. Gas supply to the discharge chamber is carried out through a narrow gap with a diameter of 0.5 mm in the peripheral area of the cathode assembly (*10*). Overheating of the electrodes in contact with the discharge can lead to a change in the burning mode of the discharge. To exclude this phenomenon, the cathode assembly (*10*) and the anode (*2*) of the ion source are cooled with water. For effective ionization of atoms in the gas discharge chamber, the atomized solid substance in the form of inserts (*5*) is pressed into the middle of the hollow cathode and anticathode. Spray inserts are made from the material whose ions need to be obtained. At the stage of working out the design of the source and its modes of operation, the insert was made of aluminium. The cathode (*1*) is made of molybdenum.

When voltage is applied to the electrodes of the source between the cathode (*1*), anode (*2*) and anticathode (*3*), a glow discharge with a voltage of $\cong 400$ V and a current in the range of 100–400 mA (Ir) ignites. Accelerated ions of the working gas (Ar) spray the aluminium inserts, creating an environment of Al atoms in the emission region of the gas discharge chamber. Fast oscillating electrons concentrated along the discharge axis provide ionization of aluminium atoms. Under the action of an external electric field, aluminium ions are extracted into the region of the ion–optical path of the source and form an ion beam. An external electric field is formed in the middle of the emission hole with a diameter of 1.5 mm, when a voltage of 30 kV is applied between the anticathode (*3*) and the extracting electrode (*11*).

After testing the work of the source with aluminium ions and ensuring sanitary and technical conditions for work with beryllium, the ion source was used to obtain Be ions. For this, sprayed inserts made of beryllium and aluminium alloys with a beryllium content of 20% and more were used.

3. APPROBATION OF THE ION SOURCE

The ion source was tested on the BALZERS MPB-202 ion implanter. The beryllium (Be) used to form the inserts in the cathode and anticathode has a high ionization energy of 9.32 eV. This energy is greater than that of Fe (7.89 eV), Cu (7.72 eV), Mo (7.1 eV), Al (5.98 eV), Ti (6.8 eV). In addition, Be has two electrons in the outer orbital, which complicates the ionization process. Accordingly, most ion sources with a cold cathode are not capable of providing an ion beam current of more than 0.07 μA. In our case, providing large ionic currents of beryllium ions will allow a priori to obtain large ionic currents for elements with lower ionization energy of atoms. The dependence of the Be^+ current on the discharge current is shown in Table 1. It can be seen that, with a discharge current of 400 milliamps,

the implanter is able to provide a beryllium ion current at the level of 0.35 μA. The resulting beryllium ion current was used to implant beryllium ions into the InSb matrix for 1 hour. The ion implantation energy was 20 KeV.

Using the Atomika 4000 instrument, secondary ion mass spectrometry (VIMS) profiles of the Be^+ impurity distribution along the depth were measured. The measurements were carried out using a beam of primary O^{2+} ions with energy of 7 keV. The depth of the crater formed during sputtering was measured using a DEKTAK 3030 contact profilometer. Along with this, a simulation of the implanted beryllium profile in the InSb matrix with energy of 20 keV was carried out using the SRIM (The Stopping and Range of Ions in Matter) program. Since the used program quite accurately predicts the distribution profiles of implanted ions in a solid body, the comparison of the measured beryllium profile and the simulated one will allow assessing qualitatively the effectiveness of the coordinated work of the created source and the BALZERS MPB-202 ion implanter.

Figure 2 shows the measured and modelled profiles of the beryllium impurity distribution along the depth. It can be seen that, within 1 hour, the beryllium source in the BALZERS MPB-202 implanter is able to provide a concentration of beryllium in the distribution maximum at the level of 10^{19} atoms/cm^3. The shapes of the measured and calculated distribution profiles are similar, which confirms the formation of a hidden layer for the used materials.

In this way, we can talk about the successful design of the developed source for this type of implanters. In addition, a 'lifetime' study of a beryllium-cathode ion source was conducted. The obtained 'lifetime' of

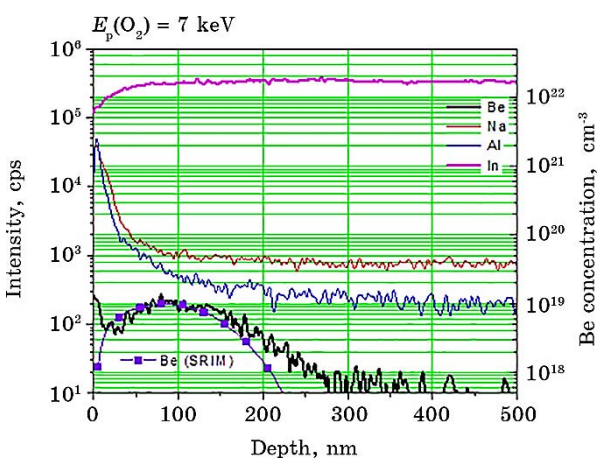

Fig. 2. Profile of the distribution of Be^+ implanted with E = 20 keV along the depth in the InSb matrix.

TABLE 1. Dependence of the beryllium beam current on the discharge current.

I_p, μA	100	150	200	250	300	350	400
I_{Be^+}, μA	0.07	0.08	0.1	0.13	0.16	0.2	0.35

the ion source was of 16 hours at a discharge current of 400 mA. The measured profile of impurity distribution in depth and simulated using the SRIM 2018 program are presented in Fig. 1.

As shown in Fig. 1, the real profile of the implanted impurity coincides with the theoretically calculated one.

4. CONCLUSION

A study of the 'lifetime' of an ion source with a beryllium cathode was carried out. The 'lifetime' of the ion source was of 16 hours at a discharge current of 400 mA.

The developed highly-efficient source with a cold cathode of the Penning system is capable of providing high currents of the ion beam from the following materials: Fe (9.6 μA), Cu (11 μA), Mo (9.7 μA), Al (23 μA), Ti (12 μA), Be (0.3 μA). No source with a cold cathode can provide the currents for the above-mentioned elements.

REFERENCES

1. E. Rimini, *Ion Implantation: Basics to Device Fabrication* (New York: Springer: 2013).
2. S. Sakai, N. Hamamoto, Y. Inouchi, S. Umisedo, and N. Miyamoto, *Rev. Sci. Instrum.*, **85**: 02C313 (2014).
3. S.R. Walther, B.O. Pedersen,and C.M. McKenna, *Proc. of Conference Record of the 1991 IEEE Particle Accelerator Conference* (1991).
4. V. A. Baturin, P. A. Litvinov, S. A. Pustovoitov, and O. Yu. Roenko, *Problems of Atomic Science and Technology*, **6**: 99 (2021).
5. V. A. Baturin, S. A. Yeryomin, S. A. Pustovoytov, P. A. Litvinov, A. Y. Karpenko, and V. I. Miroshnichenko, *Problems of Atomic Science and Technology*, **96**, Iss. 2: 204 (2015).
6. P. A. Litvinov, V. A. Baturin, and S. A. Pustovoytov, *Journal of Technical Physics*, **84**, Iss. 4: (2014).
7. https://www.atsdr.cdc.gov/csem/beryllium/docs/beryllium.pdf
8. P. A. Litvinov and V. A. Baturin, *Dzherelo Ioniv H^-* [H^- Ion Source]: Patent No. UA 71164 A, 20031110165 (2004) (in Ukrainian).
9. S. A. Pustovoytov, V. A. Baturin, S. A. Yeryomin, and A. J. Karpenko, *Problems of Atomic Science and Technology*, Iss. 4: 280 (2008).
10. V. A. Baturin and S. A. Yeryomin, *Journal of Nano- and Electronic Physics*, **10**, No. 4: 04021 (2018).

Metallophysics and Advanced Technologies
Металофіз. новітні технол.
Metallofiz. Noveishie Tekhnol.
2025, vol. 47, No. 6, pp. 581–594
https://doi.org/10.15407/mfint.47.06.0581
Reprints available directly from the publisher

PACS numbers: 71.70.Ej, 75.30.Ds, 75.30.Et, 75.50.Ee, 75.70.Tj, 75.85.+t, 85.70.Ay

Electric-Field Control of the Temporal Attenuation of Right-Handed and Left-Handed Magnons in Antiferromagnets

O. O. Boliasova[*,**] and V. M. Krivoruchko[***]

[*]*G. V. Kurdyumov Institute for Metal Physics, N.A.S. of Ukraine,*
36 Academician Vernadsky Blvd.,
UA-03142 Kyiv, Ukraine
[**]*Kyiv Academic University, N.A.S. and M.E.S. of Ukraine,*
36 Academician Vernadsky Blvd.,
UA-03142 Kyiv, Ukraine
[***]*Donetsk Institute for Physics and Engineering Named after O. O. Galkin,*
N.A.S. of Ukraine,
46 Nauky Ave.,
03028 Kyiv, Ukraine

Spin waves in antiferromagnets are promising alternative for replacing semiconductor technologies in future computational devices. One of the unique features of antiferromagnets is the availability of two spin waves with different chiralities—right-handed and left-handed ones. This degree of freedom, in addition to their phase and amplitude, can be used to create modern computational devices. The search for an effective method to separate and control the two modes in antiferromagnets is now attracting the increasing attention. Previous studies have demonstrated that an electric field can manipulate antiferromagnetic magnons of different chiralities. However, the influence of the Aharonov–Casher effect on the damping right-handed and left-handed spin waves has not been fully investigated. In this work, based on Landau–Lifshitz–Gilbert equations with Rayleigh-dissipation functional, we show that the applied electric field could effectively control the damping of the spin waves with different chiralities. Temporal attenuation of the right-

Corresponding author: Ol'ha Oleksandrivna Boliasova
E-mail: ol.boliasova@gmail.com

Citation: O. O. Boliasova and V. M. Krivoruchko, Electric-Field Control of the Temporal Attenuation of Right-Handed and Left-Handed Magnons in Antiferromagnets, *Metallofiz. Noveishie Tekhnol.*, **47**, No. 6: 581–594 (2025). DOI: 10.15407/mfint.47.06.0581

handed and left-handed modes has a shift along the wave-vector axis, which is directly proportional to the magnitude of the electric field. The relation between the damping parameters in the Rayleigh-dissipation functional plays an important role in dissipation behaviour. Our results show that the magnon lifetime depends on the electric field and dissipation parameters and is different for distinct chiralities. We believe our findings will encourage further investigation into dissipation processes in antiferromagnets and their impact on magnonic devices.

Key words: spin-wave dynamics, antiferromagnets, Aharonov–Casher effect, damping, Gilbert damping, right-handed and left-handed polarizations, Landau–Lifshitz–Gilbert equation.

Спінові хвилі в антиферомагнетиках розглядаються як перспективна альтернатива напівпровідниковим технологіям в майбутніх обчислювальних пристроях. Однією з ключових особливостей антиферомагнетиків є наявність двох спінових мод з різними хіральностями — правосторонньою та лівосторонньою. Цей додатковий ступінь свободи, разом із фазою й амплітудою, може бути використаний для створення новітніх магнонних обчислювальних систем. Пошук ефективних методів розщеплення та керування зазначеними модами в антиферомагнетиках наразі є предметом активних досліджень. Дослідження показують, що за допомогою електричного поля можна керувати антиферомагнетними магнонами з різною хіральністю. Водночас вплив ефекту Ааронова–Кашера на згасання спінових хвиль з правою та лівою поляризаціями залишається недостатньо вивченим. У даній роботі на основі рівнянь Ландау–Ліфшиця–Гілберта з урахуванням функціоналу Релейової дисипації продемонстровано, що прикладене електричне поле здатне ефективно контролювати згасання спінових хвиль з різною хіральністю. Показано, що часове згасання правосторонніх і лівосторонніх мод супроводжується зсувом уздовж осі хвильового вектора, який є прямо пропорційним до величини електричного поля. Встановлено, що співвідношення між параметрами функціоналу Релейової дисипації відіграє визначальну роль у дисипації. Результати роботи свідчать, що час життя магнонів залежить від електричного поля, параметрів дисипації та відрізняється для різних хіральностей. Одержані висновки відкривають перспективи для подальшого вивчення механізмів дисипації в антиферомагнетиках і їхнього впливу на магноніку.

Ключові слова: динаміка спінових хвиль, антиферомагнетики, ефект Ааронова–Кашера, дисипація, Гілбертова дисипативна константа, правостороння та лівостороння поляризації, рівняння Ландау–Ліфшиця–Гілберта.

(Received 2 June, 2025; in final version, 16 June, 2025)

1. INTRODUCTION

Magnonics [1], a recent branch of condensed matter physics, has

gained significant interest due to its potential to use spin waves (SWs) as carriers of information in electronic devices [2]. Spin waves can propagate without Joule heating and allow high operational speeds. Antiferromagnets (AFMs), due to the antiparallel arrangement of the two magnetic sublattices, can simultaneously support left-handed and right-handed polarized spin waves (SWs), providing an extra degree of freedom—chirality. Due to their stability to small field perturbations and absence of the stray field, AFMs are promising candidates for developing devices that incorporate spin waves.

Currently, there are several methods for manipulating SWs, for example, magnetic field, a Dzyaloshinskii–Moriya interaction in curvilinear magnets, spin-transfer torque, spin–orbit torque, spin Seebeck effect, voltage-controlled magnetic anisotropy, optical methods, and electric field. We will focus on the electric (**E**) field effect based on the so-called Aharonov–Casher (AC) effect [3, 4]. The AC effect, a quantum mechanical phenomenon like the Aharonov–Bohm effect, appears when a neutral particle with a magnetic moment moves under the effect of an **E** field and acquires a phase shift in the particle's wave function. In work [5], Cao and co-authors have demonstrated that the AC effect influences SWs propagating in a ferromagnetic ring when an **E** field is applied. Recent theoretical [6, 7] and experimental [8, 9] studies have demonstrated that the AC effect could impact SW propagation by using a static electric field in various magnetic systems, including AFMs, providing a mechanism for electric-field-based control of magnon dynamics.

It has been shown that in the first approximation, the influence of the AC effect on SWs can be mathematically represented as a Dzyaloshinskii–Moriya (DM)-like interaction [10, 11]. DM interaction, a form of antisymmetric exchange coupling, plays a crucial role in chiral magnetic systems with breaking inversional symmetry, resulting in SW nonreciprocity. In this context, the AC effect could effectively modify the spin-waves' dispersion relation in a symmetric crystal, lifting the energy degeneracy of two magnon modes by the applied electric field. As a result, SWs in antiferromagnetic materials can be distinctly separated into right-handed and left-handed modes [7].

One of the methods to split SWs in an AFM with different chirality is to induce the DM interaction, for example, by bending a material and breaking its symmetry. One of the disadvantages of this method is that one should bend it again to change the spin wave spectrum. At the same time, using the AC effect allows one to change the spin-waves' spectrum by applying an electric field, which is easier to incorporate in real devices. The unique advantages of this method include the strength and sign of the **E** field, which can be controlled, and the switchable nonreciprocity, which provides a potential platform for the design of magnonic devices.

Despite all advances in magnonic research, one critical aspect of SW dynamics remains unexplored. It is the influence of the AC effect on SWs energy dissipation. This article is dedicated to this question. Understanding how damping is affected by the topological AC effect is essential for a comprehensive description of magnons' dynamics and practical applications in antiferromagnetic-based magnonic devices [1, 12].

The dynamic characteristics of a dissipative (or absorbing) medium with finite damping include both real and imaginary components and are thus complex. There are two possible representations of the frequency and wave vector to describe the complex dispersion relation. One is the real frequency ω and the complex wave vector $\mathbf{k} = \mathrm{Re}\mathbf{k} + i\mathrm{Im}\mathbf{k}$; the other is the complex frequency $\omega = \mathrm{Re}\omega + i\mathrm{Im}\omega$ and the real wave vector $\mathbf{k}$, which is used widely in magnetism and spintronics communities. One can choose one of the two representations depending on the problem under investigation. The real ω and complex $\mathbf{k}$ focus on how the wave vector is affected by damping, and it is adequate to investigate the damping effect on propagating waves (see, for example, [13]). The complex ω and real $\mathbf{k}$ focus on how the frequency is affected by damping and describe the damping effect on the resonance, including the uniform magnetization dynamics. In this report, we use the last combination to demonstrate how the applied electric field modifies the SWs energy and damping in the two-sublattice AFM insulator. To derive analytical solutions, we used the set of the Landau–Lifshitz–Gilbert equations. There are two common options for how to adjust for damping: (i) including only the intrasublattice component [14], or (ii) a combination of intrasublattice and intersublattice components [15–17]. We will show how each of these options could modify the temporal damping, a so-called SW-regime [18], *i.e.*, spectrum width.

The paper is structured as follows: in the next Section, we will provide a brief explanation of the model used. In Section 3, our main results are presented. Section 4 is dedicated to discussing the results and presenting the conclusions derived from the study. Finally, we express our gratitude in acknowledgments.

2. THEORETICAL DETAILS

We consider the easy axis AFM consisting of two equivalent sublattices with magnetization $\mathbf{M}_1$ and $\mathbf{M}_2$. Further, for convenience, we will use unit vectors $\mathbf{m}_i = \mathbf{M}_i/M_\mathrm{s}$, where i is the sublattice number ($i = 1, 2$), $\mathbf{M}_\mathrm{S} \parallel Oz$ is sublattice saturation magnetization. Figure 1 shows the system view, where the electric field $\mathbf{E}$ is applied along the y-axis and magnons propagate along the x-axis.

Assuming the sublattices are equal and an AFM is symmetric under sublattice permutations, the free energy $F(\mathbf{m})$ of the system under con-

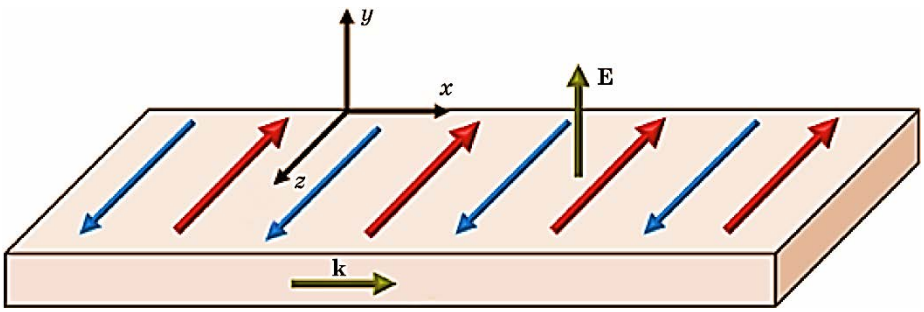

Fig. 1. Schematic representation of the antiferromagnet under electric field effect. Thin blue arrows along z direction and thick red arrows along $-z$ direction indicate the magnetization of the first and second sublattices accordingly. Electric field $\mathbf{E} \parallel Oy$, wave vector $\mathbf{k} \parallel Ox$.

sideration is:

$$F(\mathbf{m}) = \frac{A}{2}\int_V \left(\left(\frac{\partial \mathbf{m}_1}{\partial x}\right)^2 + \left(\frac{\partial \mathbf{m}_2}{\partial x}\right)^2 \right) dx + J\int_V (\mathbf{m}_1\mathbf{m}_2)dx - \\ - \frac{K}{2}\int_V \left(\mathbf{m}_1^2 + \mathbf{m}_2^2\right)dx + \frac{\mathbf{D}}{2}\int_V \left(\mathbf{m}_1 \times \frac{\partial \mathbf{m}_2}{\partial x} + \mathbf{m}_2 \times \frac{\partial \mathbf{m}_1}{\partial x} \right) dx. \quad (1)$$

The first two terms describe nonhomogeneous intrasublattices exchange coupling with a constant A, and homogeneous intersublattices' exchange coupling with a constant J. The next term corresponds to magnetocrystalline anisotropy with the anisotropy constant K. Here, the anisotropy along the z-axis is considered. The last term describes the effect of the electric field. In the first approximation, the AC effect mathematically could be incorporated in the form of the DM-like interaction $\mathbf{D}(\mathbf{m}_1 \times \mathbf{m}_2)$ [10, 11], where $\mathbf{D}$ is the vector depending on the applied electric field [6]:

$$\mathbf{D} = J\frac{ea}{E_{SO}}\mathbf{E} \times \mathbf{e}_{12} \equiv d\mathbf{E} \times \mathbf{e}_{12}. \quad (2)$$

Here, a is the distance between magnetic ions, e is the charge of the electron, $\mathbf{e}_{12}$ is unit vector in the direction connecting the ions from different sublattices, E_{SO} is energy of the spin–orbit interaction that inversely depends on the strength of the spin–orbit coupling. Recent studies [6] have shown that in some materials, E_{SO} could be around 1–3 eV, which makes this interaction valuable. As follows from Eq. (2), to achieve the maximum contribution from this interaction, the wave vector $\mathbf{k}$, the magnetization $\mathbf{m}_i$, and the electric field $\mathbf{E}$ should be orthogonal as in Fig. 1.

A phenomenological approach utilizes the Landau–Lifshitz–Gilbert

equation to describe the dynamics of magnetic materials. The equation with the dissipation term **R** is given by:

$$\frac{\partial \mathbf{m}}{\partial t} = -\gamma \mathbf{m} \times \mathbf{H}^{\text{eff}} + \mathbf{R},$$

where $\mathbf{H}^{\text{eff}} = -dF/d\mathbf{m}_i$ is the effective field, $\gamma = g\mu_0\mu_B / \hbar$ is the gyromagnetic ratio (here, g is the g factor, μ_0 is the magnetic permeability of the vacuum, μ_B is the Bohr magneton, $\hbar$ is the reduced Planck constant). In ferromagnets, the Gilbert dissipation term looks like $\mathbf{R} = \alpha_G \mathbf{m} \times \partial \mathbf{m} / \partial t$. When considering two-sublattice magnets, a question arises about how to account for the dissipation term. Some recent works [15, 16] argue for using the Rayleigh-dissipation functional as a matrix 2×2 with different damping coefficients. Thus, the two-sublattice magnet is described by the system of two torque equations with intrasublattice (α_{11}, α_{22}) and intersublattice (α_{12}, α_{21}) damping coefficients, which looks like:

$$\begin{aligned}
\frac{\partial \mathbf{m}_1}{\partial t} &= -\gamma \mathbf{m}_1 \times \mathbf{H}_1^{\text{eff}} + \alpha_{11} \mathbf{m}_1 \times \frac{\partial \mathbf{m}_1}{\partial t} + \alpha_{12} \mathbf{m}_1 \times \frac{\partial \mathbf{m}_2}{\partial t}, \\
\frac{\partial \mathbf{m}_2}{\partial t} &= -\gamma \mathbf{m}_2 \times \mathbf{H}_2^{\text{eff}} + \alpha_{21} \mathbf{m}_2 \times \frac{\partial \mathbf{m}_1}{\partial t} + \alpha_{22} \mathbf{m}_2 \times \frac{\partial \mathbf{m}_2}{\partial t}.
\end{aligned} \tag{3}$$

In AFM with equivalent sublattices, the number of damping parameters reduces to intrasublattice ($\alpha = \alpha_{11} = \alpha_{22}$) and intersublattice ($\alpha_c = \alpha_{12} = \alpha_{21}$) ones. It should be noted here that the damping within a sublattice should be greater than the damping between sublattices. In AFM, researchers commonly use one damping inside each sublattice α [14, 19]. Neglecting α_c implies that variables $\mathbf{m}_1$ and $\mathbf{m}_2$ are not directly connected in the damping processes. However, the magnetization of the two sublattices is coupled and cannot be missed during the discovery of the magnetization dynamics [17]. As is shown in the next Section, the **E** field also affects SWs' intersublattice attenuation.

3. AHARONOV–CASHER EFFECT ON TEMPORAL ATTENUATION OF SPIN WAVES

We assume that the AFM is in the collinear state and consider SWs with the frequency ω and wave **k** propagating along the x-axis, $\mathbf{k} \parallel Ox$, such that

$$\begin{aligned}
\mathbf{m}_1 &= \mathbf{x} m_{1x} \exp(i(\omega t - kx)) + \mathbf{y} m_{1y} \exp(i(\omega t - kx)) + \mathbf{z} m_{1z}, \\
\mathbf{m}_2 &= \mathbf{x} m_{2x} \exp(i(\omega t - kx)) + \mathbf{y} m_{2y} \exp(i(\omega t - kx)) + \mathbf{z} m_{2z},
\end{aligned}$$

with a small deviation of the magnetization of the first and second sub-

lattices along the z-axis $|m_{1z}| = |m_{2z}| \approx 1$. After obtaining the effective field from expression (1) and substituting it into the system of equations (3), we switch to circular variables defined as $m_{i+} = m_{ix} + im_{iy}$, $m_{i-} = m_{ix} - im_{iy}$. This allows us to derive a matrix consisting of two equations:

$$\begin{pmatrix} \pm\frac{M_S}{\gamma}\omega - P - i\alpha\omega & -W_{\pm} - i\alpha_c\frac{M_S}{\gamma}\omega \\ W_{\pm} + i\alpha_c\frac{M_S}{\gamma}\omega & \pm\frac{M_S}{\gamma}\omega + P + i\alpha\frac{M_S}{\gamma}\omega \end{pmatrix} \begin{pmatrix} m_{1\pm} \\ m_{2\pm} \end{pmatrix} = 0 . \tag{4}$$

Here, we introduce the next notation $P = J + K + Ak^2$, $W_+ = J \pm kdE$. The determinant of this matrix describes the SW dynamics of the AFM. By setting the real and imaginary parts to zero, we can find the spin waves' energy $\omega_i(k)$ and damping $\Gamma_i(k)$, using the substitution $\omega = \omega(k) + i\Gamma(k)$. We will provide the analytical expressions for these values below.

3.1. Spin-Wave Spectrum

It was shown earlier [7, 13] that the applied electric field splits the SWs spectrum into right-handed and left-handed magnons. Here, we demonstrate the AC effect on the SW dynamics in our system. We start by setting to zero the real part of the determinant of matrix (4), which gives us the next expression:

$$\omega_{\pm}(k) = \frac{\gamma}{M_S}\sqrt{(Ak^2 \pm kdE + 2J + K)(Ak^2 \mp kdE + K)} . \tag{5}$$

The difference between the magnon frequency with right-handed polarization, ω_+, and left-handed polarization, ω_-, is in the sign of the electric field term: kdE. The SW spectrum in the absence and the presence of an applied electric field is depicted in Fig. 2. The shift along the wave vector axis is directly proportional to the magnitude of the applied electric field. The greater the applied **E** field, the larger the splitting between right- and left-handed polarization magnons' energy. For visualization, here and below, the following quantities were used $M_S = 3.5 \cdot 10^5$ A/m, $A = 2 \cdot 10^{-12}$ J/m, $J = 5 \cdot 10^6$ J/m^3, $K = 10^5$ J/m^3, lattice constant $a = 0.5$ nm, and parameter of our system $d = 4.4 \cdot 10^{-12}$ C/m. We should point out that reversing the direction of the applied electric field results in a swap between left- and right-handed SWs shift along the wave vector **k**.

3.2. Spin-Wave Damping

The interplay between magnons' spin polarization and magnetic damp-

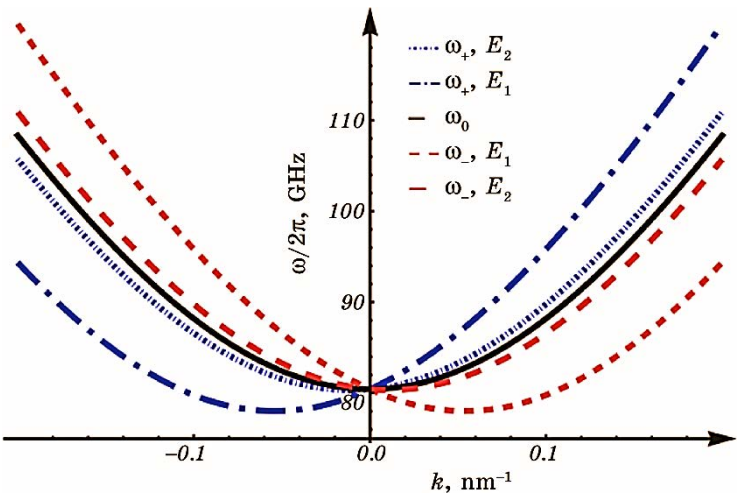

Fig. 2. Splitting of the spin wave spectrum under the **E** field effect, Eq. (5): $E_1 = 50$ V/μm, $E_2 = 10$ V/μm. The black line corresponds to $\mathbf{E} = \mathbf{0}$.

ing plays a crucial role in magnonics. We consider temporal decay, which could be found in resonance experiments as the width of the resonance peak [20]. This effect of AC has not been considered earlier.

Substituting $\omega = \omega(k) + i\Gamma(k)$ into matrix (4), we can get from the imaginary part of the determinant the following expression for temporal damping:

$$\Gamma_{\pm}(k) = \gamma \frac{\alpha(J + K + Ak^2) - \alpha_c(J \pm kdE)}{M_S(1 + \alpha^2 - \alpha_c^2)}. \tag{6}$$

As we see in Eq. (6), the external electric field affects SWs' damping through intersublattice damping coupling. The **E**-field application leads to the appearance of two attenuation functions $\Gamma_+(k)$ and $\Gamma_-(k)$. Like the frequency characteristics, the shift of the two attenuation curves depends on the value of the electric field (Fig. 3). Figure 4 shows temporal attenuation $\Gamma_{\pm}(k)$ at different values of the corresponding frequency $\omega_{\pm}(k)$.

We also found the ratio between the width of the resonance and its frequency $\Gamma_{\pm}(k)/\omega_{\pm}(k)$:

$$\frac{\Gamma_{\pm}(k)}{\omega_{\pm}(k)} = \frac{\alpha(J + K + Ak^2) - \alpha_c(J \pm kdE)}{(1 + \alpha^2 - \alpha_c^2)\sqrt{(J + K + Ak^2)^2 - (J \pm kdE)^2}}. \tag{7}$$

Figure 5 shows $\Gamma_{\pm}(k)/\omega_{\pm}(k)$ at different damping constants: $\alpha = 0.005$, $\alpha_c = 0.001$; $\alpha = 0.005$, $\alpha_c = 0.004$. As α_c has antidamping behaviour, the bigger this parameter is, the lower the ratio $\Gamma_{\pm}(k)/\omega_{\pm}(k)$.

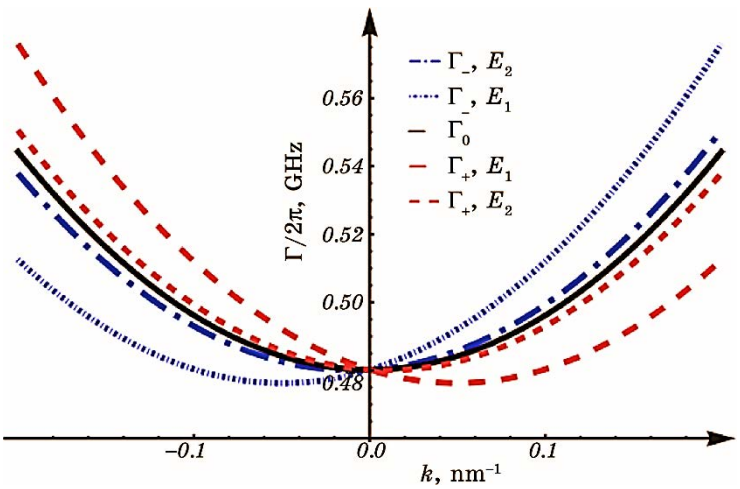

Fig. 3. The electric-field effect on the SWs' damping, Eq. (7): $E_1 = 50$ V/μm, $E_2 = 10$ V/μm. The black line corresponds to $\mathbf{E} = \mathbf{0}$. The damping parameters are $\alpha = 0.01$, $\alpha_c = 0.009$.

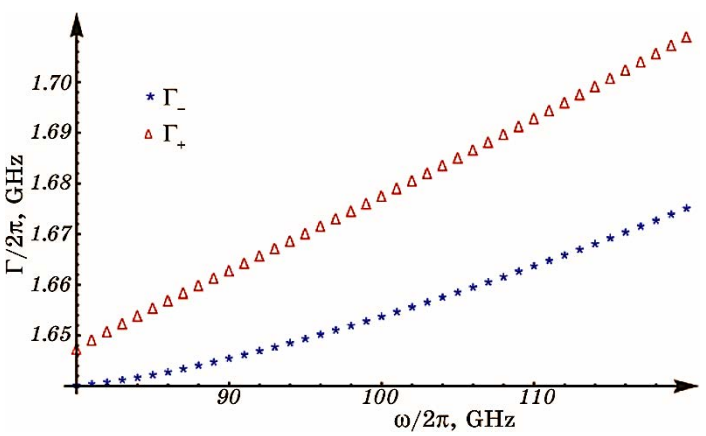

Fig. 4. Influence of the electric field, $E = 50$ V/μm, on the $\Gamma_{\pm}(k)$ magnitude at different values of the corresponding frequency $\omega_{\pm}(k)$. Here, we use the following damping parameters: $\alpha = 0.005$, $\alpha_c = 0.001$.

The peak of the function $\Gamma_{\pm}(k)/\omega_{\pm}(k)$ is shifted along the wave vector axis and proportional to the electric field.

The next factor to be paid attention to is the damping coefficients derived from Rayleigh-dissipation functional. Firstly, the existence of the intersublattice damping, α_c, directly allows the existence of the difference between the temporal attenuation of right- and left-handed polarizations' magnons. When $\alpha_c = 0$, $\Gamma_+(k) = \Gamma_-(k)$. So, the AC effect could

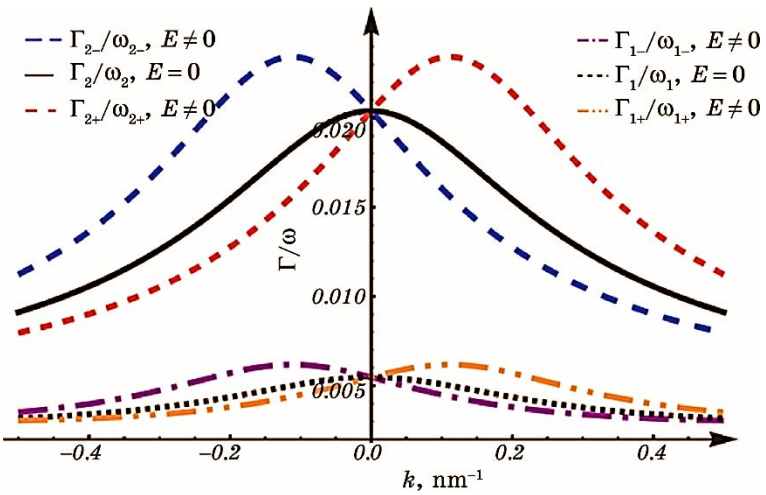

Fig. 5. The electric field $E = 50$ V/μm effect on the dependence $\Gamma_{\pm}(k)/\omega_{\pm}(k)$. The black lines (solid and dotted) correspond to $\mathbf{E} = \mathbf{0}$. Here, we use the next damping parameters: $\alpha = 0.005$, $\alpha_c = 0.004$ ($\Gamma_{1\pm}(k)/\omega_{1\pm}(k)$, dash-dotted lines); $\alpha = 0.005$, $\alpha_c = 0.001$ ($\Gamma_{2\pm}(k)/\omega_{2\pm}(k)$, short and long dashed lines).

help to detect intersublattice damping parameters experimentally.

In insulators, damping parameters could be small 10^{-3}–10^{-4} [21, 22], but the ratio between them can significantly change the dissipation. The coefficient α corresponds to the damping of magnetization dynamics, while α_c has antidamping behaviour. It was shown that these coefficients could be different by several orders of magnitude, at least in Mn-based antiferromagnets [23]. Authors [23] found that the damping coefficient derived from magnon pumping is greater than the Gilbert damping component. It means that a small difference should be between α and α_c, as $\alpha = \alpha_G + \alpha_{sp}$, $\alpha_c \approx \alpha_{sp}$. Thus, the authors [16, 23] point out the importance of taking into account the intersublattice damping.

To the best of our knowledge, there is a lack of similar research for AFM insulators, but we assume that there could be a noticeable difference between α_c and α.

The magnon lifetime is among the important parameters for practical applications. One could find it from the ratio $\tau(k, E) = 1/\Gamma(k, E)$. Figure 6 shows the magnon lifetime of right-handed $\tau_+(k, E)$ and left-handed $\tau_-(k, E)$ modes depending on the electric field. In the absence of an electric field $\tau_+ = \tau_-$, the higher the electric field, the bigger the difference between the magnon lifetimes of different modes. The lifetime difference between the right- and left-handed magnons, depending on the **E** field at different intersublattice parameters, is demonstrated in Fig. 7. The higher the α_c value, the greater the difference between the lifetimes of the right-handed and left-handed SWs.

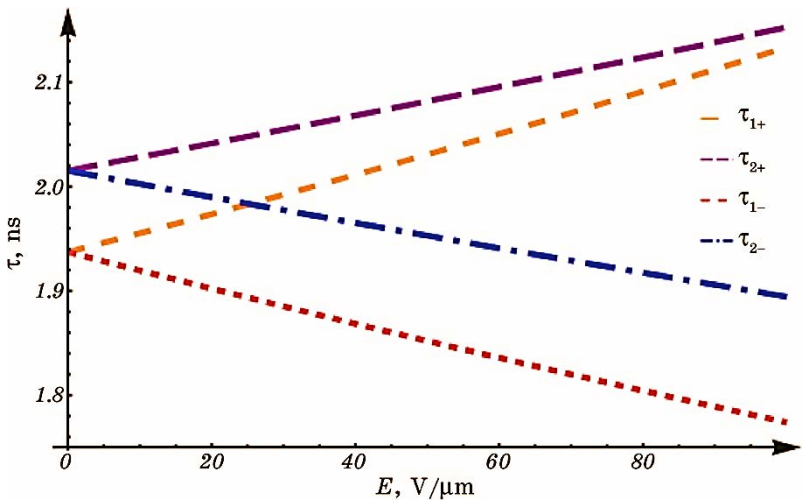

Fig. 6. The magnon lifetime of right-handed (τ_+) and left-handed (τ_-) modes depending on the electric field. $\tau_{1\pm}$ corresponds $k = 0.15$ nm^{-1}, $\tau_{2\pm}$ corresponds $k = 0.1$ nm^{-1}; $E = 50$ V/μm, the damping parameters are: $\alpha = 0.01$, $\alpha_c = 0.009$.

4. DISCUSSION

Condensed matter physics is undergoing a revolution by introducing concepts borrowed from topology to characterize the state and properties of a system. With the introduction of topology, the description of complex systems moves to characterizing their global quantities, which are measured non-locally and endow the system with global stability to disturbances. In magnetism, one vibrant example is the Berry phase—the additional phase that the system's wave function acquires, depending on the trajectory, which it passes [24]. The Aharonov–Casher effect, described in this article, is another special case of the topology phase. The main advantage of such topological effects is their independence from local perturbations, which makes them a very valuable parameter for quantum technologies, spintronics, and magnonics. We could expect that the AC effect will help to create topological magnons [12].

As previously demonstrated in Ref. [7], applying an electric field to an antiferromagnetic insulator, one could split the spin wave spectrum into two independent branches, which we have additionally demonstrated in the example of the system under consideration [13]. The spin waves with right-handed and left-handed polarization could propagate and attenuate separately. The splitting of the spin wave spectrum is achievable by applying a magnetic field, for example, with spin–orbit torque [25]. Nevertheless, an electric field could be a more efficient tool for controlling magnetism without requiring large magnetic

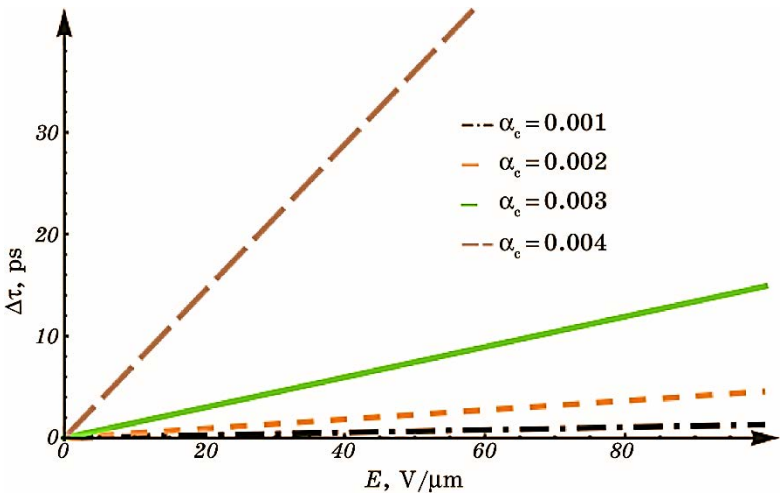

Fig. 7. The difference between the lifetimes of the right-handed and left-handed spin waves depending on the applied electric field at different damping coefficients α_c. Here, $\alpha = 0.005$, $k = 0.05$ nm^{-1}.

fields, which are energetically inefficient and challenging to integrate into nanoscale devices. Moreover, it is applicable for insulating magnetic materials.

There are several examples of practical applications of the AC effect in the SW field-effect transistor [7] or SW interferometric devices [8]. However, these works did not explore the impact of the AC-phase damping on magnon dynamics. Our results show that it could play a significant role in the dynamics of right-handed and left-handed polarized SWs. Considering topological effects like AC-induced without damping could lead to incomplete models that fail to capture real-world behaviour. Damping influences the lifetime and coherence of SWs, which could affect the efficiency of magnonic devices. For instance, the presence of damping can modify the nonreciprocal spin-wave propagation induced by the AC effect, altering its practical applications. Incorporating dissipation into theoretical and experimental studies is essential for accurately predicting device performance.

Integration of the topological effects in magnetism by electric-field control opens exciting prospects for energy-efficient, scalable technologies in spintronics and magnonics. The synergy between topological physics and electric-field-controlled SWs' characteristics is expected to revolutionize next-generation technologies, enabling faster, more energy-efficient, and highly integrative devices.

In conclusion, our work shows how the electric field affects the temporal attenuation of SWs in the insulating AFM. Damping of spin waves with right and left-handed polarizations could be manipulated

independently by the Aharonov–Casher effect. The higher the applied electric field, the more visible this difference. The Aharonov–Casher effect modifies spin-wave dynamics and allows the electric field to control propagation, magnon lifetime, attenuation, and energy of magnons. The difference between the dynamical features of right- and left-handed polarizations of SWs is mainly determined by the applied electric field and the spin–orbit coupling in the material. In contrast to ferromagnets, in antiferromagnets, electric fields allow the use of polarization as an additional degree of freedom, offering new opportunities for designing magnonic devices and topological spin wave logic elements.

This work was partially supported by the National Academy of Sciences of Ukraine through the research program No. 0125U000295 (Innovative materials for quantum sensing).

REFERENCES

1. V. V. Kruglyak, S. O. Demokritov, and D. Grundler, *J. Phys. D: Appl. Phys.*, **43**: 260301 (2010); https://doi.org/10.1088/0022-3727/43/26/260301
2. A. N. Mahmoud, F. Ciubotaru, F. Vanderveken, A. V. Chumak, S. Hamdioui, C. Adelmann, and S. D. Cotofana, *J. Appl. Phys.*, **128**: 161101 (2020); https://doi.org/10.1063/5.0019328
3. Y. Aharonov and A. Casher, *Phys. Rev. Lett.*, **53**: 319 (1984); https://doi.org/10.1103/PhysRevLett.53.319
4. V. N. Krivoruchko, *Low Temp. Phys.*, **46**: 820 (2020); https://doi.org/10.1063/10.0001548
5. Z. Cao, X. Yu, and R. Han, *Phys. Rev. B*, **56**: 5077 (1997); https://doi.org/10.1103/PhysRevB.56.5077
6. T. Liu and G. Vignale, *Phys. Rev. Lett.*, **106**: 247203 (2011); https://doi.org/10.1103/PhysRevLett.106.247203
7. R. Cheng, M. Daniels, J. G. Zhu, and D. Xiao, *Sci. Rep.*, **6**: 24223 (2016); https://doi.org/10.1038/srep24223
8. X. Zhang, T. Liu, M. E. Flatté, and H. X. Tang, *Phys. Rev. Lett.*, **113**: 037202 (2014); https://doi.org/10.1103/PhysRevLett.113.037202
9. R. O. Serha, V. I. Vasyuchka, A. A. Serga, and B. Hillebrands, *Phys. Rev. B*, **108**: L220404 (2023); https://doi.org/10.1103/PhysRevB.108.L220404
10. I. Dzyaloshinskii, *J. Phys. Chem. Solids*, **4**: 241 (1958); https://doi.org/10.1016/0022-3697(58)90076-3
11. T. Moriya, *Phys. Rev. Lett.*, **4**: 228 (1960); https://doi.org/10.1103/PhysRevLett.4.228
12. P. A. McClarty, *Annual Rev. Condens. Matter Phys.*, **13**: 171 (2022); https://doi.org/10.1146/annurev-conmatphys-031620-104715
13. O. Boliasova and V. Krivoruchko, *Phys. Rev. B*, **111**: 174440 (2025); https://doi.org/10.1103/PhysRevB.111.174440
14. R. Cheng, J. Xiao, Q. Niu, and A. Brataas, *Phys. Rev. Lett.*, **113**: 057601 (2014); https://doi.org/10.1103/PhysRevLett.113.057601
15. A. Kamra, R. E. Tronsoco, W. Belzig, and A. Brataas, *Phys. Rev. B*, **98**: 184402 (2018); https://doi.org/10.1103/PhysRevB.98.184402

16. H. Y. Yuan, Q. Liu, K. Xia, Z. Yuan, and X. R. Wang, *Europhys. Lett.*, **126**: 67006 (2019); https://doi.org/10.1209/0295-5075/126/67006
17. A. Kamra and W. Belzig, *Phys. Rev. Lett.*, **119**: 197201 (2017); https://doi.org/10.1103/PhysRevLett.119.197201
18. M. Dehmollaian and C. Caloz, *IEEE Trans. Antennas Propagation*, **69**, Iss. 10: 6531 (2021); https://doi.org/10.1109/TAP.2021.3061262
19. H. V. Gomonay and V. M. Loktev, *Phys. Rev. B*, **81**: 144427 (2010); https://doi.org/10.1103/PhysRevB.81.144427
20. L. Ryzsa, J. Hagemeister, E. Y. Vedmedenko, and R. Wiesendanger, *Phys. Rev. B*, **98**: 100404 (2018); https://doi.org/10.1103/PhysRevB.98.100404
21. P. Trempler, R. Dreyer, P. Geyer, C. Hauser, G. Woltersdorf, and G. Schmidt, *Appl. Phys. Lett.*, **117**: 232401 (2020); https://doi.org/10.1063/5.0026120
22. C. Dubs, O. Surzhenko, R. Linke, A. Danilewsky, U. Brückner, and J. Dellith, *J. Phys. D: Appl. Phys.*, **50**: 204005 (2017); https://doi.org/10.1088/1361-6463/aa6b1c
23. Q. Liu, H. Y. Yuan, K. Xia, and Z. Yuan, *Phys. Rev. Mater.*, **1**: 061401(R) (2017); https://doi.org/10.1103/PhysRevMaterials.1.061401
24. M. V. Berry, *Proc. Royal Society London A*, **392**: 45 (1984); https://doi.org/10.1098/rspa.1984.0023
25. Z. Yan, Z. Li, X. Wang, Z. Luo, Q. Xia, Y. Nie, and G. Guo, *Phys. Rev. B*, **108**: 134432 (2023); https://doi.org/10.1103/PhysRevB.108.134432

Metallophysics and Advanced Technologies
Металофіз. новітні технол.
Metallofiz. Noveishie Tekhnol.
2025, vol. 47, No. 6, pp. 595–600
https://doi.org/10.15407/mfint.47.06.0595
Reprints available directly from the publisher

PACS numbers: 75.30.Cr, 75.30.Kz, 75.40.Cx, 75.50.Bb, 75.50.Cc, 75.50.Mm, 81.40.Rs

Ferrimagnetic Properties of the $FeCr_2O_4$ Chromite and $TiFe_2O_4$ Titanomagnetite Minerals at High Temperatures

O. K. Kuvandikov, Z. M. Shodiev, Kh. B. Khasanov, B. A. Khairullaev, J. Sh. Akhtamov

Samarkand State University named after Sharof Rashidov,
15 University Blvd.,
UZ-140104 Samarkand, Uzbekistan

Temperature dependence of the magnetic susceptibility of the $FeCr_2O_4$ chromite and $TiFe_2O_4$ titanomagnetite minerals in the temperature range 300–1300 K is studied. Based on the experimental dependences, the magnetic parameters of the samples are calculated: Curie temperature, Curie–Weiss constant C, effective magnetic moment per one magnetic ion of the compound, and magnetic moment per formula unit of the sample. The results obtained are analysed in the light of available theoretical models.

Key words: magnetic susceptibility, chromite, titanomagnetite, magnetic moment, paramagnetic Curie temperature, Curie–Weiss constant.

Досліджено температурну залежність магнетної сприйнятливости мінералів хроміту $FeCr_2O_4$ та титаномагнетиту $TiFe_2O_4$ в інтервалі температур 300–1300 К. За експериментальними залежностями обчислено магнетні параметри зразків: температуру Кюрі, сталу Кюрі–Вейсса C, ефективний магнетний момент, що припадає на один магнетний йон сполуки, та магнетний момент, що припадає на формульну одиницю зразка. Одержані результати проаналізовано в світлі наявних теоретичних моделів.

Ключові слова: магнетна сприйнятливість, хроміт, титаномагнетит, магнетний момент, парамагнетна температура Кюрі, стала Кюрі–Вейсса.

Corresponding author: Obokul Kuvandikov
E-mail: quvandikov@rambler.ru

Citation: O. K. Kuvandikov, Z. M. Shodiev, Kh. B. Khasanov, B. A. Khairullaev, and J. Sh. Akhtamov, Ferrimagnetic Properties of the $FeCr_2O_4$ Chromite and $TiFe_2O_4$ Titanomagnetite Minerals at High Temperatures, *Metallofiz. Noveishie Tekhnol.*, **47**, No. 6: 595–600 (2025). DOI: 10.15407/mfint.47.06.0595

(Received 2 February, 2024; in final version, 8 October, 2024)

1. INTRODUCTION

The fundamental difference between an iron-containing mineral and a rock is that the mineral, both in terms of its chemical composition and its physical properties, is a relatively homogeneous body, while rocks are aggregates of minerals consisting of a number of mineral components [1].

The physics of magnetism is able to predict the magnetic properties of materials from their structure; this also applies to rocks. However, this approach is not optimal: it requires an in-depth study of the structural characteristics of the substance, which is not available in geophysical research. On the other hand, measuring the magnetic properties of rocks is not difficult even with a large number of samples [2]. The nature of the magnetism of rocks and the characteristics of the factors that determine the patterns of distribution of the magnetic properties of various rocks must be supplemented with empirical data for the most common minerals of rocks and ores that cause magnetic anomalies [3, 4].

The magnetic states of rocks and ores are of particular interest for the physics of magnetic phenomena, since, due to the complex crystal structure, the magnetic structures of these minerals are necessary for understanding their key features [5]. There is little experimental data on the magnetic properties and electronic structure of rock minerals at high temperatures.

The study of the magnetic properties of rock minerals from the perspective of a mineralogist is extremely important. To date, the magnetic properties of these minerals have been studied mainly in their magnetically ordered state, while their paramagnetic state has been almost unstudied [6].

To date, the temperature dependence of the paramagnetic susceptibility $\chi(T)$ of pure iron has been measured in detail by many researchers [7–9] in a wide temperature range covering its liquid state and interpreted on the basis of the polymorphic and magnetic phase transitions occurring in iron. According to the results of these studies, the dependence $\chi^{-1}(T)$ of iron is complex. χ^{-1} grows abruptly at the temperature of the ferromagnet-paramagnet magnetic phase transition (Θ_p = 1043 K); χ^{-1} increases linearly in the temperature range 1043–1183 K, and at the polymorphic transition α-Fe (b.c.c.)$\rightarrow\gamma$-Fe (f.c.c.) (at 1183 K) decreases abruptly; in the temperature range 1183–1665 K, it increases linearly, and during the polymorphic transition γ-Fe (f.c.c.) $\rightarrow\delta(\alpha)$-Fe (b.c.c.) (at 1665 K), it decreases abruptly; it increases in the temperature range 1665–1809 K linearly, during melting (1809 K) abruptly, and then linearly. By now, the magnetic properties of the compound of iron with non-magnetic metals at high temperatures have

been little studied. This is due to the difficulty of making precision magnetic measurements at high temperatures.

The purpose of this work is to study experimentally the $\chi(T)$ dependence of the iron-containing minerals chromite and titanomagnetite included in the rocks of Uzbekistan. The dependences $\chi(T)$ were measured by the Faraday method using high-temperature vertical pendulum balances in Al_2O_3 crucibles and in an excess atmosphere of purified helium in the high temperature range 300–1300 K. The maximum relative measurement error for χ did not exceed 3% [8–11]. Rock (mineral) samples were obtained from the Central Research Laboratory of the Navoi Mining and Metallurgical Combine.

2. EXPERIMENTAL RESULTS AND DISCUSSION

The dependences $\chi(T)$ were measured in the temperature range 300–1200 K for chromite and 900–1300 K for titanomagnetite (Fig. 1).

Analysis of Fig.1 shows that, for the studied minerals of chromite and titanomagnetite, χ decreases with raising temperature, but the temperature dependence is complex [12].

The measurement results are shown in Fig. 2 in the form of $\chi^{-1}(T)$ dependence.

In Figure 2, it can be seen that the $\chi^{-1}(T)$ dependences of the minerals chromite and titanomagnetite in the studied temperature range have a nonlinear complex character: the slope ($d\chi^{-1}/d\,T$) of the $\chi^{-1}(T)$ dependence for chromite at approximately 823 K sharply increases, and at 933 K, it decreases; for titanomagnetite at 1043 K, it sharply increases, and at 1173 K, it decreases. The $\chi^{-1}(T)$ dependence for chromite in the temperature ranges 300–823 K and 933–1173 K, and for titanomagnetite in the temperature ranges 923–1043 K and 1183–

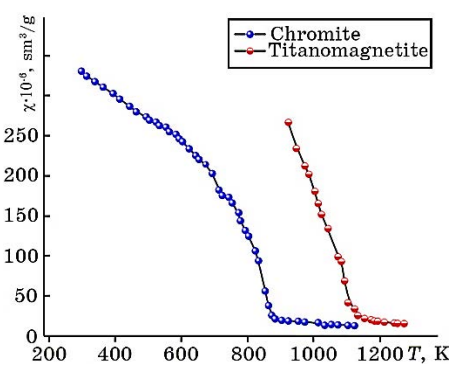

Fig.1. Dependences $\chi(T)$ of the studied samples of chromite $FeCr_2O_4$ and titanomagnetite $TiFe_2O_4$.

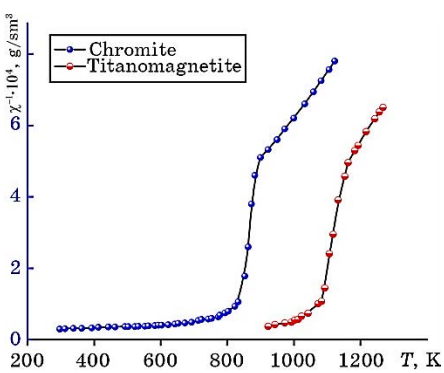

Fig.2. $\chi^{-1}(T)$ dependences of the studied chromite $FeCr_2O_4$ and titanomagnetite $TiFe_2O_4$ samples.

1273 K, they are linear.

The linear nature of $\chi^{-1}(T)$ dependence in the specified temperature range indicates that these dependences obey the Curie–Weiss law:

$$\chi = \frac{C}{T - \Theta_p}, \quad (1)$$

where C is the Curie–Weiss constant, Θ_p is the paramagnetic Curie temperature.

Changes in the experimental dependences $\chi^{-1}(T)$ of the samples under study can be explained by the results described above for pure iron [7, 8, 11]. The complex nature of $\chi^{-1}(T)$ dependence of pure iron is uniquely reflected in $\chi^{-1}(T)$ dependences of the studied iron-based compounds depending on temperature and the composition of nonmagnetic elements (O).

Consequently, changes in the $\chi^{-1}(T)$ dependences of the studied samples occur due to magnetic and structural (polymorphic) phase transitions that occur in them at certain temperatures [13]. In chromite at 823 K, there is the structural transition f.c.c.→b.c.c. in its cubic lattice. In titanomagnetite at 1043 K, there is the structural transition f.c.c.→b.c.c. in its cubic lattice. These phase transitions are reflected in the $\chi^{-1}(T)$ dependence of chromite $FeCr_2O_4$ and titanomagnetite $TiFe_2O_4$ (Fig. 2) in the form of jumps at the temperatures of these transitions. Changes in the $\chi^{-1}(T)$ dependence in the studied minerals can only be explained by structural (polymorphic) transitions that occur at higher temperatures in Fe sublattices of these minerals [7,8].

From the experimental $\chi^{-1}(T)$ dependences for the studied samples, we calculated their main paramagnetic characteristics: Curie–Weiss constants C, paramagnetic Curie temperature Θ_p, and magnetic moment per mineral chemical formula μ_{for}. The calculation results are shown in Table. Information for pure iron in Table was obtained from [8]. Analysis of the table shows that the magnetic characteristics (Θ_p and μ_{for}) of the studied compounds are smaller compared to the magnetic characteristics of pure iron. This can be explained by an increase in the distance between the magnetic iron ions located at the sublattice sites of the studied compounds. Due to this reason, the magnetic exchange interaction of electrons in the $3d$-shell of iron ions, which are responsible for the occurrence of magnetic ordering of the studied compounds, decreases. Θ_p is an energy measure of the exchange interaction.

Table shows that the values Θ_p for the studied minerals are lower compared to the values for pure iron ($\Theta_p = 1043$ K). This is explained by the fact that, if Fe^{3+} ions are partially or completely replaced by Cr^{3+} and Ti^{4+} ions in the crystal lattice of minerals, which in both structures show a strong tendency to occupy octahedral positions, this will lead to

TABLE. Calculation results.

Mineral	Temperature interval, K	Θ_p, K	C, 10^4 sm^3·g^{-1}·K	μ_{for}, μ_B
Fe	1043–1183	1050	28,1	3.54
	1183–1665	–2027	90	6.47
	1665–1809	1100	25	3.34
Chromite $FeCr_2O_4$	300–820	60	1340	15.51
	930–1170	520	72.05	3.59
Titanomagnetite $TiFe_2O_4$	920–1040	850	250	7.48
	1180–1270	910	55.56	3.5

a significant decrease in the Curie temperature.

The distribution of cations between octahedral and tetrahedral positions in the titanomagnetite lattice has been the subject of extensive discussion [14]. According to neutron diffraction data, most of Ti^{4+} ions are located in octahedral positions. The spin moments of octahedral and tetrahedral ions are directed in opposite directions. As the number of Ti^{4+} ions increases, the Néel point decreases. Fe^{3+} prefers for octahedral sites, the actual distribution between octahedral and tetrahedral sites may depend on both temperature and composition.

4. CONCLUSIONS

Based on the results obtained, the following conclusions can be drawn. For the first time, the $\chi^{-1}(T)$ dependences of iron-containing minerals, chromite $FeCr_2O_4$ and titanomagnetite $TiFe_2O_4$, were measured at high temperatures. It has been established that these $\chi^{-1}(T)$ dependencies obey the linear Curie–Weiss law.

Based on the experimental dependences of the studied minerals, their main paramagnetic characteristics were determined.

REFERENCES

1. N. A. Toropov and L. N. Bulak, *Kristallografiya i Mineralogiya* [Crystallography and Mineralogy] (Moskva: Stroyizdat: 1972) (in Russian).
2. G. P. Kudryavtseva, *Ferrimagnetizm Naturalnyh Oksidov* [Ferrimagnetism of Natural Oxides] (Moskva: Nedra: 1988) (in Russian).
3. J. A. Grisales Ceryn, D. A. Landínez Téllez, and J. Roa-Rojas, *Journal of Electronic Materials*, **2**: 822 (2021).
4. V. I. Trukhin and V. I. Maksimochkin, *Moscow University. Series 3. Physics. Astronomy*, **1**: 68 2008 (in Russian).
5. A. Singh, R. Dawn, V. K. Verma, D. Panda, S. K. Sahoo, K. Kumar, and

V. R. Singh, *Physica B: Condensed Matter*, 647: 414373 (2022).
6. S. Krupichka, *Fizika Ferritov i Rodstvennykh Im Magnitnykh Okislov* [Physics of Ferrites and Related Magnetic Oxides] (Moskva: Mir: 1976) (Russian translation).
7. E. G. Nevzerova, B. P. Geltekov, I. Z. Radovsky, and P. V. Geld, *News from Universities. Ferrous metallurgy*, **9**: 105 (1972) (in Russian).
8. O. K. Kuvandikov, K. O. Shakarov, and Z. M. Shodiev, *J. Commun. Technol. Electron.*, **52**: 1058 (2007).
9. O. K. Kuvandikov, *Magnitnyye i Kineticheskie Svoistva Kondensirovannykh Splavov i Soyedineniy na Osnove Perekhodnykh i Redkozemel'nykh Metallov* [Magnetic and Kinetic Properties of Condensed Alloys and Compounds Based on Transition and Rare Earth Metals] (Tashkent: Fan: 2009) (in Russian).
10. K. V. Vasin and M. V. Eremin, *JMMM*, **537**: 168185 (2021).
11. O. K. Kuvandikov, Kh. O. Shakarov, and K. M. Irgashev, *Optiko-Akusticheskie, Elektricheskie, Magnitnyye Issledovaniya Kondensirovannykh Sred* [Optical-Acoustic, Electrical, Magnetic Studies of Condensed Matter] (Samarkand: 1982) (in Russian).
12. O. K. Kuvandikov, K. H. Shakarov, Z. M. Shodiev, and G. R. Rabbimova, *J. of Communications Technology and Electronics*, **52**, 9: 1062 (2007).
13. O. K. Kuvandikov, Kh. O. Shakarov, Z. M. Shodiev, and Kh. B. Khasanov "*Mountain Herald" of Uzbekistan*, **4**, No. 67: 84 (2016) (in Russian).
14. R.T. Shui, *Poluprovodnikovyye Rudnyye Mineraly* [Semiconductor Ore Minerals] (Leningrad: Nedra: 1979) (in Russian).

Metallophysics and Advanced Technologies
Металофіз. новітні технол.
Metallofiz. Noveishie Tekhnol.
2025, vol. 47, No. 6, pp. 601–617
https://doi.org/10.15407/mfint.47.06.0601
Reprints available directly from the publisher

PACS numbers: 05.70.Ce, 62.20.de, 62.50.-p, 64.30.Jk, 65.40.De, 91.32.Gh, 91.60.Gf

Exploring the High-Pressure Equation of State in Earth's Mantle with a Focus on the $MgSiO_3$–MgO System

S. Gaurav, S. Shankar*, Arvind Mishra**, S. Kanwar, and Pratibha K

Department of Applied Physics, Amity University,
Amity Road, Sector 125,
122413 Noida, India
**Experimental Research Laboratory, Department of Applied Physics,*
ARSD College, University of Delhi,
Dhaula Kuan Enclave I,
110021 New Delhi, India
***Department of Applied Science and Humanities,*
G. L. Bajaj Institute of Technology and Management,
201303 Noida, India

The thermodynamic characteristics of the $MgSiO_3$–MgO system are determined using a modified form of the Shanker equation of state (EOS) known as the 'Higher Order Shanker (HOS) EOS'. This adaptation incorporates higher-order terms into the Shanker EOS. The Higher Order Shanker (HOS) EOS is evaluated against Stacey criteria to ensure consistency in the variation of the pressure dependence of the isothermal bulk modulus. In a comparative analysis, the thermodynamic properties obtained from the Higher Order Shanker (HOS) EOS are contrasted with those derived from established classical EOS models, alongside electronic contribution analysis. This demonstrates the reliability of the proposed Higher Order Shanker (HOS) EOS for computing thermodynamic properties for similar systems under higher pressures. Furthermore, expressions for the bulk modulus and its pressure derivatives are formulated and extended to the theoretical limit of infinite pressure. These

Corresponding author: Sharma Gaurav
E-mail: gsharma6@amity.edu, s.gaurav29june@gmail.com

Citation: S. Gaurav, S. Shankar, Arvind Mishra, S. Kanwar, and Pratibha K, Exploring the High-Pressure Equation of State in Earth's Mantle with a Focus on the $MgSiO_3$–MgO System, *Metallofiz. Noveishie Tekhnol.*, **47**, No. 6: 601–617 (2025). DOI: 10.15407/mfint.47.06.0601

derived expressions are valuable for conducting more intricate analysis of higher-order thermoelastic properties.

Key words: equation of state, Stacey criteria, thermal expansion, Grüneisen parameter.

Термодинамічні характеристики системи $MgSiO_3$–MgO визначено з використанням модифікованої форми Шенкерового рівняння стану, відомого як «Шенкерове рівняння з урахуванням вищих порядків». Ця адаптація включає члени вищого порядку Шенкерового рівняння стану. Шенкерове рівняння з врахуванням вищих порядків оцінено за критеріями Стейсі, щоб забезпечити узгодженість у зміні залежности ізотермічного об'ємного модуля від тиску. У порівняльній аналізі термодинамічні властивості, одержані з Шенкерового рівняння з урахуванням вищих порядків, порівняно з термодинамічними властивостями, одержаними з відомих класичних моделів Шенкерового рівняння стану, а також з аналізою електронних внесків. Це демонструє надійність запропонованого методу Шенкерового рівняння з врахуванням вищих порядків для розрахунку термодинамічних властивостей подібних систем за високих тисків. Крім того, сформульовано вирази для об'ємного модуля та його похідних за тиском, які поширено на теоретичну границю нескінченного тиску. Ці одержані вирази є цінними для проведення більш складної аналізи термопружніх властивостей вищих порядків.

Ключові слова: рівняння стану, критерії Стейсі, теплове розширення, Грюнайзенів параметер.

(Received 16 January, 2024; in final version, 25 September, 2024)

1. INTRODUCTION

The exact thermodynamic behaviour of the $MgSiO_3$–MgO system as one of the component of the Earth's lithosphere is the field of interest for modern mineralogical researches. Since 2004 [1, 2], when $MgSiO_3$–MgO was known to be the ultimate phase of the lower mantle of the Earth, different studies are carried out on its thermodynamic properties and its phase boundary conditions, so as to know more about the *D*-layer of Earth in seismological scenario and are nowadays used as input for geodynamics studies heling us to develop the theory regarding plate tectonics which explain the formation of Earth's lithosphere. Equations of state (EOS) is the powerful tool for the exact determination of thermodynamic variables in terms of pressure, volume and temperature and it is also found helpful for studying the compressibility and pressure induced phase transitions for geophysical minerals at high pressures and temperatures [4–6].

The properties of geophysical minerals at extreme pressures and temperatures recently estimated from EOS's are obtained by simplifying basic thermodynamic expressions like bulk modulus and thermal

expansion taking into account of electronic contribution due to Helmholtz free energy and the properties thus computed by varying temperature and pressure conditions are found to have low precision due to its limitation as reported earlier for B–M EOS for solids for higher compressions. This drawback was overcome by proposing EOS universally [10] for solids having distinct kind of chemical bonding at extremely high compressions. The dependences of potential energy $E = E(r)$ (r being the interatomic distance) were in agreement with Rydberg's model of EOS [11, 12].

An EOS based on volume dependent short-range forces in case of interatomic potentials was developed by Shanker *et al.* [13, 14]. However, the results reported earlier [7, 13] were not consistent with the results of Hama Suito EOS [15] derived from the first principle and based on quantum statistical model (QSM-Model) and linearized augmented plane wave method (APW-Method). In view of recent findings about EOS based on potential energy function, focused studies are being made to frame new EOS and require critical assessment to overcome the present challenges of the Earth interior.

For achieving better consistency with the results of Hama Suito, in the present endeavour, the previous developed Shanker EOS [13] has been modified by considering the effect of the higher-order terms of V/V_0, which were excluded in Shanker EOS. The consistency of modified EOS has been mapped with Hama Suito to follow the essential Stacey criteria for pressure dependent bulk modulus dK_T/dP at constant temperature as a function of P/K_T; K_T being the isothermal bulk modulus at pressure P. For rigorous consistency, the derived EOS has been subjected to polymorphic lower mantle material $MgSiO_3$–MgO. This system is of great importance as it provides understanding of evolution of the Earth and helps in comprehending the seismic profile of the Earth. In addition to this, the correctness of modified EOS is verified by comparing the results with (*a*) B–M EOS, (*b*) Vinet–Rydberg EOS, (*c*) Shanker EOS, and (*d*) Stacey EOS.

The thermodynamic properties obtained using modified Shanker EOS known as 'Higher Order Shanker (HOS) EOS' will be useful for various applications of Geosciences and specially to the Earth's behaviour at extreme conditions. For consistency of modify EOS, we have to calculate the values of first-, second-, and third-order Grüneisen parameter using to Stacey EOS and Modified EOS (HOS EOS) values under high compressions.

2. MODIFICATIONS OF SHANKER EOS

Shanker EOS representing the relationship between P and V/V_0 can also be obtained using the volume dependence. The volume dependent force constant is approximated [15] as

$$A = A_0 f\,, \tag{1}$$

where A_0 does not depend on volume and f is volume or compression V/V_0 dependent. Now, using Shanker's approach [16] the expression of P is given by

$$P\left(\frac{V}{V_0}\right)^{4/3} = -\frac{K_0}{f_0 V_0}\int_{V_0}^{V} f dV\,. \tag{2}$$

Equation (2) is the basic equation, which assists in deriving the EOS. Shanker EOS has been obtained [17] using following form for f:

$$f = (1 + y + y^2)\exp(ty)\,, \tag{3}$$

where $y = 1 - \frac{V}{V_0}$ and t is the constant. For $V = V_0$, $f = f_0 = 1$.

Equation (3) is substituted in (2) as

$$P\left(\frac{V}{V_0}\right)^{4/3} = -\frac{K_0}{f_0 V_0}\int_{V_0}^{V} f dV\,. \tag{4}$$

For getting more closer results with Hama Suito results at high compressions, we replaced the value of f inducing the higher-order terms as given by

$$f = (1 + y + y^2 + y^3)\,. \tag{5}$$

Using (4) and (5) resulted in the modified Shanker EOS named as Higher Order Shanker (HOS) EOS.

EOS.

$$P = K_0\left(V/V_0\right)^{-4/3} \times$$
$$\times\left[\left(1 - \frac{1}{t} + \frac{2}{t^2} - \frac{6}{t^3}\right)\left\{\exp\left(ty\right) - 1\right\} + y\left(1 + y - \frac{2}{t} + y^2 - \frac{3y}{t} + \frac{6}{t^2}\right)\exp\left(ty\right)\right], \tag{6}$$

$$K_T = K_0\left(\frac{V}{V_0}\right)^{-\frac{1}{3}}\left(1 + y + y^2 + y^3\right)\exp\left(ty\right) + \frac{4}{3}P\,, \tag{7}$$

$$K_T' = \frac{4}{3} + \left(1 - \frac{4}{3}\frac{P}{K_T}\right)\left[\frac{1}{3} + \frac{V}{V_0}\left\{t + \frac{\left(1 + 2y + 3y^2\right)}{\left(1 + y + y^2 + y^3\right)}\right\}\right], \tag{8}$$

where $t = K_0' - \frac{8}{3}$ and $y = 1 - \frac{V}{V_0}$.

The above-mentioned mathematical relations expressed for P, K_T and K_T' are employed to investigate pressure dependent properties in the present study and the results obtained are explained in the subsequent section.

3. RESULTS AND DISCUSSION

We have obtained pressure P (cold pressure or pressure at reference isotherm) and isothermal bulk modulus K_T for $MgSiO_3$–MgO system (Forsterite, Wadsleyite, Ringwoodite, Perovskite, Akimotoite, and Post-perovskite) taking the input data of K_0, K_0' and K_T'' of earlier work [22]. The expressions obtained from various EOSs are written below.

B–M EOS.

$$P = \frac{3}{2}K_0\left(x^{-7} - x^{-5}\right)\left[1 + \frac{3}{4}A_1\left(x^{-2} - 1\right)\right], \tag{9}$$

$$K_T = \frac{1}{2}K_0\left(7x^{-7} - 5x^{-5}\right) + \frac{3}{8}A_1\left(9x^{-9} - 14x^{-7} + 5x^{-5}\right), \tag{10}$$

$$K_T' = \frac{K_0}{8K_T}\left[\left(K_0' - 4\right)\left(81x^{-9} - 98x^{-7} + 25x^{-5}\right) + \frac{4}{3}\left(49x^{-7} - 25x^{-5}\right)\right], \tag{11}$$

where $x = \left(\frac{V}{V_0}\right)^{1/3}$ and $A_1 = K_0' - 4$.

VINET (Rydberg) EOS.

$$P = 3K_0x^2(1-x)\exp\left[\frac{3}{2}(K_0' - 1)(1-x)\right], \tag{12}$$

$$K_T = K_0x^2\left[1 + \left\{\frac{3}{2}(K_0' - 1)x + 1\right\}(1-x)\right]\exp\left[\frac{3}{2}(K_0' - 1)(1-x)\right], \tag{13}$$

$$K_T' = \frac{1}{3}\left[\frac{x\left(1-\eta\right) + 2\eta x^2}{1 + \left(\eta x + 1\right)\left(1-x\right)} + \eta x + 2\right], \tag{14}$$

where $x = \left(\frac{V}{V_0}\right)^{1/3}$ and $\eta = \frac{3}{2}\left(K_0' - 1\right)$.

SHANKER EOS.

$$P = K_0\left(\frac{V}{V_0}\right)^{-4/3}\left[\left(1 - \frac{1}{t} + \frac{2}{t^2}\right)\left\{\exp\left(ty\right) - 1\right\} + y\left(1 + y - \frac{2}{t}\right)\exp\left(ty\right)\right], \tag{15}$$

$$K_T = K_0 \left(\frac{V}{V_0}\right)^{-\frac{1}{3}} \left(1 + y + y^2\right) \exp\left(ty\right) + \frac{4}{3} P, \tag{16}$$

$$K_T' = \frac{4}{3} + \left(1 - \frac{4}{3}\frac{P}{K_T}\right)\left[\frac{1}{3} + \frac{V}{V_0}\left\{t + \frac{\left(1+2y\right)}{\left(1+y+y^2\right)}\right\}\right], \tag{17}$$

where $t = K_0' - \frac{8}{3}$ and $y = 1 - \frac{V}{V_0}$.

Stacey [18, 19] has established an innovative method representing $K' = \frac{dK'}{dP}$ with the dependence with $\frac{P}{K}$. Stacey deduced reciprocal of K' as mentioned below:

$$\ln\left(\frac{V}{V_0}\right) = \frac{K_0'}{K_\infty'^2} \ln\left(1 - K_\infty' \frac{P}{K}\right) + \left(\frac{K_0'}{K_\infty'} - 1\right)\frac{P}{K}, \tag{18}$$

$$\frac{K}{K_0} = \left(1 - K_\infty' \frac{P}{K}\right)^{-\frac{K_0'}{K_\infty'}}, \tag{19}$$

$$\frac{1}{K'} = \frac{1}{K_0'}\left(1 - \frac{K_\infty'}{K_0'}\right)\frac{P}{K}. \tag{20}$$

Several attempts have been to formulate the equations of state. However, they fail to satisfy the Stacey's criterion [8, 19] Shanker EOS and Higher Order Shanker (HOS) EOS, B–M EOS and Vinet EOS are nearly linear supporting the validity of Stacey equations (linear or exponential form).

In addition, the polymorphic $MgSiO_3$–MgO system (Forsterite, Wadsleyite, Ringwoodite, Perovskite, Akimotoite, and Postperovskite) and their compressibility and phase transitions were studied by using the different EOSs. Phase equilibria in the $MgSiO_3$–MgO system play a major contribution in the interpretation of the seismic profile of Earth's mantle. Recently, it was observed that olivine (OI) structure converted into Wadsleyite (Wds) structure at the distance of 410 km existing at 14–15 GPa and at the depth of 520 km at 17–18 GPa is categorised by Wadsleyite–Ringwoodite (Rwd) transition [21]. The low boundary present in the upper mantle (550–670 km) around 23–24 GPa is often designated to Ringwoodite (Rwd) to Mg, Perovskite, and Ferropericlase (or Magnesiowistite) transition. This 'layer *D*' can be perceived above the core–mantle boundary using seismic data studies. Such type of studying is done by experimentally and an initial calculation. In the present work, measurements of *P*–*V*–*T* properties were us-

TABLE 1. Values of input data for $MgSiO_3$–MgO System.

Phase	K_0	K_0'	γ_0	$\alpha_0 \times 10^{-6}(K^{-1})$
Forsterite	127.4	4.30	1.066	22.599
Wadsleyite	169.0	4.14	1.185	20.295
Ringwoodite	187.4	3.98	1.210	18.909
Perovskite	252.0	4.38	1.700	22.594
Akimotoite	215.3	4.91	2.000	27.584
Postperovskite	253.7	4.03	1.670	22.274

ing Equations of State and the validity of the proposed equations of state is tested for $MgSiO_3$–MgO system. Subsequently, after assessment of EOSs, we have also studied the equilibria of the transitions OI to Wds, and Rwd to Bdg + Per.

The input data on K, K_0', γ and γ_0 as used [21, 22] for assessment of EOSs are tabulated in Table 1 with $K_\infty' = 2.41$ (for lower mantle). We have observed the variation of pressure (P), isothermal bulk modulus (K_T) and their derivative with compression (K_T') and shown in Fig. 1–6, (a–c). The results for obtained equations of state are strongly matched with measured data and are found to be consistent.

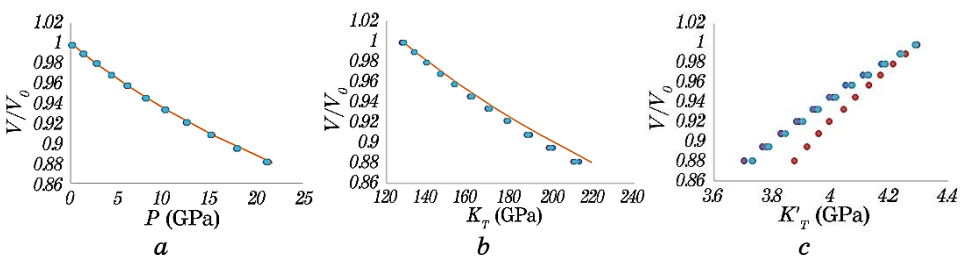

Fig. 1. Variation of pressures (a), K_T (b), K_T' (c) with compression for Forsterite.

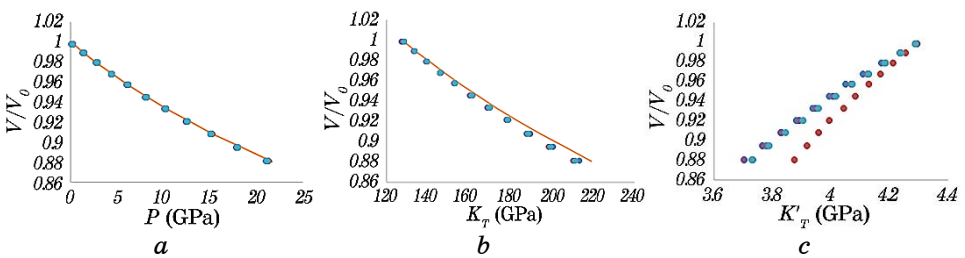

Fig. 2. Variation of pressures (a), K_T (b), K_T' (c) with compression for Wadsleyite.

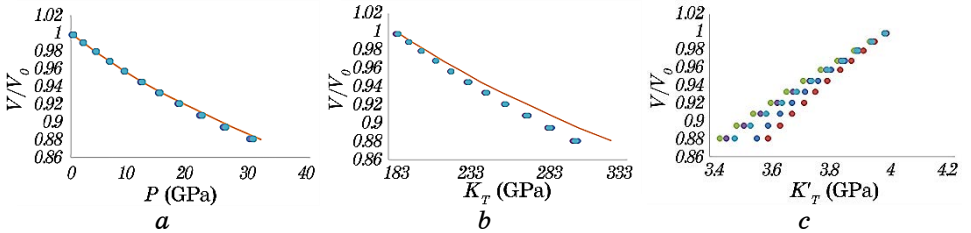

Fig. 3. Variation of pressures (*a*), K_T (*b*), K'_T (*c*) with compression for Ringwoodite.

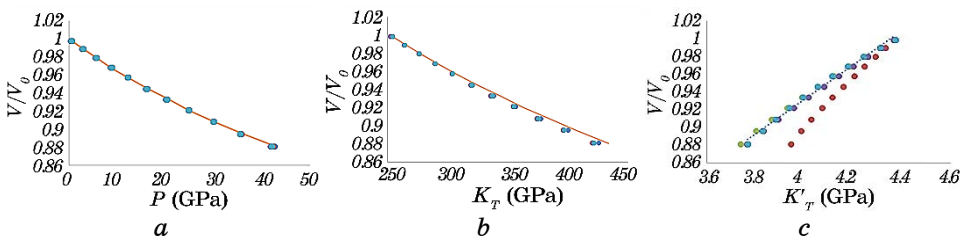

Fig. 4. Variation of pressures (*a*), K_T (*b*), K'_T (*c*) with compression for Perovskite.

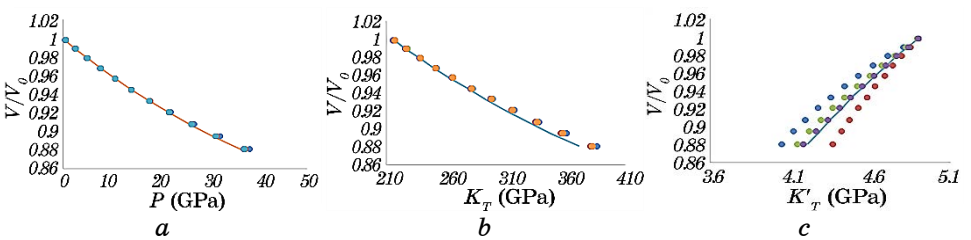

Fig. 5. Variation of pressures (*a*), K_T (*b*), K'_T (*c*) with compression for Akimotoite.

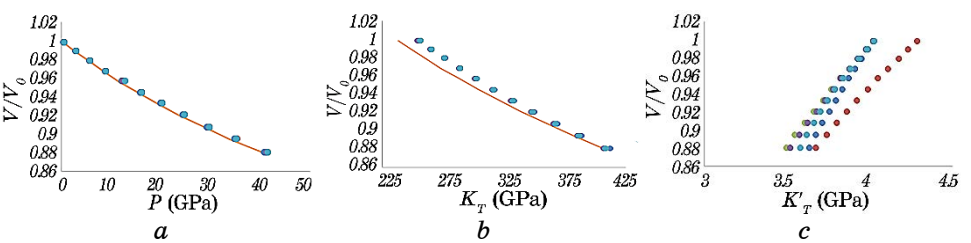

Fig. 6. Variation of pressures (*a*), K_T (*b*), K'_T (*c*) with compression for Postperovskite.

In addition, the results of pressure K_T and K_T' are also in good agreement with previously reported data computed using thermodynamic model (electronic configuration) approach equations [21, 22] and are labelled as R_{ef} in Fig. 1–6, (*a*–*c*).

The B–M EOS is based on Euler's strain theory and the Vinet (Rydberg) EOS is based on the Rydberg potential function. Shanker EOS is derived from the near force constant related to the potential energy derivative [10, 11].

Values of K_0 and K_0' used in the present calculations are given in Table 1. The results for P, K_T and K_T' as functions of V/V_0 down to 0.1 are given in Fig. 1–6, (*a*–*c*). Stacey argued that results based on B–M EOS, Vinet (Rydberg) EOS, and Shanker EOS agree well with results for Forsterite, Perovskite, Akimotoite, and Postperovskite studied up to high compressions. For Wadsleyite and Ringwoodite, the results obtained from Shanker EOS are relatively close to those based on the electron contribution equation [21, 22], but fail up to very high compressions. However, the results obtained from Higher Order Shanker EOS (HOS), which uses higher-order terms in this study, are more consistent up to higher-order compression, supporting their claim [21, 22] and further analysis help.

$MgSiO_3$–MgO System

It is evident from Figs. 1–6, (*a*–*c*) that the values of P and K_T calculated from Eqs. (6) and (7) present close agreement with the values obtained from the HOS EOS, which is consistent with the Stacey EOS and Electronic contribution equation [21, 22] results for the entire range of compressions.

On the other hand, the results obtained from the B–M third-order EOS, the B–M EOS, and the Vinet EOS deviate substantially from the Electronic contribution equation [21, 22] at higher compressions; V/V_0 is somewhat less than 0.80.

An advantage of the present EOS is that it can be written in the inverted form also, *i.e.*, V/V_0 as a function of pressure. We have studied the range of applicability of the present EOS for various solids with different values of K_0'. It has been found that the present EOS is valid up to very high compressions for a material with $K_0' < 4$ (Ringwoodite—Fig. 3, *a*–*c*). For materials with $4 < K_0' < 4.38$, (such as Forsterite, Wadsleyite, and Postperovskite) the EOS holds good down to a compression of $V/V_0 = 0.85$. In the case of solids with $K_0' \geq 4.38$, such as Perovskite and Akimotoite, the present EOS holds good only for small compressions down to about $V/V_0 = 0.85$.

For the Earth's lower mantle, we have $K_0' < 4$ [1], and therefore the present EOS is suitable for studying the variation of densities with pressure for the entire depth of the lower mantle.

Variation of First-, Second-, and Third-Order Grüneisen Parameter with Pressure

The ratio of γ is a vital quantity in condensed matter physics as well as Shockwaves and the field of geophysics. The anharmonicity of solids is directly linked to the Grüneisen parameter. The greater the value of γ, the greater is its anharmonic nature.

Important parameters like pressure as well as temperature of the metal and core [8, 25]. One way to get the perfect EOS for a solid from their response to shock-wave loading is to use a specific form of this dependence in conjunction with Hugoniot shock. That is why it is important to achieve an independent form of Hugoniot shock or isotherm. The Grüneisen ratio, used in shock physics, has not been done so far. Therefore, the purpose of the present work we have to find the anharmonic behaviour of Forsterite, Wadsleyite, Ringwoodite, Perovskite, Akimotoite, and Postperovskite using the values (P, K_T and K_T') obtained by HOS.

The Stacey K-primed equation given below:

$$\frac{1}{K'}=\frac{1}{K_0'}+\left(1-\frac{K_\infty'}{K_0'}\right)\frac{P}{K}. \tag{21}$$

The expressions for higher-order pressure derivatives obtained from (2) due to Stacey [20] are written as follows:

$$KK''=-\left(\frac{K''^2}{K_0'}\right)\left(K'-K_\infty'\right). \tag{22}$$

The expressions of γ based on Shanker *et al.* [27] are given below:

$$\frac{1}{\gamma}=A+B\frac{P}{k}, \tag{23}$$

where A and B are material dependent constants:

$$A=1/\gamma_0, \tag{24}$$

$$B=K_\infty'\left(\frac{1}{\gamma_\infty}-\frac{1}{\gamma_0}\right). \tag{25}$$

The subscripts 0 and ∞ present values at zero pressure and infinite pressure, respectively. We have used the following identity at infinite pressure [28].

The most important reason for considering (16) at finite pressures is that it leads to the boundary conditions for higher-order Grüneisen parameters at infinite pressure which are identical to those derived in the

preceding section using the principle of calculus. Equation (16), when differentiated with respect to pressure, gives

$$\frac{q}{\gamma} = B\left(1 - K'\frac{P}{K}\right), \tag{26}$$

where q is the second-order Grüneisen parameter (3). Now, differentiating (20) with respect to P, we find

$$\frac{q\lambda}{\gamma} - \frac{q^2}{\gamma} = B\left[\left(KK''\right)\frac{P}{K} + K'\left(1 - \frac{K'P}{K}\right)\right], \tag{27}$$

where λ is the third-order Grüneisen parameter (8). (20) and (21) then yield

$$\lambda = \left(\frac{KK''}{1 - K'\dfrac{P}{K}}\right)\frac{P}{K} + K' + q\,. \tag{28}$$

The input data used in calculations are taken in Table 1, 2. The input data used in calculations are taken from and P, K_T and K'_T values from HOS EOS ((6)–(8)). Values of KK'' are determined from (22) of Stacey and Davis [25]. Values of γ, q and λ at different values of pressure are calculated from Eqs. (23), (26) and (28) respectively. The results have been given here in Fig. 7–12. Values of γ, q and λ for the Forsterite, Wadsleyite, Ringwoodite, Perovskite, Akimotoite and Postperovskite are compared with the corresponding values reported by Stacey EOS and recent developed HOS EOS. Stacey [20] found that K'_∞ is nearly equal to $\frac{3}{5}K'_0$. Calculated values of K'_∞ reported in Table 2 also vali-

TABLE 2. Values of input data for $MgSiO_3$–MgO System from equations.

Phase	K'_0	A	B	$K'_\infty = \frac{3}{5}K'_0$ [20 and 25]	$\gamma_\infty = \frac{1}{2}K'_\infty - \frac{1}{6}$ [25]
Forsterite	4.30	0.938	–0.123	2.58	1.123
Wadsleyite	4.14	0.843	0.213	2.48	1.075
Ringwoodite	3.98	0.826	0.280	2.38	1.027
Perovskite	4.38	0.588	0.745	2.62	1.147
Akimotoite	4.91	0.501	0.781	2.94	1.307
Postperovskite	4.03	0.598	0.872	2.41	1.042

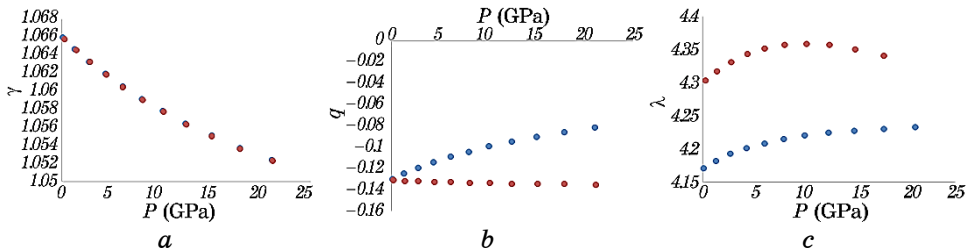

Fig. 7. First- (*a*), second- (*b*), third- (*c*) order Grüneisen parameter for Forsterite.

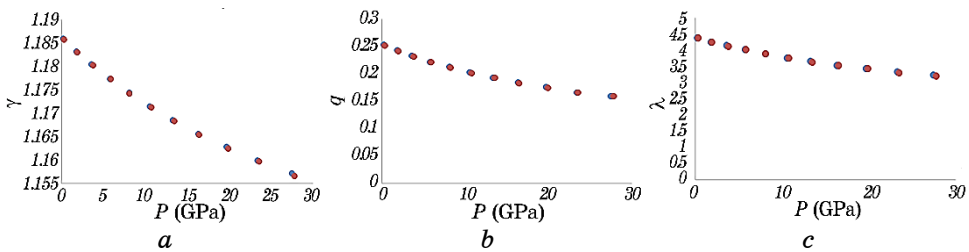

Fig. 8. First- (*a*), second- (*b*), third- (*c*) order Grüneisen parameter for Wadsleyite.

date the Stacey thermodynamic constraint [20, 25]: $K'_\infty > 1 + \gamma_\infty$.

Finally, we discuss that the higher-order thermoelastic properties obtained in the present study are useful to estimate the cross derivatives of bulk modulus with respect to pressure and temperature.

The results based on the Higher Order Shanker (HOS) EOS and the Stacey EOS are compared in Fig. 7, *a*–12, *c*. The difference in the two sets of values is substantial at low pressures. The results for the cross derivatives of bulk modulus with respect to P and T are very sensitive to the values of second- and third-order Grüneisen parameter q and appearing in Eq. (19). We have to calculate the higher-order Grüneisen parameters, taking the values P, K_T and K'_T from two sets: (i) HOS EOS, (ii) Stacey EOS. These are in good agreement with values obtained in the present study. The results obtained in the present study and those reported by Stacey EOS both reveal that values of γ, q and λ for the Forsterite, Wadsleyite, Ringwoodite, Perovskite, Akimotoite and Post-perovskite shown in Fig. 7, *a*–12, *c*. As pointed out that, the model is not satisfactory for Forsterite because of KK'' values become negative. At finite pressures our values of λ are between 2 and 4 for the lower mantle, and between 2 and 3 for the core. These values of λ are not much different from the Stacey–Davis values which are between 3 and 4 at finite pressures.

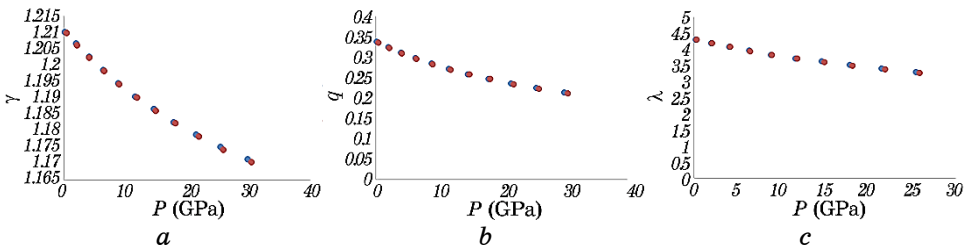

Fig.9. First- (*a*), second- (*b*), third- (*c*) order Grüneisen parameter for Ringwoodite.

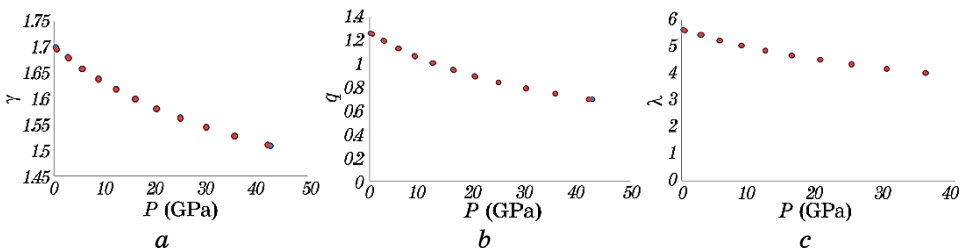

Fig. 10. First- (*a*), second- (*b*), third- (*c*) order Grüneisen parameter for Perovskite.

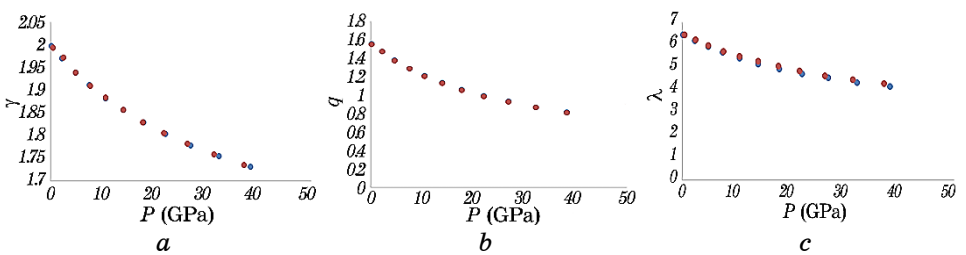

Fig. 11. First- (*a*), second- (*b*), third- (*c*) order Grüneisen parameter for Akimotoite.

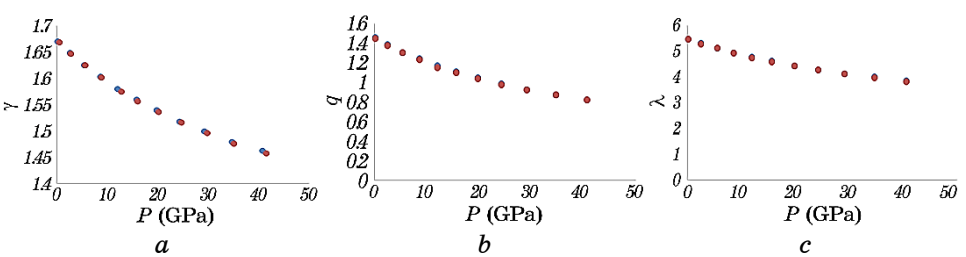

Fig. 12. First- (*a*), second- (*b*), third- (*c*) order Grüneisen parameter for Postperovskite.

Most of the calculations for the Earth interior were performed by Stacey and Davis (2004) using the reciprocal K-primed equation. λ_0 and λ_∞ were the exceptions. Subsequently, the method was developed (Shanker and Singh, 2005; Shanker *et al.*, 2009) for determining λ_0 and λ_∞ using the Stacey reciprocal K-primed equation. It should be mentioned that the expressions for KK'' and K^2K''' obtained from the Stacey reciprocal K-primed equation when using Shanker equation at infinite pressure (Shanker *et al.*, 2009) yield.

$$\lambda_\infty = \frac{K'^2}{K'_0}. \tag{29}$$

Equation (29) gives $\lambda_\infty = 1.54$, 1.48, 1.42, 1.56, 1.79 and 1.44 for Forsterite, Wadsleyite, Ringwoodite, Perovskite, Akimotoite and Postperovskite respectively (1.38 for the lower mantle, and 1.81 for the core). We note from (29) that $\lambda_\infty < K'_\infty$ since $K_\infty < K'_0$.

The results for the Forsterite, Wadsleyite, Ringwoodite, Perovskite, Akimotoite and Postperovskite given in figs are similar to those reported by Stacey EOS values. γ, q and λ all decrease with the increase in pressure. At infinite pressure, q_∞ and λ_∞ remain positive finite. It should be mentioned that (16) is more suitable for geophysical applications since P and K both are available directly from the seismological data.

An equation of state is physically acceptable only when it satisfies the thermodynamic constraints [5] *viz.* K'_∞ must be greater than 5/3, λ_∞ must be positive finite, and λ_∞ must be less than K'_∞. In case of the Birch–Murnaghan equation, we have $K'_\infty = 3$, and $\lambda_\infty = 2/3$ [8]. This equation thus satisfies the thermodynamic constraints, but yields the pressure-volume data [16], which deviate much from the seismological data [5]. For the Vinet–Rydberg equation [14], we have $K'_\infty = 2/3$, and $\lambda_\infty = 1/3$. Although this equation satisfies the constraint that $\lambda_\infty < K'_\infty$, but it fails to satisfy the fundamental constraint [5] $K'_\infty > 5/3$.

This equation thus violates the constraints *viz.* $K'_\infty > 5/3$ and $\lambda_\infty > 0$. To conclude, a physically acceptable equation of state must satisfy all the thermodynamic constraints as specified above, and it should be capable of predicting not only the pressure–volume relationship but also the higher derivative thermoelastic properties of materials in agreement with experimental data. The Stacey reciprocal K-primed equation is found to fulfil these requirements and HOS equations results close to Stacey EOS results.

In the limit of extreme compression $V \to 0$, P tends to infinity, K also tends to infinity, but their ratio P/K remains finite. K decreases with the increase in pressure and attains a minimum constant value K'_∞. This is because K becomes linear in P (directly proportional to P) in the limit of infinite pressure [2, 3]. Under this condition, the following identity has been found to hold [19, 20].

$$\left(\frac{P}{K}\right)_{\infty} = \frac{1}{K''_{\infty}}, \tag{30}$$

where the infinite subscript denotes the respective parameter at infinite pressure. (1) displays that the expression $\left[1 - K'P / K\right]$ reaches zero at extreme pressure and likewise exhibit the variation of α. The subsequent expression for $\alpha(P)$ can be written as [23, 24].

$$\alpha = \alpha_0 \left[1 - K'(P / K)\right]^t, \tag{31}$$

where α_0 is the thermal expansion at $P = 0$ and t is the constant dependent on material properties. The validity of (16) has been demonstrated for the Earth lower mantle [25] with $t = 1.13$. The Higher Order Shanker equation was used for obtaining thermal expansion and the corresponding input parameters [21] are also tabulated in Table 2. Values of $\alpha(P)$ with compressions are shown in Fig. 13. The values of thermal expansion obtained using modified EOS display strong correlation with the measured data [21, 22].

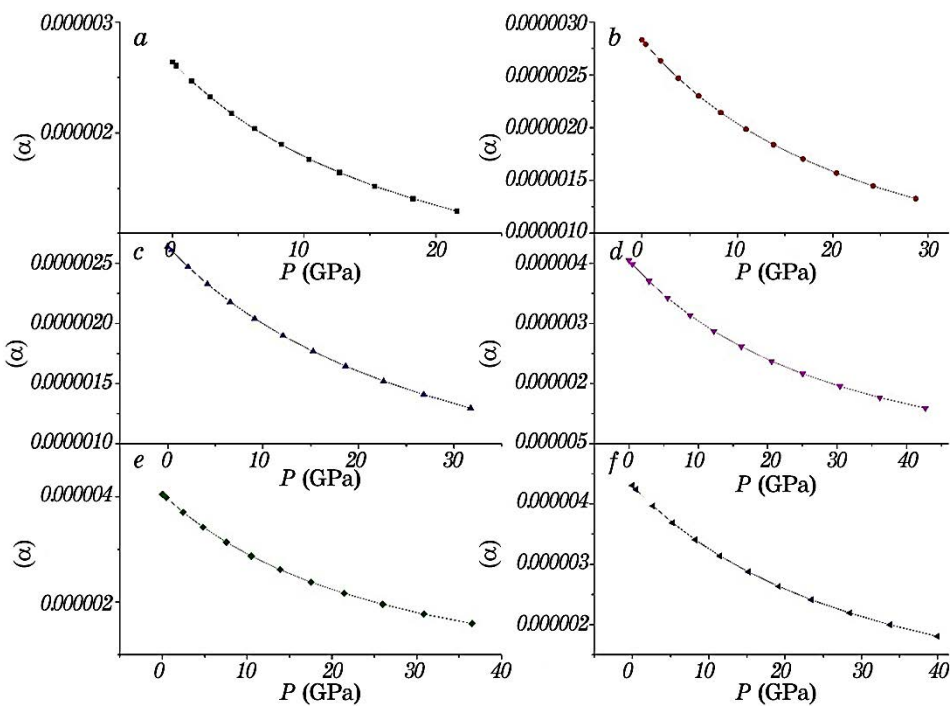

Fig. 13. Variation of thermal expansion (α) for Forsterite (*a*), Wadsleyite (*b*), Ringwoodite (*c*), Perovskite (*d*), Akimotoite (*e*) and Postperovskite (*f*) as a function of pressure MgO–$MgSiO_3$ system.

4. CONCLUSIONS

Shanker Equation of State (EOS) has been modified by including higher-order terms. The modified equation has been studied for fundamental MgO system, and, for validation, it is compared with phenomenological EOSs. The modified EOS for solids follows Stacey formulation under high compressions and is more reliable. The results obtained from modified EOS for $MgSiO_3$–MgO System are found to be in agreement with the experimental data. These results indicates that the correctness of the modified EOS and confirm that it can be used for determining thermoelastic properties of $MgSiO_3$ system at high pressure and high temperatures.

The equation's main feature is fewer input parameters are required, which are easily available by experimental studies. These equations may be frequently employed as the thermal equation of states of Earth's minerals. It uses various advanced quantum methods and simulations at the pressure and temperature of the Earth's interior. This study follows the basic laws of thermodynamic in regard to expressions at high-pressure. It also allows extrapolation to regions for which experimental data are not available.

As fewer studies have been done, so proposed study attempts to investigate the elastic properties of $MgSiO_3$ system under high pressure. The results for the Forsterite, Wadsleyite, Ringwoodite, Perovskite, Akimotoite and Postperovskite, given in Figs. are similar to those reported by Stacey and Davis [25]. As pointed out by Stacey and Davis (2004), the same formula for an equation of state works satisfactorily for different phases provided we use appropriate values of input parameters such as K_0' and K_∞' which are different for the lower mantle, outer core and the inner core of the Earth.

The present HOS EOS results are similar to Stacey EOS (6) proves particularly advantageous for geophysical applications, as both P (pressure) and K (isothermal bulk modulus) can be directly obtained from seismological data. The applicability of the Higher Order Shanker Equation of State (HOS EOS) extends beyond geophysics, demonstrating its relevance in the study of Bulk Metallic Glasses [29]. Moreover, the HOS EOS can be reliably extrapolated to high r pressures, enhancing its utility for interpreting recent experiments in high-pressure research.

The ability to apply the same methodology to both complex minerals and BMGs underscores its robustness and utility in diverse scientific investigations, making it a valuable tool for researchers exploring a range of materials and their behaviours.

Therefore, the new EOS can contribute to the planning of high-pressure experiments in the future on compression behaviour of Earth-forming minerals and solids.

REFERENCES

1. O. L. Anderson, *Equations of State of Solids for Geophysics and Ceramic Science* (New York: NY: 1995; online edn, Oxford Academic: 2023).
2. F. D. Stacey, B. J. Brennan, and R. D. Irvine, *Geophysical Surveys*, **4**, No. 3: 189 (1981).
3. F. D. Stacey, *Rep. Prog. Phys.*, **73**, No. 4: 046801 (2010).
4. A. Keane, *Aust. J. Phys.*, **7**, No. 2: 322 (1954).
5. F. D. Murnaghan, *Proc. Natl. Acad. Sci.*, **30**, No. 9: 244 (1944).
6. J. Shanker, K. Sunil, and B. S. Sharma, *Phys. Earth Planet. Inter.*, **262**: 41 (2017).
7. S. S. Kushwah and J. Shanker, *Phys. B*, **253**, Nos. 1–2: 90 (1998).
8. F. D. Stacey, *Phys. Earth Planet. Inter.*, **89**, Nos. 3–4: 219 (1995).
9. S. Gaurav, S. Shankar, A. Raghav, P. Kumari, and M. Singh, *Russ. J. Earth Sci.*, **22**: 2 (2022).
10. P. Vinet, J. Ferrante, J. H. Rose, and J. R. Smith, *J. Geophys. Res.: Solid Earth*, **92**, No. B9: 9319 (1987).
11. S. Gaurav, B. S. Sharma, S. B. Sharma, and S. C. Upadhyaya, *Phys. B*, **322**, No. 3: 328 (2002).
12. R. Rydberg, *Zeitschrift für Physik*, **73**: 376 (2013).
13. J. Shanker, B. Singh, and S. S. Kushwah, *Phys. B*, **229**, Nos. 3–4: 419 (1997).
14. M. Born and K. Huang, *Am. J. Phys.*, **23**, No. 7: **474** (2005).
15. J. Hama and K. Suito, *J. Phys.: Condens. Matter*, **8**, No. 1: 67, (1996).
16. J. Shanker, S. S. Kushwah, and M. P. Sharma, *Phys. B*, **271**, Nos. 1–4: 158 (1999).
17. J. Shanker, B. P. Singh, and K. Jitendra, *Condens. Matter. Phys.*, **11**, No. 4: 681 (2008).
18. S. Rekha, K. Sunil and B. S. Sharma, *High Temperatures – High Pressures*, **46**, Iss. 6: 449 (2017).
19. F. D. Stacey, *J. Phys.: Condens. Matter*, **11**, No. 2: 575 (1999).
20. F. D. Stacey, *Geophys. J. Int.*, **143**, No. 3: 621 (2000).
21. T. S. Sokolova, P. I. Dorogokupets, K. D. Litasov, B. S. Danilov, and A. M. Dymshits, *High Pressure Res.*, **38**, No. 3: 193 (2018).
22. P. I. Dorogokupets, A. M. Dymshits, K. D. Litasov, and T. S. Sokolova, *Sci. Rep.*, **7**: 1 (2017).
23. K. Sunil, P. K. Singh, and B. S. Sharma, *Mod. Phys. Lett. B*, **26**, No. 22: (2012).
24. J. Shanker, K. Sunil, and B. S. Sharma, *Phys. B*, **407**, No. 12: 2082 (2012).
25. F. D. Stacey and P. M. Davis, *Phys. Earth Planet. Inter.*, **142**, Nos. 3–4: 137 (2004).
26. F. D. Stacey, *Rep. Prog. Phys.*, **68**: 341 (2005).
27. J. Shanker, K. Sunil, and B. S. Sharma, *Phys. Earth Planet. Inter.*, **262**: 41 (2016).
28. L. Knopoff, *J. Geophys. Res.*, **68**: 2929 (1963).
29. S. Gaurav, S. Shankar, Arvind Mishra, and S. P. Singh, *Metallofiz. Noveishie Tekhnol.*, **45**, No. 10: 1151 (2023).

Metallophysics and Advanced Technologies
Металофіз. новітні технол.
Metallofiz. Noveishie Tekhnol.
2025, vol. 47, No. 6, pp. 619–625
https://doi.org/10.15407/mfint.47.06.0619
Reprints available directly from the publisher

PACS numbers: 06.60.Vz, 68.08.Bc, 68.08.De, 68.35.Np, 81.05.Je, 81.20.Vj, 85.40.Ls

Brazing and Metallization of Zirconia Ceramics with Ni–Cr–Ti Filler to Fabricate Products Operating at High Temperatures

O. V. Durov and T. V. Stetsyuk

I. M. Frantsevych Institute for Problems of Materials Science, N.A.S. of Ukraine,
3 Omeljan Pritsak Str.,
UA-03142 Kyiv, Ukraine

Ni–Cr–Ti system is considered as filler for ZrO_2-ceramics brazing and metallization because of its high melting temperature. The contact angle near 40° is reached for (Ni–56Cr)–15Ti composition; the adhesion is provided by the formation of an oxidized titanium transition layer on the interface. A method of spreading the nickel–chromium melt on titanium plate is elaborated for metallization and brazing. A mix of metal powders and an infiltration of nickel–chromium melt through titanium powder on ceramics surface or in brazing gap are also used. The method of spreading shows the better results because high-disperse titanium oxidizes with oxygen from zirconia.

Key words: brazing, metallization, zirconia, wetting, infiltration, spreading.

Систему Ni–Cr–Ti було розглянуто як прилюток для лютування та металізації ZrO_2-кераміки, зважаючи на її високу температуру топлення. Для композиції (Ni–56Cr)–15Ti досягнуто крайовий кут близько 40°; адгезія забезпечується утворенням перехідного шару окисненого титану на межі поділу. Розроблено спосіб металізації та лютування розтіканням нікель-хромового розтопу по титановій пластині. Також використано суміш металевих порошків і просочування нікель-хромового розтопу через титановий порошок на поверхні кераміки або в лютівному зазорі. Метод розтікання показав ліпші результати, оскільки високодисперсний титан окиснюється Оксиґеном з діоксиду Цирконію.

Corresponding author: Oleksii Viktorovich Durov
E-mail: avdu@ukr.net

Citation: O. V. Durov and T. V. Stetsyuk, Brazing and Metallization of Zirconia Ceramics with Ni–Cr–Ti Filler to Fabricate Products Operating at High Temperatures, *Metallofiz. Noveishie Tekhnol.*, **47**, No. 6: 619–625 (2025). DOI: 10.15407/mfint.47.06.0619

Ключові слова: лютування, металізація, діоксид Цирконію, змочування, просочування, розтікання.

(Received 30 October, 2024; in final version, 15 November, 2024)

1. INTRODUCTION

At the moment, the methods of brazing of ceramic materials, including zirconia based, have been developed, which provide quite high characteristics of brazed joints [1, 2]. Titanium is used as an adhesive-active component of such solders. The disadvantage of these technologies is a relatively low melting point of fillers. The operating temperatures of such joints do not exceed 600–700°C. However, currently there is an increasing need to produce solder joints operating in extreme conditions with operating temperatures of 900–1000°C, while parts containing these joints are required in many high-temperature use (turbines, internal combustion engines, electron beam equipment, fuel cells, electrolysers, *etc.*). Therefore, it is important to develop methods for obtaining ceramics compounds with high operation temperature. Basically, such technologies are developed for oxygen-free ceramic materials [3–7]. Zirconium is by a solder in many applications, but is little used for oxide ceramic materials. Therefore, it is important to test high-temperature active metal melts as fillers for ZrO_2-ceramics brazing or metallization.

2. MATERIALS AND METHODS

Dense ceramics based on zirconia, partially stabilized 3.5 at.% of yttria, high purity nickel, chromium (not lower than 99.997%), iodide titanium, high-pure powders of nickel, chromium, and titanium were used in the experiments. The composition of nickel–chromium (54 at.% Cr) alloy corresponding to eutectic one [8], with the melting point of 1618 K, was chosen as a solvent of active metal, to which various amounts of titanium were added. This composition has relatively low melting temperature and high enough concentration of chromium providing the heat resistance. This alloy was prepared by remelting appropriate amounts of components in vacuum in alumina crucibles. For brazing experiments, titanium foil 0.2 mm thick was also used.

Surfaces of ceramic samples for wetting experiments were polished with a diamond paste of 0.7–0.3 μm. In the brazing operations, ceramic disks of 10-mm diameter were joined to disks of 15-mm diameter.

Wetting was studied by the sessile drop method at 1350°C. The experiments were performed in vacuum no worse than 10^{-3} Pa; images of the drops were obtained using a high-resolution digital camera.

Three methods for metallization or brazing were used.

For the first method, a mix of chromium, nickel and titanium powders was prepared and was painted on the surface of the ceramic for metallization or in the brazing gap. Then, samples were dried and annealed in vacuum.

For the second technique, titanium powder was applied to the surface of the ceramic disk or in the brazing gap between the joined discs. After drying, the samples were weighed, and a piece of Ni–54Cr alloy was situated on the layer of Ti powder; samples were annealed in vacuum. Titanium powder is easily impregnated with metal melts, then, dissolves in them and acts as an active addition that provides metal adhesion to solid oxide.

According to the third technique, on the surface of ZrO_2-ceramics or between the brazed details, a titanium plate of 0.2-mm thickness was situated, on it placed a piece of Ni–54Cr alloy; the samples were annealed in vacuum. After melting, the nickel–chrome-liquid filler spreads on the titanium plate, covering the surface intended for metallization or penetrating into the brazing gap, and dissolves the titanium, thus, formed a melt with high adhesion to ZrO_2.

3. RESULTS AND DISCUSSION

The results of experiments on wetting of the ZrO_2-ceramics by Ni–Cr–Ti melts are presented on Fig. 1 as the dependence of the contact angle on the atomic concentration of titanium in melt.

The addition of titanium improves significantly wetting of ceramics; at 15% of titanium, the contact angle is of about 40°. This is enough for brazing [9]. In addition, it needs to note that the equilibrium contact angles were reached during not more than 5 min; it is fast

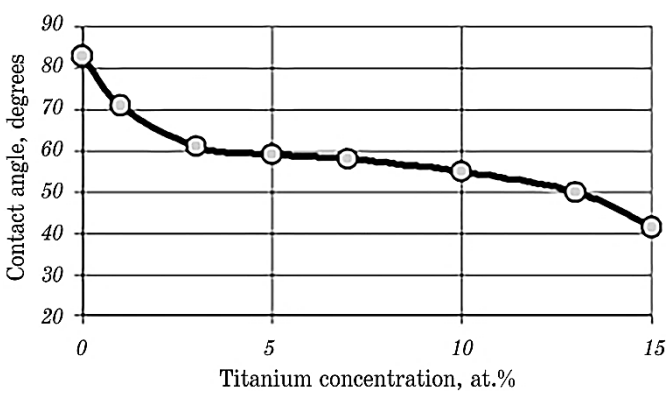

Fig. 1. The dependence of contact angle on titanium concentration in Ni–54Cr melt for wetting of ZrO_2-ceramics.

enough. The darkening of ceramics was observed, apparently due to the loss of oxygen with the formation of a non-stoichiometric phase, which is characteristic for contact of zirconia and metal melts containing titanium [10]. Unlike [10], where dark areas with a strict boundary were formed in the volume of ceramics, in these experiments, ceramic samples darkened within all volume. Since the spread of the dark area is a diffusion process [10], its acceleration in these experiments is explained by the increase in temperature that intensifies diffusion.

From the sample, where the drop of the (Ni–54Cr)–10Ti melt solidified on the ceramic surface, the cross-section was fabricated; the microphotography of the ceramics–-metal interface after etching with nitric acid is represented in Fig. 2.

The alloy of the solidified drop has a eutectic structure (dark areas correspond to a phase rich in nickel) consisting of a matrix enriched with nickel, where grains of a phase enriched with chromium are distributed. There are no noticeable differences in the distribution of nickel or chromium near interface and in the depths of the drop. A thin transition layer presents in the interface; probably, it consists of oxidized titanium, providing adhesion of the metal to the solid oxide, as in other systems [9]. The thickness of the layer is uneven; obviously, it has an island structure.

Since sufficient wetting was reached and the adhesion of the drop to the substrates was high, the (Ni–56Cr)–15Ti composition was tested as filler for brazing and metallization of the ZrO_2-ceramics by the methods described above. The temperature was of 1350°C; holding time—5 min. Photographs of some samples are represented in Fig. 3.

In all metallization methods, satisfactory results were obtained: the metal layer was kept on the surface of the ceramics firmly enough. When using the method of the nickel–chrome on the titanium plate

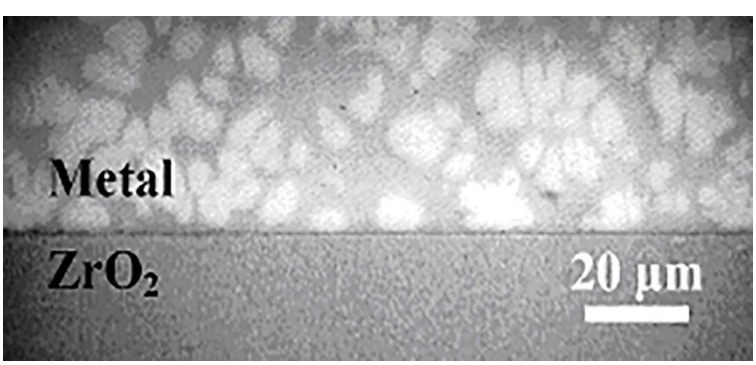

Fig. 2. Microphotography of the ceramics–metal interface for the (Ni–54Cr)–10Ti drop solidified on the surface of ZrO_2-ceramics after the etching.

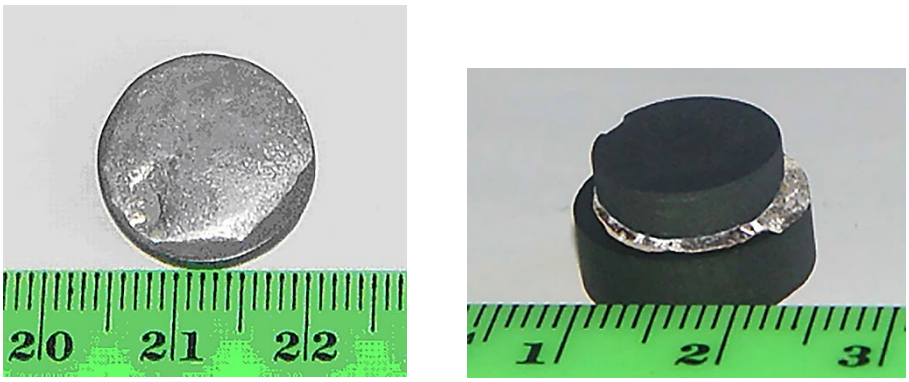

a *b*

Fig. 3. Samples of ZrO_2-ceramics metallized (*a*) and brazed (*b*) by nickel–chromium melt spreading on titanium plate.

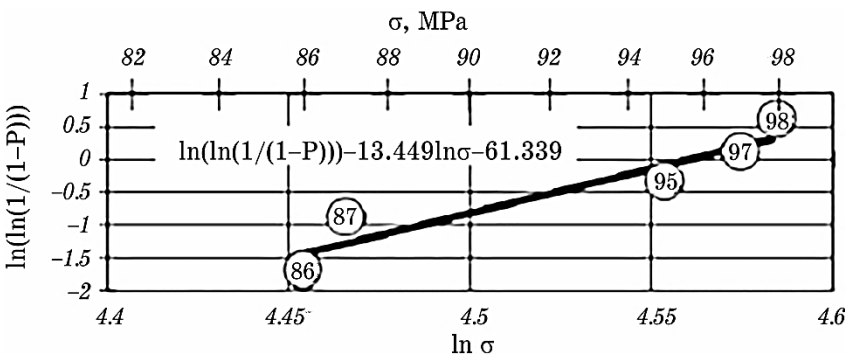

Fig. 4. The Weibull plot for shear strength of ZrO_2-ceramics to itself joints brazed by spreading of nickel–chromium melt on titanium plate.

spreading, the metal surface was the cleanest and homogeneous (Fig. 3, *a*); for methods using a mixture of powders and the infiltration of the nickel–chromium melt through the layer of titanium powder, signs of coating oxidation are noticeable.

The shear strength of the joints brazed using the mixture of powders or infiltration was no more than 40 MPa. However, the strength of the joints obtained by spreading of the solder on the titanium plate was of 86–98 MPa; the Weibull plot for these strength values is presented in Fig. 4.

Low strength for the method using a mixture of powders can be explained by the presence of contaminations adsorbed from air in the powders. In the case of infiltration, annealed titanium powder was used, so the influence of contamination is excluded.

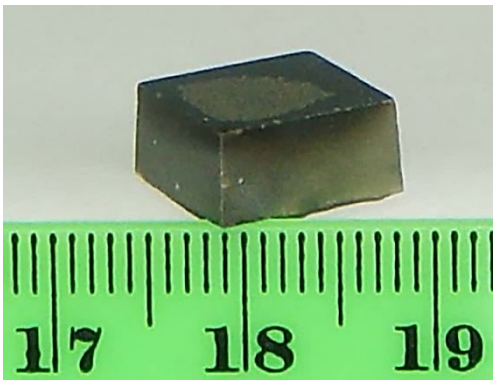

Fig. 5. Darkening of ZrO_2-ceramics with applied Ti powder on its surface after annealing in vacuum; 1350°C; 15 min.

Therefore, the following explanation can be suggested: the high-pure high-active titanium powder is in a closed contact with ceramics, and the mobility of anions in the structure of zirconia at brazing or metallization temperature is also sufficient [11], so, oxygen from ZrO_2 interacts with the titanium powder oxidizing it. As result, the quality of metal coatings and brazing joints degrades. To check this assumption, a sample of ceramics with titanium powder applied to its surface was annealed in vacuum at 1350°C 15 min. The ceramic has darkened and more intensively near the covered with titanium surface (Fig. 5). Therefore, titanium powder on the surface of the zirconia can indeed be oxidized by oxygen from the substrate at the experimental temperatures.

4. CONCLUSION

The Ni–Cr–Ti system may be used for metallization and brazing of ZrO_2-ceramics. The method of spreading of nickel–chromium melt on titanium plate was elaborated and shown the better results in comparison to methods with using of powders, because high-disperse titanium oxidizes by oxygen from zirconia.

The results obtained open up the possibility of producing brazed and metallized products for high-temperature applications.

REFERENCES

1. Y. V. Naidich, V. S. Zhuravlev, I. I. Gab, B. D. Kostyuk, V. P. Krasovskyy, A. A. Adamovskyy, and N. Yu. Taranets, *J. Europ. Ceram. Soc.*, **28**: 717 (2008).
2. S. Mishra, A. Sharma, D. H. Jung, and J. P. Jung, *Met. Mater. Int.*, **26**: 1087 (2020).
3. Y. Zhang, D. Feng, Z.-Y. He, and X.-C. Chen, *J. Iron Steel Res. Int.*, **13**: 1 (2006).

4. H.-P. Xiong, W. Dong, B. Chen, Y.-S. Kang, A. Kawasaki, H. Okamura, and R. Watanabe, *Mater. Sci. and Eng.: A*, **474**, Iss. 1–2: 376 (2008).
5. A. Koltsov, F. Hodaj, and N. Eustathopoulos, *Mater. Sci. and Eng.: A*, **495**, Iss. 1–2: 259 (2008).
6. H.-P. Xiong, W. Mao, Y.-H. Xie, W.-L. Guo, X.-H. Li, and Y.-Y. Cheng, *Mater. Let.*, **61**, Iss. 25: 4662 (2007).
7. V. P. Krasovskyy and A. E. Shapiro, *J. Superhard Materials*, **45**, No. 2: 93 (2023).
8. *Collection of Phase Diagrams* [Electronic resource]: http://www.crct.polymtl.ca/fact/documentation/FSstel/Cr-Ni.jpg
9. Ju. V. Naidich, *Prog. Surf. Membrane Sci.*, **14**: 353 (1981).
10. A. V. Durov, Y. V. Naidich, and B. D. Kostyuk, *J. Mater. Sci.*, **40**: 2173 (2005).
11. Y. N. Vilk, V. E. Shvaiko-Shvaikovskii, and V. A. Shvarts, *Refractories*, **36**: 247 (1995).

Metallophysics and Advanced Technologies
Металофіз. новітні технол.
Metallofiz. Noveishie Tekhnol.
2025, vol. 47, No. 6, pp. 627–645
https://doi.org/10.15407/mfint.47.06.0627
Reprints available directly from the publisher

PACS numbers: 06.60.Vz, 52.77.Fv, 61.72.Ff, 62.20.Qp, 81.20.Vj, 81.40.Cd, 81.40.Ef

Structure and Mechanical Properties of Heat-Treated D16 Aluminium-Alloy Welded Joints Made with a Consumable Electrode after Heat Treatment

T. M. Labur and V. A. Koval

E. O. Paton Electric Welding Institute, N.A.S. of Ukraine,
11 Kazymyr Malevych Str.,
UA-03150 Kyiv, Ukraine

The extent of the influence of heat treatment on structural features and mechanical properties of 6-mm D16 alloy and its welded joints made by a consumable electrode with application of two isolated filler wires or embedded elements of different chemical composition is established. Wires of Zv1201, ZvAK5, ZvAK12 grades of 1.6-mm diameter and embedded elements cut out of V92, V96 and 7056 alloys are used for welding.

Key words: aluminium alloy, consumable-electrode welding, joining, heat treatment, microstructure, mechanical properties.

Встановлено ступінь впливу термічного оброблення на структурні особливості та механічні властивості стопу Д16 товщиною у 6 мм та його зварних з'єднань, виконаних топкою електродою із застосуванням двох ізольованих присадних дротів або втілених елементів різного хемічного складу. Для зварювання використано дріт марок Зв1201, ЗвАК5, ЗвАК12 діяметром у 1,6 мм і втілені елементи, яких було вирізано зі стопів В92, В96 і 7056.

Ключові слова: алюмінійовий стоп, зварювання топкою електродою, з'єднання, термооброблення, мікроструктура, механічні властивості.

Corresponding author: Tetiana Mykhailivna Labur
E-mail: tanyalabur@gmail.ua

Citation: T. M. Labur and V. A. Koval, Structure and Mechanical Properties of Heat-Treated D16 Aluminium-Alloy Welded Joints Made with a Consumable Electrode after Heat Treatment, *Metallofiz. Noveishie Tekhnol.*, **47**, No. 6: 627–645 (2025). DOI: 10.15407/mfint.47.06.0627

(Received 4 May, 2023; in final version, 11 January, 2024)

1. INTRODUCTION

Heat-hardenable D16 aluminium alloy (Al–Cu–Mg) is used with success in different mechanical engineering sectors, as it is characterized by a unique combination of mechanical properties, due to chemical composition of chemical elements (Table 1). The range of its semi-finished products is rather wide [1–5]. The main precipitation phases are $CuAl_2(\theta)$ and $Al_2CuMg(S)$. At the ratio of $Cu/Mg \leq 2.6$, the structure contains *S*-phase, which is the main phase in D16 alloy strengthening. At the ratio of $Mg/Si = 1.73$, Mg_2Si phase forms in addition to it.

In the cast state, the alloy structure is non-equilibrium. It consists of the solid solution and precipitates of intermetallic phases, located along the grain boundaries and between the dendrite axes in the form of pseudoeutectic. This one results in a low strength level (185–200 MPa) of the alloy, as well as low ductility, compared to other structural aluminium alloys (Table 2). At process heating, the alloy demonstrates a high capability of structural equilibrium due to the influence of the mechanism of all the alloying element transition from the equilibrium state into the solid solution [1, 4, 6, 7]. Therefore, the alloy chemical composition was selected taking this physical phenomenon into account. In the wrought state, this effect develops faster than in the cast one. During decomposition of oversaturated solid solution, the strength is increased, but the ductility values are decreased. In the thermally strengthened condition, the alloy is characterized by somewhat higher strength (210–230 MPa), depending on temperature–time heat treatment modes. In the annealed state, the value of D16 alloy ductility is satisfactory—3–6%.

To prevent cracking in the metal and lower the degree of its buckling, the alloy is quenched from the temperature of 500 ± 5°C in cold water of 20–40°C. In the case, when the alloy stays at room temperature for 90–100 h, it demonstrates the capability for natural (zonal) ageing [6]. Ultimate tensile strength of the alloy after quenching is increased by 110 MPa, compared to the annealed state. An increase in ultimate tensile strength by 100 MPa is observed in this case. The level

TABLE 1. Chemical composition and mechanical properties of 6-mm D16 alloy.

Mg	Cu	Mn	Si	Fe	Zn	*E*, GPa	σ_t	$\sigma_{0.2}$	$\sigma_{0.01}$	δ_5, %
							MPa			
1.4–1.7	4.0–4.5	0.34–0.53	0.16–0.19	0.21–0.22	0.07–0.11	67–71	217–221	106–115	79–89	6–18

TABLE 2. Effect of heat-treatment on hardness of D16 alloy welded joints, made by consumable electrode with batch-produced Zv1201 filler wire and Si-containing wire.

State of base metal and welded joint	Hardness, *HRB*									
	BM	Zv1201			Zv1201 + ZvAK5			Zv1201 + ZvAK12		
		Weld	WJ	HAZ	Weld	WJ	HAZ	Weld	WJ	HAZ
After welding and natural ageing	65–67	88–89	60–89	59–65	89–90	62–87	60–65	89–90	62–87	59–65
Welding + artificial ageing		88–88	79–87	63–66	95–96	74–90	60–65	96–98	78–94	61–66
Welding + quenching + artificial ageing	100–102	94–95	97–98	96–99	94–95	97–98	99–101	93–95	95–98	99–101

of mechanical properties of the alloy after quenching and natural ageing reaches $\sigma_t = 470$ MPa, $\sigma_{0.2} = 300$ MPa, $\delta = 19\%$. Wrought sheets are often subjected to artificial (phase) ageing at temperature conditions of $190 \pm 5°C$ for 12–13 h [4–6].

At the same time, the main disadvantage of the alloy remains to be its sensitivity to process heating. It is exactly what provokes initiation of 'hot cracks', as a result of a non-uniform distribution of alloying elements in the alloy structure, as well as formation of complex phase compounds, *etc.*, the appearance of which lowers the mechanical properties of base metal and its welded joints. That is why, technologies aimed at cracking prevention and raising the level of its respective characteristics are applied in fabrication of critical structures from this alloy. Different technological approaches are used for this purpose: from application of advanced solid-phase welding technologies to manufacture of integral welded structures [5].

Note that the technological advance in welded structure fabrication is directly associated with solving a number of complex, but interrelated science and technology problems. Development of new more functional structural materials, as well as improvement of the chemical composition and properties of the traditional alloys result in the demand and need for a thorough study of their joining processes. At the same time, arc-welding technologies remain the most common methods of joining parts and components in structure fabrication [4]. This is promoted by flexibility of processes realization, their cost, as well as the availability and degree of acceptance by industry of the normative documents, required for reproduction of the respective welding modes under the shop conditions. The main requirements here

are stability of the weld structure quality and higher efficiency of production lines for welded structure fabrication.

Considering the technological advantages of arc technologies, it should be noted that the low speeds of tungsten electrode welding of aluminium alloys from the viewpoint of industrial requirements, restrain production of sound welds. Plasma-arc welding is too expensive now, and it does not ensure the appropriate production flexibility of the process under the conditions of its plant realization, unlike the consumable electrode joining technology [7]. This is due to a relatively low value of heat input into the process proper that allows it to be automated and integrated into the production line. However, there remain the consequences of the impact of physical conditions of liquid metal solidification in the weld pool, during which such undesirable phenomena as segregation and formation of various technological defects may arise, lowering the joint properties.

Chemical composition of filler wires is one of the main tools for weld structure improvement and producing the required mechanical and service characteristics of the joints in welded structures. Note that the effectiveness of their influence on the mechanical properties is diverse, as it depends on the alloying degree of the wires proper [1–4]. Two or three filler wires (electrodes) are sometimes used for improvement of the production process of structure welding. It allows modifying the weld structure, and, this way, eliminating the causes for defect formation in the deposited metal. A similar effect was also obtained in multipass welding with rotation. In this case, the change of deformation and stress concentration along the weld axis allowed increasing the joint strength level by 10% and the relative elongation level by 4% [7, 8].

Recovery of the properties of heat-hardenable aluminium alloys and their joints is often observed, when various heat treatment modes are used [9–11]. It is achieved due to realization of two mechanisms of aluminium-alloy strength improvement: formation of precipitate dispersion or solid solution strengthening and alloy quenching; alloying element dissolution in the solid solution and their further precipitation in the form of submicroscopic coherent particles [1, 2]. The operation of artificial ageing, denoted as T81, is the most common in production, as it increases the strength level. Such an increase in strength is also observed at its combination with subsequent deformation of metal up to 8% (T37 condition), which is performed at 163°C for 24 (36) h. However, the ductility values decrease almost two times with both the technologies. A simultaneous increase of strength and ductility characteristics is reported as a result of performance of a full heat-treatment cycle (T62 condition). In this case, first, the metal is quenched in water with cooling from the temperature of 500 ± 5°C, and then, the operation of artificial (phase) ageing is performed for 12 h at

the temperature of 190 ± 5°C [12, 13]. As the cooling rate during quenching determines the structure morphology and residual stress level, *i.e.*, it has an essential influence on the mechanism of formation of coarse nonequilibrium phases, it is given special attention [5]. Elimination of some phases or their additional precipitation in the structure promotes partial or complete recovery of the mechanical properties, so that, it is rational to conduct a more detailed study of the effectiveness of heat treatment modes of D16 alloy joints made by a consumable electrode with two isolated wires.

In connection with the above ideas, the objective of the study was to establish the features of microstructure formation in D16 alloy welds made by a consumable electrode with application of batch-produced filler wires or embedded elements after heat treatment by different technologies, and to compare these results with base metal properties. Batch-produced wires of Al–Si system were selected for this purpose, namely, ZvAK5 (Al–5.5% Si) and ZvAK12 (Al–12% Si) with silicon. Its presence promotes appearance of a considerable number of low-melting eutectics capable of lowering the risks of solidification crack and pore formation in welding of D16 alloy or ensuring the conditions for their healing during weld solidification. The following zinc-containing alloys were used as embedded elements: V92 (Al–0.5% Cu–4.2% Mg–3.5% Zn), V96 (Al–2.3% Cu–2.6% Mg–8.5% Zn) and 7056 (Al–1.65% Cu–1.8% Mg–9.5% Zn). Butt joints were welded by the following technology variants: Zv1201 + ZvAK5; Zv1201 + ZvAK12; Zv1201 + V92; Zv1201 + V96; Zv1201 + 7056. Research results were compared with those of the joints produced with one wire of Al–Cu system of Zv1201 grade (Al–6.3% Cu–0.3% Mn). Proceeding from analysis of the features of the structure and mechanical properties of the specimens, cut out in different sections of the welds, an optimal combination of filler wire chemical composition was determined, application of which enables producing permanent joints of D16 alloy, in keeping with the requirements to and purpose of the welded structure. The above methodology was selected in connection with the fact that phase growth occurs during liquid metal solidification and formation of weld microstructure on its boundary along the front [1]. The extent of this phenomenon is determined by temperature gradient on the interface of the solid solution and the phases, as well as the pattern of distribution of the solution, the morphology of which changes from the cellular to the dendritic one.

The operation of artificial ageing by the mode of $T = 190 \pm 5$°C for 12 h was selected to determine the range of effectiveness of the above-mentioned heat treatments, as it ensures the maximum strength level and stability of the structure in time [2–4]. Another studied technology variant was application of a full heat treatment cycle, *i.e.*, quenching of D16 alloy welded joints (welded butt joint heating up to the tem-

perature of $T = 500 \pm 5$°C and soaking for 1 h with cooling in water and further artificial ageing by the mode of $T = 190 \pm 5$°C for 12 h). Selection of the above technological conditions of welded joint treatment was performed, taking into account the known data [1, 4, 5], which show that at D16 alloy quenching the brittle intermetallic interlayers between the grains almost completely go into the solid solution, and, thus, they can ensure a higher level of joint ductility. The driving force of this process is determined by the degree of solid solution oversaturation in the alloy, features of its structural morphology, dimensions or dispersion of phase inclusions, precipitating during heat treatment.

2. EXPERIMENTAL PROCEDURE

Before welding, D16 alloy blanks were traditionally treated in 10%-NaOH solution and clarified in 13%-HNO_3 solution. Consumable-electrode welding of the blanks was conducted in a horizontal position. For practical realization of the process, technological equipment was improved, which ensured simultaneous mechanical feeding of two insulated wires into a common pool. The wires were fed into the pool according to standard requirements, *i.e.*, directly from the face surface of the butt joints being welded. Modes of the joining process and conditions of wire feed synchronization directly during welding were also optimized.

To expand the technology variants, embedded elements of 2×2×2.5-mm size of V92, V96 and 7056 aluminium alloys with different zinc content were also used, which were located in the lower part of the butt. Zn, Mg, Cu, Mn and Zr chemical elements, which are included into the composition of these alloys, ensure physic-chemical conditions for formation of a fine-grained structure of weld metal, which promotes its strengthening under the conditions of subsequent heat treatment of welded joints [1].

The value of welding heat input was selected from the condition of a minimal value required for complete penetration of this alloy thickness, that is why the process of butt joining was conducted in the following mode: $I_w = 240$–250 A, $U_a = 20$–21 V, welding speed here was equal to 31–33 m/h. The width of butt welds was almost the same from the face and penetration side, being in the range of 9–11 mm. The process was realized with application of a forming backing, as it is known that when it is used growth of columnar crystallites in the two-dimensional direction takes place, and it influences the joint quality [4]. Modulation of the main mode parameters with cycle duration period of $2.2 + 0.2$ s created necessary thermophysical conditions, when control of the process of drop transfer from the main wire of Zv1201 grade and formation of the appropriate shape of the weld pool and weld

structure are improved. It increases the amount of oversaturated solid solution and the density of precipitates of dispersed particles of the strengthening phase during solid solution decomposition.

The quality of D16 alloy weld formation was assessed visually and by x-ray method (GOST 7512 [13]) in RAP-150/300 X-ray unit. Weld metal density was controlled in Densitometer DP-30 instrument.

The welded butt joints were used to prepare specimens for mechanical testing, in keeping with the requirements of normative document GOST 6996 [14]. Mechanical tests were conducted by a procedure, described in GOST 1497 [15]. Here, Instron-1126 machine was used, the speed of its crossbeam displacement being 6 mm/min. The load and deformation values at specimen testing were recorded by a personal computer that allowed further on calculating the values of ultimate tensile strength (ultimate strength of welded joints (σ_t^{WJ}) and weld metal (σ_t^{WM}) of welded joints). Obtained experimental results allowed establishing their sensitivity to the thermal cycle of consumable electrode welding and assessing the coefficient of welded joint strength, compared to base metal strength level ($K_W = \sigma_t^{ws}/\sigma_t^{bM}$ or $K_W = \sigma_t^{WM}/\sigma_t^{bM}$).

After welding and heat treatment by two modes, the general state of the joints and their deformability under the conditions of three-point bending with load application from the weld root side as bend angle (α) (GOST 14019-80) were studied, and the derived results were compared with base metal values. Technological reinforcement and weld root here were machined to required dimensions.

Heat treatment of the specimens before tensile testing was performed in keeping with the above technology variants: artificial ageing and full heat treatment (quenching and artificial ageing). Selection of the mode of joint heat treatment was performed, taking into account the processes of dispersed precipitation of phase particles, solid solution strengthening, brittle intermetallic dissolution that promotes higher ductility of D16 alloy [1]. Precipitation of dispersed particles of $AlCu_2$ phase was observed at artificial ageing, their presence in the metal increasing this alloy strength. The effectiveness of the above processes was determined during investigations, with recording of the structural morphology and size of phase inclusions in different zones of welded joints.

Brinell hardness *HB* was evaluated with the purpose of a better substantiation of selection and development of the respective technological measures on optimization of the modes of D16 alloy welding and heat treatment of its welded joints. The degree of strength lowering was recorded in Rockwell instrument at load $P = 600$ N, by a 1/16 inch sphere (measurement point spacing was 2 mm). All the obtained hardness values were specified by normative document GOST 9012-89 [16]. Hardness measurements were conducted on the surface of the studied welded butt joints, cut out across the welding direction. Determination

of the above parameter was based on the existence of a connection between the structural state and mechanical properties [1, 2].

Metallographic examination of base metal and welded joints was performed in MMT-1600V microscope, using butt joint sections cut out across the rolling direction of the semi-finished products. Microstructural features were revealed by electrolytic polishing in a solution of the following composition: chloric acid 1000 cm^3 + ice acetic acid 75 cm^3.

3. INVESTIGATION RESULTS AND DISCUSSION

Dissolution of alloying elements in the aluminium solid solution and formation of submicron particles of the second phase take place in aluminium alloys during heat treatment, as is known from works [1, 3, 4]. That is why, in order to determine the most influential technology factor, which improves the mechanical properties of D16 alloy welded joints, heat treatment of butt joints was followed by studying their microstructural features, achieved due to two isolated wires of different chemical composition, or embedded elements, the composition of which is given above.

Metallographic Investigations. Analysis of the alloy microstructural features showed that during consumable electrode welding at the speed of 32–33 m/h, high-temperature heating of the metal and its further cooling cause formation of a heterogeneous structure in the joint zone, inherent to fusion arc welding processes. The extent of structural transformations and volumes of precipitation or dissolution of the forming phases are determined by the term of the respective metal region staying in particular temperature ranges, which are due to welding speed. The processes of diffusion of alloying elements and additives included into the composition of this alloy, filler wires and embedded elements, determine the nature of local structural features in all the zones of the welded joint (Figs. 1–5). By the data of Refs. [4–9], during welding of alloys of D16 type, up to 7 diverse phase inclusions are usually observed in its structure. Some of them belong to intermediate ones, for instance, metastable θ' phase, which later on transforms into a stable equilibrium $\theta(CuAl_2)$ phase.

Weld microstructure is determined by chemical composition of the alloy and main Zv1201 wire. Structural morphology is quite homogeneous; it consists of solid solution and fine inclusions of $CuAl_2$ phase, as well as eutectic of $(\alpha + CuAl_2)$ type, characteristic for this alloying system. Inclusions of oxide films or microcracks are not observed in the welds, but individual pores of up to 0.1 μm size are found in the sites of excess phase precipitates. Their number and arrangement depend on chemical composition of additional filler materials. Fine equiaxed crystallites are found in the weld central part, and in the periph-

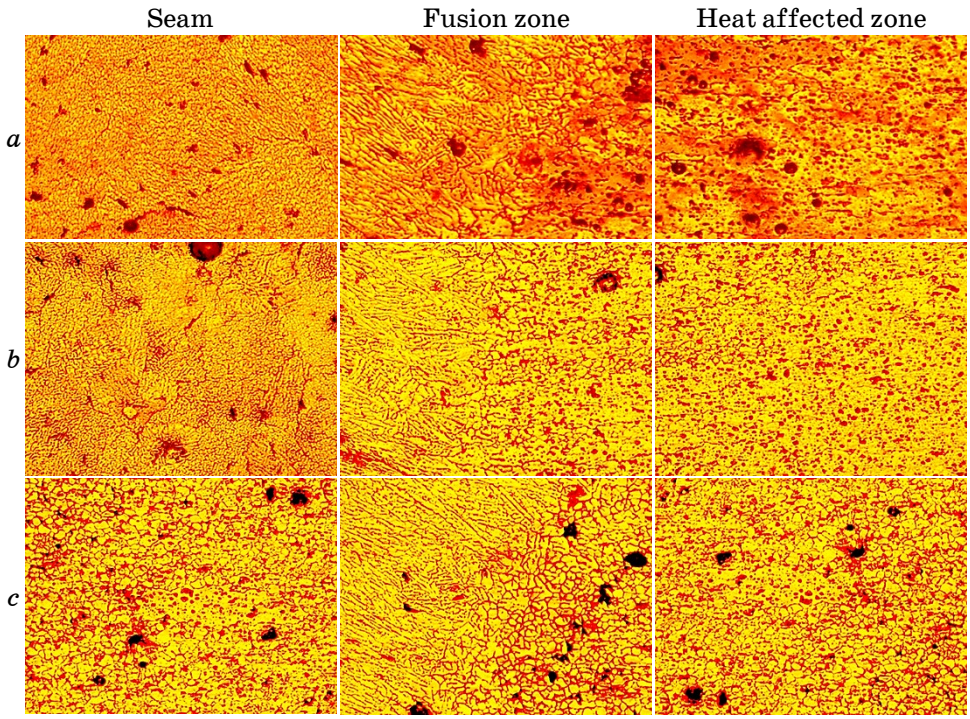

Fig. 1. Microstructure of D16 alloy welded joints made with batch-produced wire of Zv1201 grade: after welding (*a*), artificial ageing (*b*), and full heat-treatment cycle (*c*). ×320.

eral zone (line of its fusion with base metal), these are crystallites, oriented in the direction of the heat removal vector. A narrow zone of fine columnar crystallites is observed on the fusion boundary in the HAZ and eutectic interlayers are found near the intermetallic phase inclusions, which were formed at heating above the non-uniform solidus temperature [1].

Modification of the structure of welds formed as a result of feeding additional wire into the metal pool is cellular–dendritic, typical for arc welding with high density and dispersion of phase particle precipitates (Figs. 1–5).

A diverse nature of phase precipitates is observed across the entire weld thickness as the crystallites grow. This is attributable to a change of metal pool solidification rate in a wide range relative to the direction of the torch displacement at the specified welding mode. At application of ZvAK5 and ZvAK12 wires, an increase in the amount of low-melting eutectics is recorded in the structure of the weld and in the region of partial melting of the grains, predominantly on intercrystalline boundary. As at the specified welding mode, the solidification rate

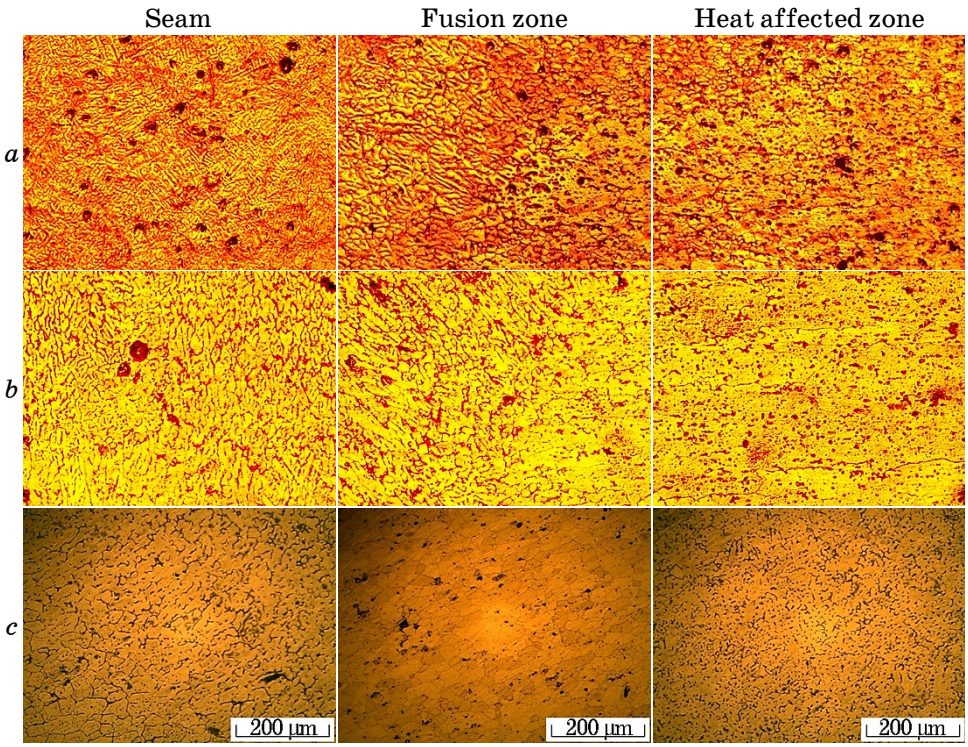

Fig. 2. Microstructure of D16 alloy joints produced with isolated Zv1201 + ZvAK5 wires into one a common pool: after consumable-electrode welding (*a*), artificial ageing (*b*), and full heat-treatment cycle (*c*). ×320.

changes in a broad range relative to weld width, a significant change in the nature of phase precipitates occurs with crystal growth. Eutectic precipitates of particles in the weld centre, where the solidification rate is higher, have thinner walls (10–15 μm) of intercrystalline layers, and the cell width is 8 μm smaller than near the fusion boundary (39–35 μm). A non-uniform degree of the change of phase-structural state of the metal leads to anisotropy of structural regions in the case of application of embedded elements in welding, Mg (Zn_2AlCu) and $Mg_3Al_2Zn_3$ intermetallic phase compounds are found in the structure. Zinc content in the applied elements determines them in the weld volume. Eutectic phase precipitation is observed predominantly on the intercrystalline boundary.

Performance of artificial ageing does not change the overall structure pattern, but it promotes increase of the number of strengthening phase precipitates in the intercrystalline gap (Fig. 2). Their number depends on their presence in the alloy or filler materials. It allows obtaining an oversaturated solid solution, which provides the respective

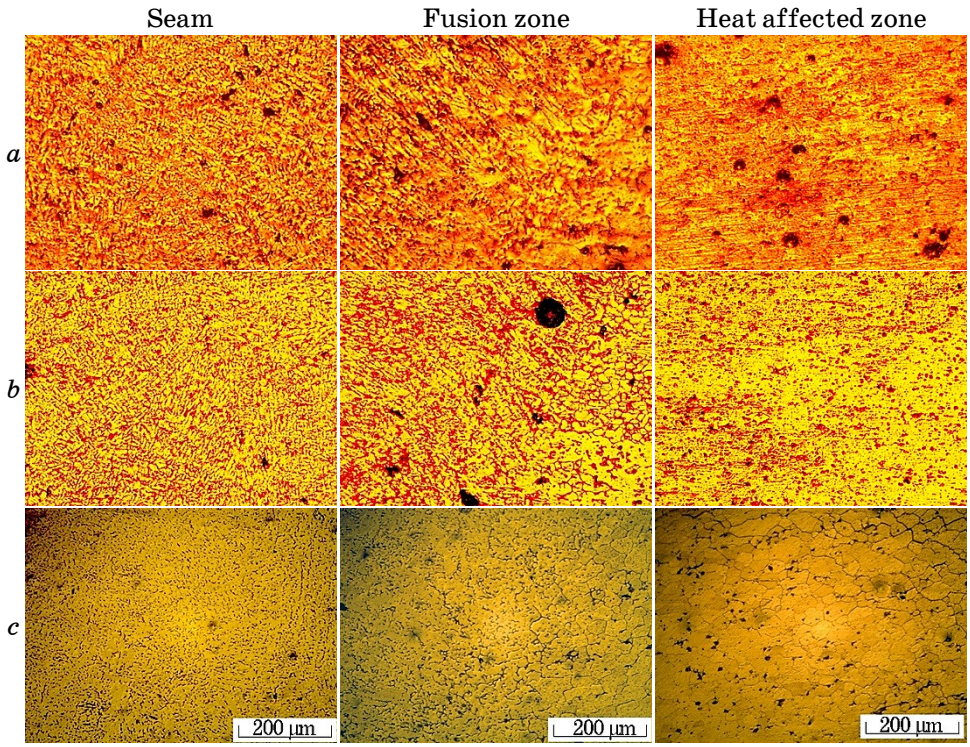

Fig. 3. Microstructure of D16 alloy welded joints produced with isolated Zv1201 + ZvAK12 wires into a common pool: after consumable-electrode welding (*a*), artificial ageing (*b*), and full heat-treatment cycle (*c*). ×320.

set of properties of welded joint specimens. Conducting full heat treatment, *i.e.*, quenching and artificial ageing of the studied welded joints of D16 alloy, significantly changes the location morphology of the phases, strengthening the metal. Their dispersion and number increase in all the zones (Fig. 3). This is due to the rate of decomposition of oversaturated solid solution during metal cooling in water at quenching. The shape and pattern of distribution of phase precipitates are related to chemical composition of the used materials. In the case of application of both ZvAK5 or AzAK12 wires and embedded elements from V92, V96 and 7056 alloys in welding, the number of phase inclusions in the crystalline structure volume is directly proportional to silicon presence in the composition of the wire and of zinc in the embedded elements.

Evaluation of Hardness Value. Measurement of the mentioned metal characteristic in different joint zones, namely, in the weld, on the fusion boundary and in the HAZ confirmed the above-given regularities of irreversible structural–phase transformations, taking place at high

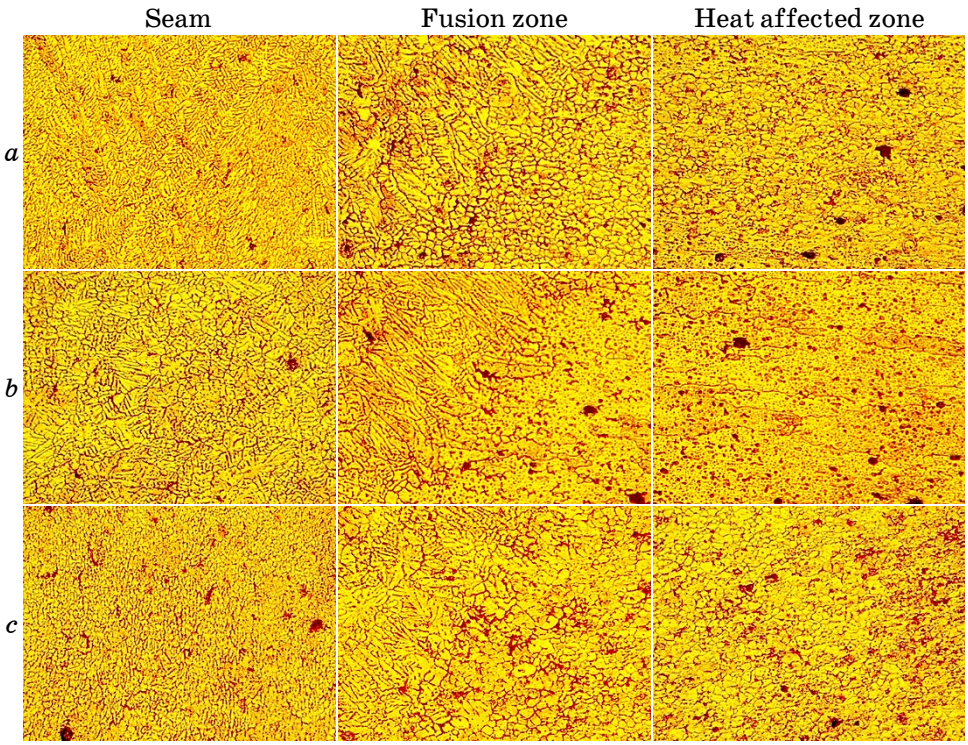

Fig. 4. Microstructure of welded joints of alloy D16 after welding with a fusible electrode and artificial ageing: ZSv1201 + 7056 (Zn = 9.5%) (*a*), Zv1201 + B96 (Zn = 8.5%) (*b*), Zv1201 + B92 (Zn = 3.5%) (*c*). ×320.

temperatures in welding D16 alloy. Modification of the structure of welds formed as a result of feeding additional wire into the metal pool is cellular-dendritic, typical for arc welding with high density and dispersion of phase particle precipitates (Figs. 1–5).

A diverse nature of phase precipitates is observed across the entire weld thickness as the crystallites grow. This is attributable to a change of metal pool solidification rate in a wide range relative to the direction of the torch displacement at the specified welding mode. At application of ZvAK5 and ZvAK12 wires, an increase in the amount of low-melting eutectics is recorded in the structure of the weld and in the region of partial melting of the grains, predominantly on intercrystalline boundary. As at the specified welding mode, the solidification rate changes in a broad range relative to weld width, a significant change in the nature of phase precipitates occurs with crystal growth. Eutectic precipitates of particles in the weld centre, where the solidification rate is higher, have thinner walls (10–15 μm) of intercrystalline layers, and the cell width is 8 μm smaller than near the fusion boundary

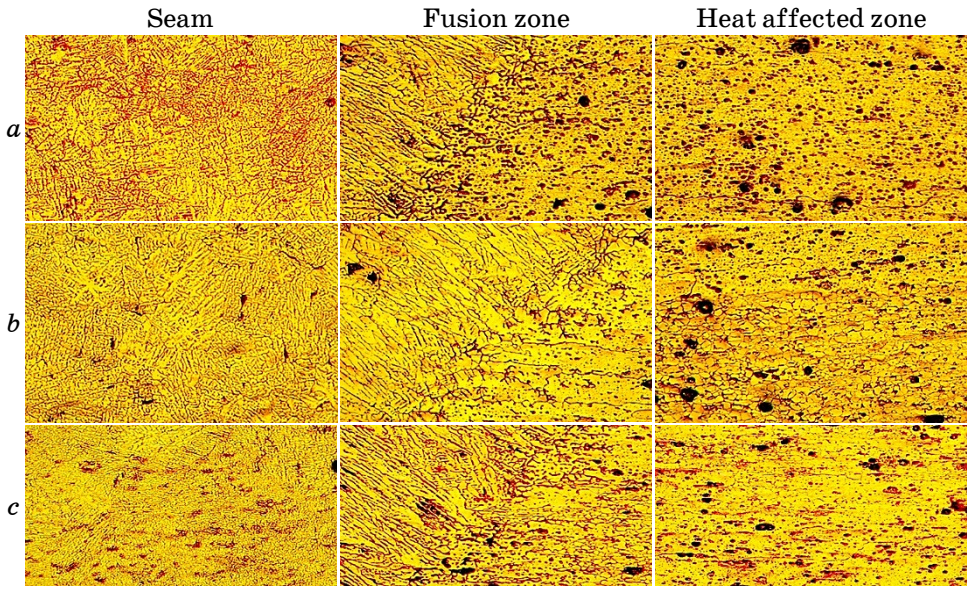

Fig. 5. Microstructure of welded joints of alloy D16 after welding with a fusible electrode and a full cycle of heat treatment: Zv1201 + 7056 (Zn = 9.5%) (*a*), Zv1201 + B96 (Zn = 8.5%) (*b*), Zv1201 + B92 (Zn = 3.5%) (*c*). ×320.

(39–35 μm). A non-uniform degree of the change of phase–structural state of the metal leads to anisotropy of structural regions in the HAZ. In the case of application of embedded elements in welding, Mg (Zn_2AlCu) and $Mg_3Al_2Zn_3$ intermetallic phase compounds are found in the structure. Zinc content in the applied elements determines them in the weld volume. Eutectic phase precipitation is observed predominantly on the intercrystalline boundary.

Distribution of hardness values practically reflects the kinetics of solid solution decomposition process and distribution pattern of decomposition products in the matrix during welding and heat treatment. Their dependence on chemical composition of the applied filler wires and/or embedded elements, thermal cycle of welding and heat treatment modes was established.

One can see from the data in Tables 2 and 3 that the change of the morphology of liquid eutectic phase distribution and temperature ranges of weld solidification in case of application of silicon-containing wires, causes an increase in primary dendrite dimensions in welds as a result of higher liquid eutectic mobility in the intergranular space and lowering of their formation temperature. Hardness level in this technology variant varies in the range of 12.5–20.1 units. Such a pattern of hardness distribution is due to interaction of alloying elements of the alloy and of filler materials under the temperature–time

TABLE 3. Influence of heat treatment on hardness of D16 alloy welded joints made by consumable electrode using batch-produced Zv1201 filler wire and embedded elements from Zn-containing alloys.

State of base metal and welded joint	Hardness, *HRB*									
	BM	Zv1201+7056 inserts			Zv1201+V96 inserts			Zv1201+V92 inserts		
		Weld	WJ	HAZ	Weld	WJ	HAZ	Weld	WJ	HAZ
After welding and natural ageing	65–67	90–91	61–87	59–65	89–90	61–85	59–65	89–90	62–88	60–65
Welding + artificial ageing		87–90	82–90	58–65	92–92	70–91	59–65	90–93	72–93	63–66
Welding + quenching + artificial ageing	100–102	98–99	100–101	100–102	99–99	100–101	99–102	98–99	100–101	97–102

conditions of consumable-electrode welding [5]. Modulation of the main parameters of welding mode with cycle time of 2.2 ± 0.2 s created the necessary thermo-physical conditions. This is accompanied by improved control of the process of drop transfer from the main wire, producing the appropriate metal pool shape and formation of a dense structure of welds. Such conditions ensure an increased amount of the solid solution, and promote higher density of precipitates of dispersed particles of the hardening phase, that influences the joint hardness.

By their analysis data, a slight increase (5–7%) in the level of hardness of the weld metal and zone of its fusion with the base metal is observed, after artificial ageing of the joints made with batch-produced ZvAK5 and ZvAK12 wires. This is, probably, due to a small number of secondary phase inclusion precipitates, found along the crystallite boundaries in the welds and base metal grains, and influencing the structure strength. In the HAZ, this value grows by only 3–5 units and reaches the base metal level in the naturally aged condition (59–65 units).

Application of embedded elements (from V92, V96 and 7056 alloys) as additional materials also causes an increase of metal hardness level by 2–5 units in different zones of the joint, compared to joints, made by batch-produced wires. The level of hardness value is determined by the amount of zinc in the composition of the respective additional embedded elements (Table 3).

Conducting a full cycle of welded joint heat treatment ensures a more significant increase in hardness value in all the structural zones. Irrespective of silicon presence in the filler wire, its level increases by 25–30% (Tables 2, 3). The greatest effect of hardness increase is observed in the weld. Similar to artificial ageing, hardness value depends

on silicon content in the additional filler wires. In the fusion zone, the difference in hardness values is just 1–2 *HB*, and in the heat-affected zone these values are similar.

Hardness level of D16-alloy base metal, which was artificially aged, increases by almost 10% relative to this value in the naturally-aged state, and it is equal to 100–102 *HRB* (Tables 2, 3). Performance of the full cycle of heat treatment of the joints, welded with embedded elements, creates a similar pattern of hardness change. Its level rises by 2–5 *HRB*, compared to joints made with application of silicon-containing filler wires. The hardness effect is determined by the amount of zinc in the additional materials.

Evaluation of Mechanical Properties. During mechanical tests for static tension, fracture of D16-alloy welded joints takes places in the HAZ subzone, where metallographic analysis revealed centres of formation of a network of brittle intermetallic phases located along the grain boundaries, because of grain coagulation. The fracture relief retains tough fracture regions, which is indicative of the mixed mode of joint destruction. In case of application of ZvAK5 and ZvAK12 filler wires, the ultimate strength of welded joints was equal to 186–188 MPa, on average, and that of weld metal was 180–187 MPa. Here, ductility value (bend angle) varied in the range of 27–44 degr. (Table 4). That is, during consumable-electrode welding, favourable conditions are in place for physicochemical interaction of alloying elements and additives of base metal and wires, containing silicon. It additionally expands the amount of eutectic of a balanced composition and improves the structural homogeneity of the welds, both in the weld centre, and on the fusion boundary with the base metal.

Performance of the operation of artificial ageing of welded joints does not cause any essential increase of the yield limit (Table 4). It increases only by 2–3% and remains on the level of 200 MPa, but the bend angle value somewhat decreases to 22–32 degr.

Fracture sites are coarse phase particles and insoluble intermetallics, located along the weld crystallite boundaries or in the zone of its fusion with the base metal. Performance of the operation of full heat treatment ensures an increase of welded joint strength to 282.8–298.2 MPa in specimens made with ZvAK5 and ZvAK12 wires. The joint fracture mode is similar.

Zinc presence in embedded elements from V92, V96 and 7056 alloys promotes an increase of joint strength level, due to its availability in $Mg(Zn_2AlCu)$ and $Mg_3Al_2Zn_3$ secondary phase components [1]. Performance of just the artificial ageing causes a slight increase in the strength of the joints made using embedded elements. Its value is equal to 195.8–198.0 MPa, and ductility is of 22–27 degr. compared to as-welded state (joint strength of 190–200 MPa, that of weld metal of 191–194 MPa, (bend angle) varies from 27 to 36 degr.). Zinc content in

embedded elements determines the level of joint strength and ductility (Table 4).

TABLE 4. Influence of technology variants at application of various filler materials for D16 alloy welding and of subsequent heat treatment on the joint mechanical properties.

Filler material grades	Mechanical properties of welded joints in different conditions													
	as-welded*						welding + artificial ageing*					welding + quenching + artificial ageing**				
	σ_t^{WJ}	σ_t^{WM}	α, degr.	Strength factor, K			σ_t^{WJ}	σ_t^{WM}	α, degr.	Strength factor, K		σ_t^{WJ}	σ_t^{WM}	α, degr.	Strength factor, K
	MPa			1	2		MPa			1	2	MPa			1
Zv1201 (base)	193.0	186.0	40	0.79	0.76		198.1	197.6	36	0.64	0.64	301.1	285.6	31	0.69
Zv1201 + ZvAK5	188.0	187.0	44	0.77	0.76		194.7	191.7	32	0.63	0.62	298.2	242.3	21	0.69
Zv1201 + ZvAK12	186.0	180.0	27	0.76	0.73		98.0	190.0	18	0.69	0.69	282.8	243.9	28	0.69
Zv1201 + 7056 alloy	194.0	190.	31	0.79	0.78		201.2	198.0	23	0.69	0.69	296.0	230.4	18	0.69
Zv1201 + V96 alloy	200.0	194.0	36	0.82	0.79		199.0	195.4	27	0.69	0.69	301.4	270.0	23	0.69
Zv1201 + V92 alloy	191.0	190.0	27	0.78	0.78		198.0	195.8	22	0.69	0.69	273.7	189.0	12	0.69

Notes: 1. Average values of strength ($\sigma_{t\,WJ}$, $\sigma_{t\,WM}$) and bend angle (α, degr.) of welded joints by the results of mechanical testing of three specimens. 2. Strength of D16 alloy base metal: after welding and natural ageing, after artificial ageing—310 MPa, after full heat-treatment cycle—340 MPa. 3. *—specimen fracture ran through the base metal in the HAZ. 4. **—specimen fracture ran along the weld axis and along the boundary of its fusion with base metal of D16 alloy. 5. Strength factor (1—welded joint—$K = (\sigma_B^{WJ}/\sigma_B^{bM})$WJ and 2—weld metal—$K = (\sigma_B^{WM}/\sigma_B^{bM})$) is given in comparison with the strength level of D16 alloy base metal in the natural condition, after artificial ageing and full heat-treatment cycle.

The highest strength of welded joints (up to 301.4 MPa) and weld metal (up to 296.0 MPa) is noted at application of V96 alloy. Specimen fracture at mechanical testing runs along the weld axis or boundary of its fusion with the base metal that reflects the dependence of the joint structure on the thermal-cycle effect in welding D16 alloy.

Performance of full heat treatment of joints made using embedded elements, increases the strength level to 273.7–301.4 MPa, and for weld metal to 189.0–270.0 MPa (Table 4). The level of ductility (bend angle) here varies from 12 to 23 degr. Strength increase depends on zinc presence in the filler material composition. In keeping with the data of Refs. [1, 3], weld strengthening can be achieved as a result of formation of dispersed precipitates of metastable η'-phase, the composition of which was determined to be $Mg_4Zn_{13}Al_2$ phase. The observed heterogeneity of excess phase and intermetallic cluster dimensions can be associated with silicon presence in Mg_2Si and $W(Al_xMg_5Cu_6Si_4)$ phases. Under the artificial ageing conditions, they dissolve in the liquid metal and strengthen it, but this increase is small. Zinc presence in the structure of welds, produced using embedded elements, promotes formation of $Mg(Zn_2AlCu)$ and $Mg_3Al_2Zn_3$ secondary phases, which increase the strength level of the joints and weld metal up to 301.4 MPa and 296.0 MPa, respectively. Specimen fracture under tension also occurs along the weld axis or the boundary of its fusion with the base metal. The fracture sites are phase particles, which do not dissolve in liquid aluminium, but form centres of extended intermetallic inclusions by coagulation. Presence of tough cells on fracture relief, alongside the quasi-cleavage elements, may be indicative of stress localization and concentration of ductile shear in individual structural regions, in keeping with the conclusions of work [2]. Thus, both the operation of artificial ageing and full heat-treatment cycle can be performed in order to improve the mechanical properties of D16 alloy joints in consumable electrode welding.

Their effectiveness is determined by the volume fraction of base metal phase particles and amount of alloying elements and additives at weld modifying. The degree of influence on the structure and mechanical properties depends on their amount, their ratio in the welded-joint zones and segregation along the boundaries of weld crystallites and base metal grains.

Moreover, it should be also noted that welded structure fabrication in the shop does not always provide favourable conditions for heat treatment performance. The above-mentioned problem arises in the case of absence of the necessary thermal furnaces, and also at large overall dimensions and considerable weight of individual structural elements, *etc.*, that is when the full heat treatment cycle cannot be implemented under the production conditions.

In this case, the operation of artificial ageing can be applied. In case

of absence of the mentioned production difficulties for performance of heat treatment of welded parts or components from D16 alloy, application of a full heat-treatment cycle of welded structural elements is more rational. At its realization, a more favourable structure of welded joints and optimal values of mechanical properties, namely, strength and ductility are achieved.

4. CONCLUSIONS

1. The nature of structural transformations taking place in D16 alloy during heat treatment, namely, artificial ageing or full cycle (quenching and artificial ageing), was evaluated. Their effectiveness is determined by the size of volume fractions of base metal phase particles and amount of alloying elements and additives, applied for modifying the welds made by consumable electrode. The extent of impact on the structure and mechanical properties is determined by their amount in the filler metal, segregation along the boundaries of weld crystallites and base metal grains. Weld microstructure is homogeneous, and consists of solid solution and finely dispersed inclusions of $CuAl_2$ phase and eutectic of ($\alpha + CuAl_2$) type. Alongside the solid solution, up to seven diverse phase inclusions are found in the structure, their combination influencing the level of welded joint mechanical properties.
2. The level of joint strength depends on the type of D16 alloy heat treatment, and it is determined by the geometrical dimensions and morphology of phase precipitates in the structure. Artificial ageing of joints made with batch-produced ZvAK5 and ZvAK12 wires results in their strength increase by 2–3% (190.0–195.8 MPa). Bend angle value is equal to 22–32 degr., which is due to transition of brittle intermetallic phases into the aluminium solid solution. Silicon presence in the composition of Mg_2Si and $Al_xMg_5Cu_6Si_4$ phases only slightly strengthens the joint. Conducting full cycle of welded-joint heat treatment raises the strength value largely (282.8–298.2 MPa), that is by 20–27% higher than under the conditions of artificial ageing. Specimen fracture runs along the weld axis or the boundary of its fusion with the base metal.
3. A similar regularity of strength increase is observed in joints welded with embedded elements. After artificial ageing, the strength level is equal to 195.8–198.0 MPa, and after the full cycle, it is of 273.7–270.0 MPa, depending on chemical composition and zinc content in the welds when using V92 and 7056 alloys. The greatest effect of strength increase in the joints (up to 301.4 MPa) and weld metal (up to 296.0 MPa) is observed at application of V96 alloy. Probably, this is promoted by formation of $Mg(Zn_2AlCu)$ and $Mg_3Al_2Zn_3$ secondary-phase compounds during weld solidification. Under the conditions of tension, the joints fail along the weld axis or the boundary of its fusion

with base metal.

4. It was confirmed that performance of heat treatment of D16 alloy joints made by consumable electrode, ensures an increase of hardness level, and it is determined by the volume of the respective transformations in different structural zones. After artificial ageing of the joints produced with ZvAK5 and ZvAK12 wires, hardness rises by 5–7% compared to as-welded state, and for those produced using embedded elements, it is 3–5% higher. The amount of silicon or zinc in the composition of the applied filler materials determines the extent of the effect of welded joint hardening. Performance of full heat treatment of the joint further increases their hardness by 2–5 *HRB*.

REFERENCES

1. Yu. V. Milman, N. P. Korzhova, and A. I. Sirko, *Inorganic Materials Science. Metals and Technologies* (Kyiv: Naukova Dumka: 2008).
2. K. V. Chuistov, *Ageing of Metallic Materials* (Kyiv: Akademperiodika: 2003).
3. V. S. Mashin, A. G. Poklyatskiy, and V. E. Fedorchuk, *Avtom. Svarka*, **9**: 43 (2005).
4. V. A. Lebedev, *Svarochnoye Proizvodstro*, **11**: 26 (2007).
5. A. M. Zhernosekov and V. V. Andreev, *Avtom. Svarka*, **10**: 48 (2007).
6. T. M. Labur, *Svarshchik*, **6**: 7 (2021).
7. D. Colchen, *Soudage Tech. Connexes*, **54**, Nos. 3/4: 3 (2000).
8. C. Wolverton, *Acta Mater.*, **49**, Iss. 16: 3129 (2001).
9. A. Norlin, *Svetsaren.*, **2**: (2000).
10. N. J. Teh, *TWI Connect.*, **143**, No. 4: 1 (2006).
11. A. Wenez, *Der Praktiker*, **5**: 74 (2005).
12. Metal 2002: Good Prospects for the Future as the Newly Industrialised Countries Gain Greater Importance, *IKB Deutsche Industriebank*, 14 (2002).
13. *GOST 6996-66, Welded Joints. Mechanical Testing Methods. Introd.* (Moskva: Standard Publ. House: 1967).
14. *GOST 7512-82 Nondestructive Testing. Welded Joints. Radiography Method* (Moscow: Standard Publ. House: 1983).
15. *GOST 1497-84 (ISO 6892-84, ST SMEA 471-88) Metals. Tensile Testing Methods*.
16. *GOST 9012-89. Brinell Hardness Measurement*.

Metallophysics and Advanced Technologies
Металофіз. новітні технол.
Metallofiz. Noveishie Tekhnol.
2025, vol. 47, No. 6, pp. 647–666
https://doi.org/10.15407/mfint.47.06.0647
Reprints available directly from the publisher

PACS numbers: 46.35.+z, 81.20.Hy, 81.40.Gh, 81.40.Jj, 81.40.Lm, 83.60.-a

Research into the Processes of Rolling Stamping of Ring and Flange Billets with a Complex Profile

V. M. Myhalevych[*], A. A. Shtuts[**], M. A. Kolisnyk[**], I. A. Zozulyak[**], A. P. Jelenich[**]

[*]*Vinnytsia National Technical University,*
95, Khmelnytskyi Highway Str.,
UA-21021 Vinnytsia, Ukraine
[**]*Vinnytsia National Agrarian University,*
3, Sonyachna Str.,
UA-21008 Vinnytsia, Ukraine

This article analyses the features of local deformation, which determine rolling stamping as an independent type of metal processing by pressure. Examples of the most complete realization of the advantages of stamping by rolling, which ensures the efficiency of industrial use, are given. In the priority directions of the development of science and technology, a special role is given to energy- and resource-saving. Modern national industries of mechanical engineering and metal processing, which are designed to increase the competitiveness of own products, are still largely based on the energy- and metal-intensive technological processes. The reduction of the energy and material costs is facilitated by the development and implementation of new metal processing by pressure in metalworking. This circumstance determines the priority of the development of agro-industrial production. The development of the agricultural sector and the need to increase its efficiency require improvement of technical support.

Key words: rolling stamping, metal pressure processing, cold three-dimensional stamping, deformation, forming, workpieces, yielding of metal.

Corresponding author: Volodymyr Markusovych Myhalevych
E-mail: vmykhal2@gmail.com

Citation: V. M. Myhalevych, A. A. Shtuts, M. A. Kolisnyk, I. A. Zozulyak, and A. P. Jelenich, Research into the Processes of Rolling Stamping of Ring and Flange Billets with a Complex Profile, *Metallofiz. Noveishie Tekhnol.*, **47**, No. 6: 647–666 (2025), DOI: 10.15407/mfint.47.06.0647

У роботі проаналізовано особливості локального деформування, які визначають прокатне штампування як самостійний вид оброблення металу тиском. Наведено приклади найбільш повної реалізації переваг штампування обкочуванням, що забезпечує ефективність промислового використання. У пріоритетних напрямах розвитку науки та техніки особливу роль відводять енерго- та ресурсозбереженню. Сучасні вітчизняні галузі машинобудування та металооброблення, які покликані підвищити конкурентоспроможність власної продукції, все ще значною мірою базуються на енерго- та металомістких технологічних процесах. Пониженню енергетичних і матеріяльних витрат сприяє розроблення та впровадження в металооброблення нових технологій оброблення металу тиском. Ця обставина зумовлює пріоритетність розвитку агропромислового виробництва. Розвиток аграрного сектора та необхідність підвищення його ефективности потребують вдосконалення технічного забезпечення.

Ключові слова: штампування обкочуванням, оброблення металу тиском, холодне тривимірне штампування, деформування, формування, заготівки, плинність металу.

(Received 27 December, 2024; in final version, 13 March, 2025)

1. INTRODUCTION

Approaches based on the concept of multistage technological processes are increasingly used in the study of a wide range of production processes. Examples can be the processes of chemical, atomic energy, aircraft and automobile manufacturing, *etc.* [1].

Mechanical engineering mass manufactures and uses axisymmetric parts of various designs such as rings, bandages and flanges. The annual demand, including Ukraine's, for details of this type varies widely and can reach tens of millions of pieces. According to foreign companies, when cutting, the material utilization factor (MMF) is 40–50%, and when using cold stamping, it is 75–80%. If we take into account the energy consumption for the production of steel and its processing per unit weight of the finished part, it is 66–82 mJ/kg during cutting, and 41–49 mJ/kg during cold plastic deformation [2, 3].

There are methods of processing metals by pressure, based on the action of the technological load in the conditions of a localized plastic cell. The essence of these methods is that the shape change at each moment of time is performed only over a portion of the volume of the workpiece, and when the centre of deformation is moved, it covers the entire volume. These are well studied and widely used in production operations of free forging, rotary forging, rolling, *etc.* (Fig. 1).

The technological processes of end rolling and the sphere of mobile stamping, to combine into rolling stamping, rolling of rings and discs, *etc.*, can be attributed to relatively new ones that have an insignificant level of application [4].

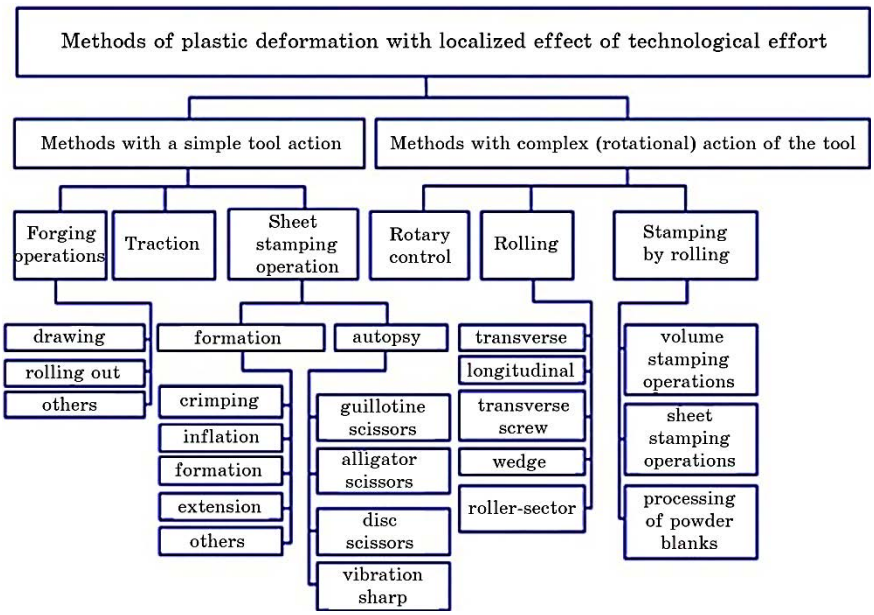

Fig. 1. Methods of plastic moulding and dissection with localized effect of technological force.

The problem of the limited level of production application of local methods is due to the fact that each of the listed technological processes has its own set of parts inherent in the form of which the process shows the highest efficiency.

Despite the fact that rolling stamping technologies have numerous advantages compared to traditional methods, as well as high economic and technological indicators, they have not been widely used today. National and foreign scientists pay considerable attention to the creation and development of resource-saving metalworking processes. These works have a relatively narrow spectrum of defining criteria and recommendations for the industrial use of rolling stamping.

Therefore, there are problems in the availability of available methods of typical technological design and development of national industrial equipment. The task of this work is a justification and demonstration of this direction, which, as a result of the improvement of the rolling deformation technology and the creation of specialized equipment, is gradually being formed into an independent production method of processing metals by pressure [5, 6].

Formulation of the problem. The purpose of the work is to study the rolling stamping processes of flat ring and flange blanks and to determine the ways of developing technological capabilities. Analysis of the nomenclature of parts in mechanical engineering showed (Fig. 2) that

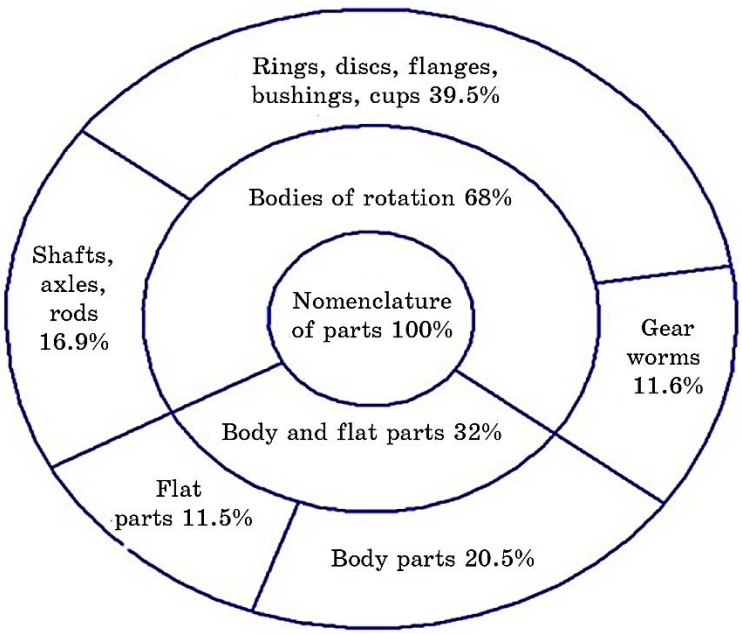

Fig. 2. Diagram of the distribution of the nomenclature of parts by structural features.

the vast majority of them are bodies of rotation (68%).

A large number of bodies of rotation include axisymmetric parts such as rings, disks, flanges, *etc.* In the production of these parts, mainly carbon, alloyed steel and non-ferrous metals are used. The main difficulties in the production of such parts by traditional methods consist in a sharp increase in the deformation force due to the closing of zones of hindered metal's flow.

To obtain such parts, methods are used in which the shape change is carried out by a tool that rolls over the surface of the workpiece. The production of parts under local loading allows achieving a plastic state in the deformation zone with a lower value of the technological effort.

For the preparation of blank parts such as rings, disks, flanges and bushings from plastic materials, the application of SHO processes can be effective. The main technological schemes of SHO are presented in Fig. 3 [2, 15].

Special development of SHO was achieved by the creation of such a direction as cold mechanical rolling (CMR). CMR processes make it possible to obtain axisymmetric, solid and hollow products of a complex profile with thin-walled elements of significant size by cold deformation [1, 16]. The shape change of workpiece can be implemented according to the following schemes (Fig. 4): deposition, landing of out-

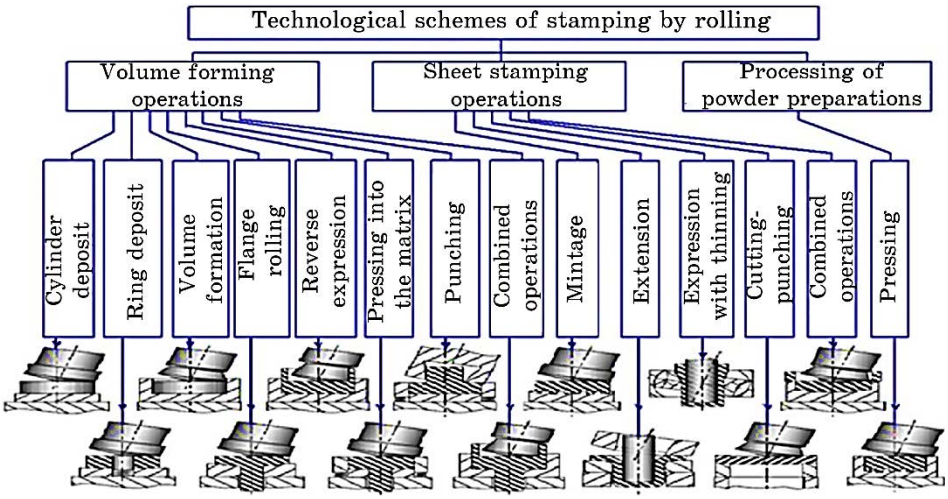

Fig. 3. Technological schemes of rolling stamping.

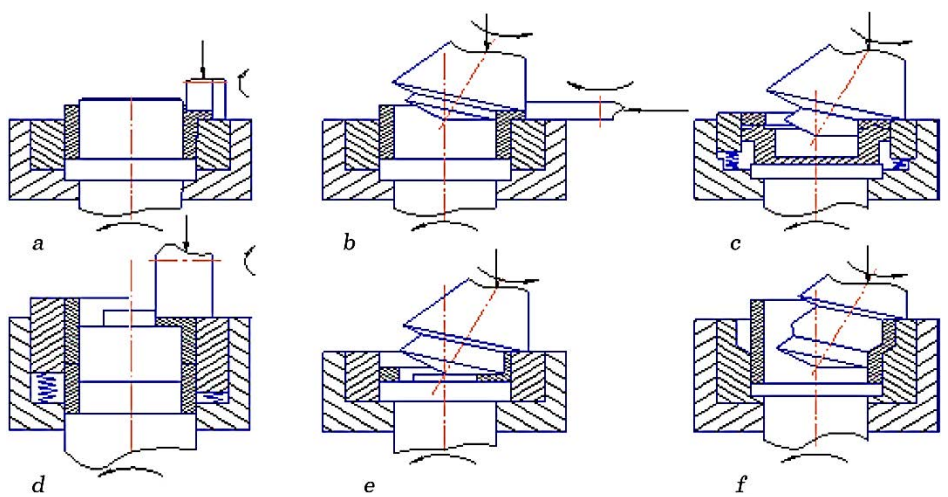

Fig. 4. Schemes of CMR: *a*, *b*—landing of the outer side; *c*—minting; *d*—landing of the inner side; *e*—reverse extrusion; *f*—distribution.

er and inner edges on tubular blanks; direct and reverse squeezing; dispensing, turning away, rotary hood, minting, *etc*.

Cylindrical or conical rolls are used as the main deforming tool in CMR. The cylindrical roll forms the inner and profiled outer edges according to the landing scheme.

A deforming tool in the form of a conical roll located at an angle to the axis of rotation of the part provides significantly greater techno-

logical capabilities. The conical roll makes it possible to form the part according to the schemes of disembarkation, direct and reverse extrusion, distribution, deposition, embossing [1]. When deforming with a conical roll, in some cases it is possible to refuse of using the mandrel, which simplifies the design of the equipment. The disadvantages of the conical tool are the complexity of the roll shape and the dependence of the tool size on the part size.

As blanks for rolling, you can use pieces of pipes and rods, stamped blanks and rings obtained by bending strips or rods with subsequent welding. The material of the blanks can be steel: structural steel—Art. 3, steel 20, steel 40; structural alloys—20X steel, 18XHT steel; ball bearings—SHKH15 steel; tool steel—steel 9XC, steel 4X13 and others, as well as non-ferrous metals and alloys.

The amount of single crimping is determined by the required degree of deformation, power parameters of the equipment, dimensions of the workpiece and mechanical characteristics of its material and can vary from 1–3 mm at the initial stage of deformation to 0.05–0.1 mm at the calibration stage. The final deformation of the part occurs, in most cases, in 10–30 revolutions or within 0.1–0.25 min. The shape and dimensions of the product are determined by the rolling scheme and the design of the equipment.

The main parameter that evaluates the suitability of metals for processing by the mechanical rolling method is sufficient plasticity.
The main factors that limit the technological possibilities of CMR processes are the destruction of the material, distortion and folding of the workpieces.

Deformability of workpieces in a real technological process depends on the shape change scheme, plasticity of the material, parameters of the process and the workpiece. The most dangerous schemes due to destruction are the landing of the outer edge, distribution and removal of tubular blanks.

When the outer edges are planted, the deformation limit before failure decreases with an increase in the ratio of the height of the part of the workpiece exposed to rolling to the wall thickness.

The stress state of the workpieces was evaluated using the indicator $\eta = (\sigma_1, \sigma_2, \sigma_3)/\sigma_u$, where σ_1, σ_2, σ_3 are the main stresses, σ_u—stress intensity [7]. The processing of the obtained results by the method of least squares made it possible to determine the ways of deformation of metal particles on the free surface of the edge in the co-ordinates 'intensity of deformation (ε, u)–stress state indicator' in the form of a dependence

$$\eta = k\varepsilon_u - n \,. \qquad (1)$$

It was experimentally established that the angle of inclination of the

TABLE 1. Technological characteristics of semi-automatic machines for CMR.

Parameters	Dimensionality	Model		
		КО9013	СО424	САО424
Strain force	[kN]	125	250	630
Matrix rotation speed	revolutions per wave	125	200	200
The power of the rotation drive	[kWt]	6	18.5	30
Productivity	details per hour	240	150	100
The diameter of the initial workpiece	[mm]	60	125	250
The edge width of the finished part	[mm]	15	25	40
The height of the edge of the finished part	[mm]	10	15	25
Overall dimensions of the machine				
Length	[mm]	2000	3500	4600
Width	[mm]	2000	1240	2000
Height	[mm]	1200	1240	1500
The weight of the machine	[kg]	3000	3600	15000

roll and the displacement of its top from the axis of the workpiece have a significant influence on the deformation path. With a constant angle of inclination of the roll $\alpha = 10°$ and the absence of its displacement, the main influence is exerted by factors h_0/b_0 and δ/b_0 (Fig. 5);

$$d_p/d_0 = \\ = \exp\{0.865\varepsilon_{*c}(\eta = 0)\exp(-\eta_к \ln\lambda)w - 0.14[\varepsilon_{*c}(\eta = 0)\exp(-\eta_к \ln\lambda)w]^2\}. \quad (2)$$

The limiting diameter of the outer edge of the rolled blank can be determined from the ratio, where is the value of the indicator at the point of intersection of the deformation path of the material particles of the dangerous zone of the workpiece with the plasticity diagram; coefficient of influence of deformation history on plasticity. When by rolling out, the outer sides $w = 1.2–1.35$.

Materials with a gentle plasticity diagram $(\varepsilon_p(\eta = -1)/\varepsilon_p(\eta = 0) < 1.5)$ can be destroyed not on the free surface of the edge, but in the zone with maximum deformations at a distance from the inner surface of the original pipe blank. In this case, the admissible degree of deformation must also be checked by the marginal degree of burst deposition [1–3];

$$h_0/h_p = \exp[\varepsilon_{*c}(\eta = 0)\exp(1.5\ln\lambda)]. \quad (3)$$

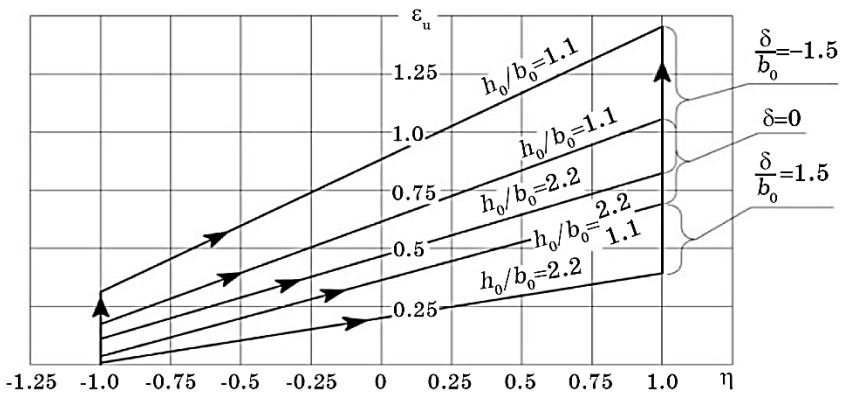

Fig. 5. Ways of deformation of the free surface of the outer side during landing.

In Figure 6, workpieces are shown with their external and internal edges, obtained according to the landing scheme for a blank with $2 < h_0/b_0$ when using a purposeful displacement of the top of the roll from the centre of the workpiece.

When rolling tubular blanks according to the scheme of landing the outer sides, in case $h_0/s_0 > 2–2.5$, the wall is curved and a fold is formed; this is a technological limitation of the process due to the loss of stability of the workpiece. To avoid the formation of folds when rolling blanks with a relative wall thickness $s_0/d_0 < 0.1–0.12$ and the relative initial height $h_0/s_0 > 3$ of the formation of the outer sides can be carried out according to the deburring scheme. The workpieces deburred by the CMR method are shown in Fig. 7.

$$\delta = \frac{s_0}{(1,5\ldots2)\mu}, \tag{4}$$

where μ is the coefficient of friction on the surface of the rolls-workpiece.

Unrolling of workpieces according to the deburring scheme is accompanied by the appearance of significant tensile stresses, so this type of unrolling can be subjected to materials with high plasticity,

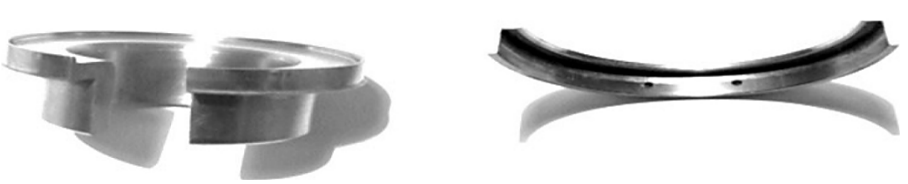

Fig. 6. Blanks with an outer and inner edge, obtained by landing with a purposeful displacement of the top of the conical roll.

Fig. 7. The workpiece obtained by debarring: at the intermediate and final stages.

a *b* *c*

Fig. 8. Scheme of direct extrusion–calibration and the appearance of the obtained blanks: *1*—blank, *2*—clamp, *3*—matrix, *4*—mandrel, *5*—roll, *6*—ejector.

which is characterized by the value of the relative narrowing of the neck when the sample is stretched $\psi_{\varnothing} = 60...65\%$.

The production of parts from steels 10, 20, 12X18N10T and copper M0b showed that deburring of rolling allows obtaining high-quality edges of significant sizes, including and with a thickness significantly less than the wall thickness of the original workpiece.

Technological schemes of direct extrusion–calibration and combined deformation with deposition and reverse extrusion are more favourable from the point of view of metal deformability [7]. According to the first scheme, thrust bearing rings and parts of cam clutches were obtained (Fig. 8).

The workpiece in this case is a ring obtained by cutting from a sheet on a stamp or cut from a pipe. The material of the bearing ring is bearing steel. Application conical roll with $\alpha < 10°$ allows reducing the centrifugal flow of the material and the intensity of the formation of external burr. In the rolling process, a track of the rolling elements, end surfaces with chamfers, outer and inner diameters of 8–9 accuracy quality are formed. The surface roughness of the raceway is $R_a = 0.2–0.4$ μm; the other surfaces are $R_a = 0.8–2.5$ μm. The rolling time is of 4–5 seconds.

Figure 9 shows the products obtained according to the technological scheme of deposition with reverse extrusion.

Thus, by purposefully applying various technological schemes of SR, it is possible to obtain high-quality products of various shapes, and

a *b*

Fig. 9. Complicated profiled products obtained by rolling with a cylindrical roll: *a*—flange with a collar; *b*—element of the body of the electrovacuum device.

using an approach based on deformability criteria, determine the suitability of the material for processing and the final dimensions of the products.

2. PRESENTATION OF THE MAIN RESEARCH MATERIAL

Rounded flat workpieces are quite common in the manufacturing industry. Traditionally, such workpieces are obtained by cutting or cutting from a sheet, which is accompanied by significant waste in the form of jumpers. Therefore, the issue of effectively obtaining thin workpieces for subsequent MRM operations is quite relevant [8].

Despite the development of stamping processes with improved contact friction conditions [9, 10], the main operation for obtaining thin round workpieces remains their cutting from a sheet. At the same time, the quality of the blanks does not always meet the requirements due to the initial anisotropy and different sheet thicknesses.

In the further extraction of products from such blanks, the main factor limiting technological possibilities is the destruction of blanks in the most dangerous local zones. Ruin is preceded by a loss of deformation resistance or a local thinning of the workpiece in the form of a neck, from the moment of its formation, an increase in the degree of extraction becomes impossible.

Rounded parts with a relatively small height are difficult to manufacture; $h/d < 0.3$ with a diameter of no more than 300–350 mm. In this case, high-power and high-rigidity hot stamping press equipment is required, and highly alloyed, expensive steels are required for the production of stamping equipment.

In this regard, the article examines the technological process of stamping by rolling (SR) of flat annular and flange workpieces.
SR allows obtaining blanks of the required shape by reshaping them from square, round and ring. According to the proposed technology, the sheet is cut into square blanks without waste, which are reshaped

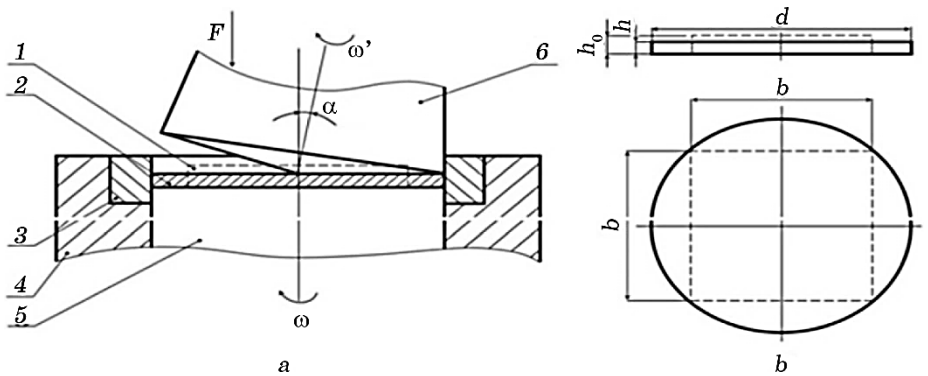

Fig. 10. Scheme of reshaping of workpieces by the SR method (*a*), view of the original square and rolled round workpiece (*b*): *1*—workpiece, *2*—product, *3*—matrix, *4*—spindle, *5*—ejector, *6*—roll.

by the SR method (Fig. 10.) into flat round ones or with the required thickness profile. Thus, the reshaping of the workpiece is carried out according to the scheme of precipitation by the SR method.

In the case of reshaping of workpieces by the SR method, the possibility of controlling the intensity and direction of the metal`s flow by shifting the roll is practically excluded, since it is impossible to ensure the shift of the top of the roll due to the use of a die-gauge. In this case, centrifugal drawing of the metal is preferred. At the same time, the maximum flow intensity is observed at a distance $r < 0.2R$.

The debugging scheme shown in Fig. 11 according to the classification of rolling stamping processes [11, 12] should be classified in the first group - waste-free production of flat workpieces.

When the metal flows in different axial directions of the workpiece, three stages of forming are observed.

At the first stage, there is an intensive redistribution of the volume of metal [12] (in the reverse direction from the applied force *P*) and in the radial (along the line *H*–*H*) directions (Fig. 12). In the tangential direction, the redistribution of the volume of metal is slowed down, which is confirmed by the difference in the values of a_i and b_i (Fig. 4). The resistance to deformation throughout the volume of the part is also different, on the surface of the interaction of the initial blank with the punch I, the outer layers move more intensively than the inner layers due to the high friction of the initial workpiece along the surface of its interaction with matrix II (this is obvious when considering the contact area of the tool with the original workpiece).

Because of this, additional loads appear: on the outer compressive surface (since each inner layer restrains the movement of the adjacent outer one) and on the inner one—tensile ones (since each outer layer moving faster than the neighbouring one captures it with itself).

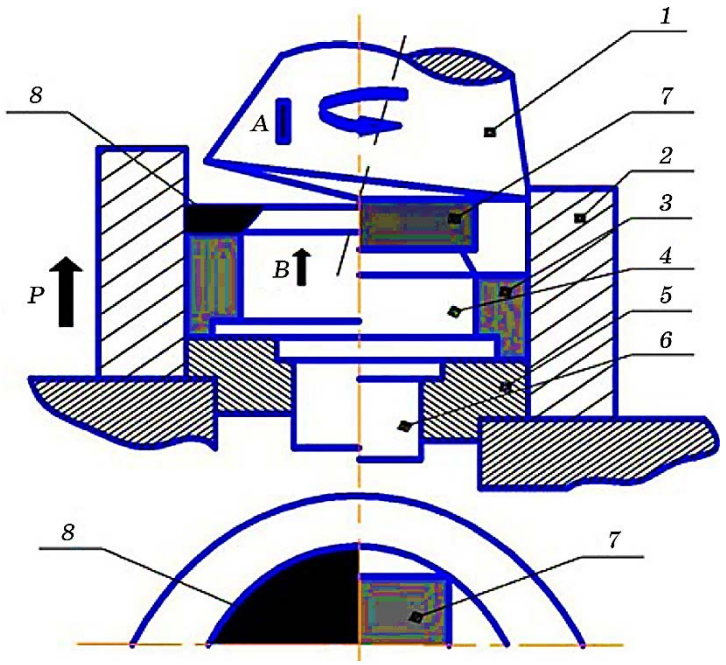

Fig. 11. Setup scheme for rolling stamping of flanged parts and blanks: *1*—punch; *2*—container; *3*, *4*—matrix; *5*—ring; *6*—ejector; *7*—starting workpiece; *8*—finished part.

As a result of equalizing the load, there is a zone of the inner layers with additional radial load, which increases to the outer surface. The fact that the surface layers of the metal move more intensively than the lower layers is confirmed by examining the cross section of the workpiece in the first stage of the process (Fig. 13).

The beginning of the second stage of the process is determined at the moment of contact of the initial workpiece with the matrix on surface III. Although the movement of the volume of metal does not change its character in relation to the first stage, it occurs with increasing resistance to deformation, which is explained by the intensive formation of the lower part of the workpiece. In the directions along the line H–H, the radial flow of metal increases, and at the moment of filling the outer diameter of the container, it changes its direction, at the same time, in the direction along the line S–S, the tangential flow of metal prevails, and at the moment of changing the direction of the flow of metal along H–H, an increased hydrostatic pressure, the increase of which determines the filling of the lower part of the flange [13].

A characteristic feature of the first two stages of forming is the presence of internal circular steps when the initial and final stages of the process are formed, and the height difference $H2 - H1 = S$ gives

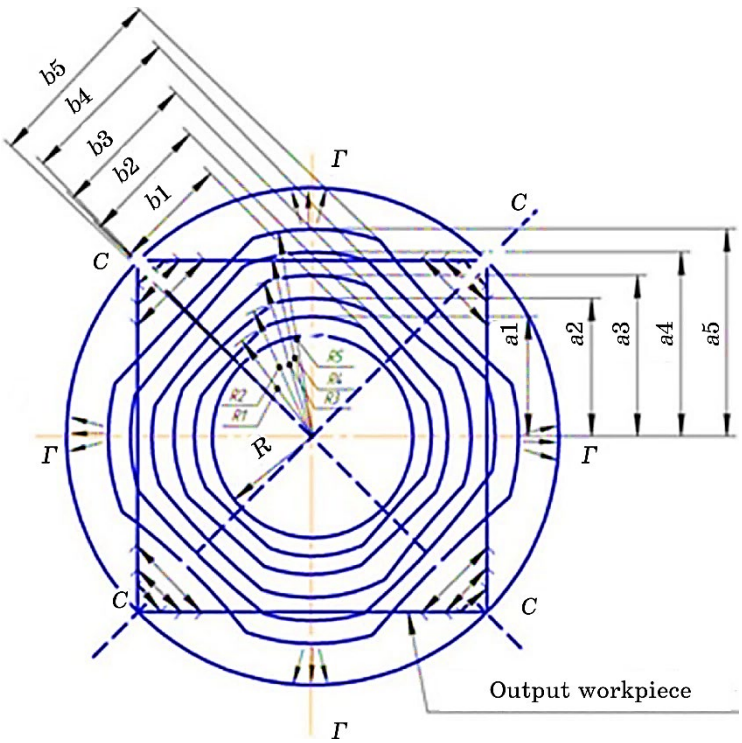

Fig. 12. Scheme of metal flow in the flange part of the part during rolling stamping from a ring blank. *H*–*H*—radial metal flow conversion line *S*–*S*—tangential metal flow conversion line.

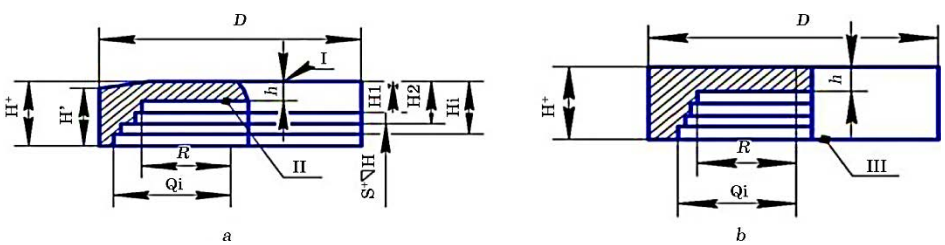

Fig. 13. Cross-section of the workpiece at the stage of the process: *a*—along the *G*–*G* plane, *b*—along the *S*–*S* plane.

the feed value for one rolling cycle.

The formation of straight sections on the *S*–*S* line is a consequence, the distortion forms rings due to the support at the point of contact of the workpiece with the diagonal direction.

The third stage of the process is the calibration of the canvas and the inner diameter of the workpiece. The process occurs without a signifi-

TABLE 2. Dimensions and parameters of the rolling stamping process of ring and flange workpieces.

№	Parameter names	Marking	Unit of measurement	Parameters
1.	Diagonal of the original workpiece	L_d	[mm]	186 ± 240
2.	The thickness of the original workpiece	H_{sum}	[mm]	16
3.	Angle of inclination of the axis of the punch	θ	(degree)	2
4.	Axial feed of the tool	S	[mm/turn]	1.7
5.	Heating temperature	T	[°C]	740
6.	The maximum force of the stamp	P	[kN]	2300

cant increase in deformation force [14].

In the analysis stage of the study, a device for the production of blanks and parts by the rolling stamping method is proposed [15].

The device for implementing the method contains a matrix *1*, a rolling punch *2* and an ejector *3*. The punch *2* receives a rolling motion from a special drive. The matrix *1* and the ejector *2* are mounted on the press table and can move vertically from their drives.

Research of the obtained products in terms of accuracy corresponds to 10–11 quality, the surface roughness is 3.2 μm [16].

Calculation of the workpiece during rolling stamping.

1. Initial conditions (Fig. 14.):

$$C = D,\ V_d = V_z, \tag{5}$$

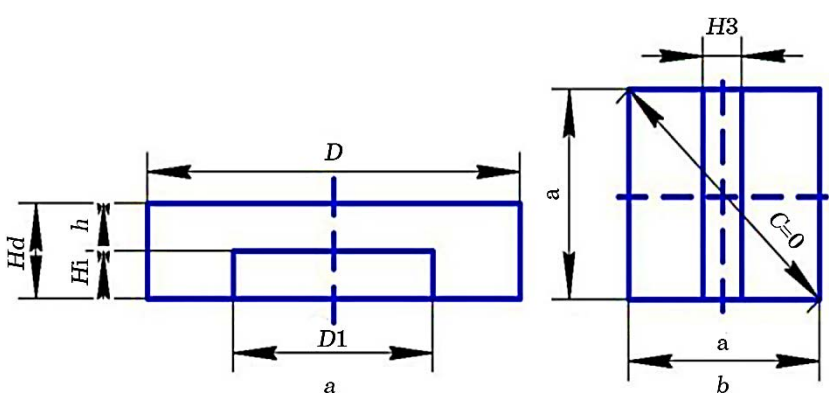

Fig. 14. Dimensions of the finished part (*a*) and the initial blank (*b*).

where C—diagonal of the workpiece; D—outer diameter of the part; V_d, V_z—the volumes of the part and workpiece.

2. Variation intervals:

$$D_1/D = 0.1, 0.2, 0.3, 0.4, 0.5, 0.6, 0.7, 0.8, 0.9,$$
$$\text{Sun} = 3.5, 10, 12, 14, 16, 20,$$
$$h = 0, 1.5, 4,$$

where D_1—inner diameter of the part; H_d—the height of the part; h—is the thickness of the jumper.

3. Conclusions of calculation formulas:

$$V_d = (\pi D^2 H - \pi D_1^2 H_1) / 4, \quad (6)$$

$$V_z = a^2 H_3, \quad (7)$$

where a—side of the workpiece:

$$a = \left(\frac{C}{\sqrt{2}}\right)^2; \quad (8)$$

but $C = D$, then,

$$a = \left(\frac{D}{\sqrt{2}}\right)^2. \quad (9)$$

From formula (7),

$$H_z = \frac{V_z}{a^2}. \quad (10)$$

However, according to condition (5), V_z is equal to V_d.

After transformation (10), we will get the original formula for calculating the height of the workpiece:

$$H_z = 1.57(H_d - B^2 H_1). \quad (11)$$

Power parameters and forming processes during rolling stamping of flat annular and flange blanks from a square workpiece. In the processes of three-dimensional rolling stamping, at each moment of time, the initial workpiece is in contact with the tool only with part of the end surface, thus forming a local centre of deformation [7].

The location of the centre of oscillations at the top of the conical (rolling) of the tool, which determines the dependence of the total stamping force on the angle of inclination of the tool axis θ, the feed of the workpiece S, the shapes and geometric dimensions of the initial workpiece.

Rolling stamping can be carried out in two ways:

- with constant effort, when the required shape change is achieved due to a certain number of rolling cycles under load [17];
- with constant axial feed of the tool (workpiece) in one rolling cycle.

In the latter option, the punching force will increase to a maximum by the end of the punching, but by this time the deformation will be over, the endurance under full load is not required, the rolling drive will not experience peak loads at the initial moment of punching, and the productivity will be higher.

As a rule, according to the first option, stamping is carried out on low-power equipment. In the initial stage of the press process, maximum effort is given, while the feed will inevitably decrease due to the increase in the size of the workpiece. When carrying out such a process, there is uneven deformation along the height and re-sticking of the surface layers of the workpiece, which are in contact with the rolling tool.

Pre-stamping, *i.e.*, the final operation of complete shaping of the workpiece, is carried out at very small feeds, the locality factor X increases, and the productivity at the same time decreases significantly.

In this regard, it is advisable to conduct a process with a constant supply. In this case, the force P_{os} is increasing with each run-in cycle, and the locality coefficient λ will keep a constant value.

The calculated feed at a constant number of running-in of the spherical moving mechanism is slightly less than the actual feed. Despite this, the effort is not observed, since the local feed does not have time to show itself during the rolling cycle.

As a result, productivity increases and the probability of defects detected in the case of conducting the process with constant effort decreases SR. In this case, the requirements for the equipment of the power press and the rolling mechanism change accordingly.

Researching [18] in this direction was carried out on low-power equipment and did not reveal all the advantages of rolling stamping.
Based on the above, we will consider the characteristic features of stamping round flanges from square and strip blanks with constant feed.

Figure 15 shows the diagrams of the established process of rolling stamping with square and strip workpieces.

To calculate the area of the local centre of plastic deformation of the spot of contact with the surface of the rolling tool, we use the formulas given in [19], where the stress-deformed state of the metal during this process is most accurately described.

It should be noted that the law of the smallest perimeter is not observed when stamping round workpieces from square or strip workpieces. In this regard, the boundaries of the square and strip workpieces remain practically straight. This allows you to determine the local centre of deformation of the contact spot in the direction perpendicu-

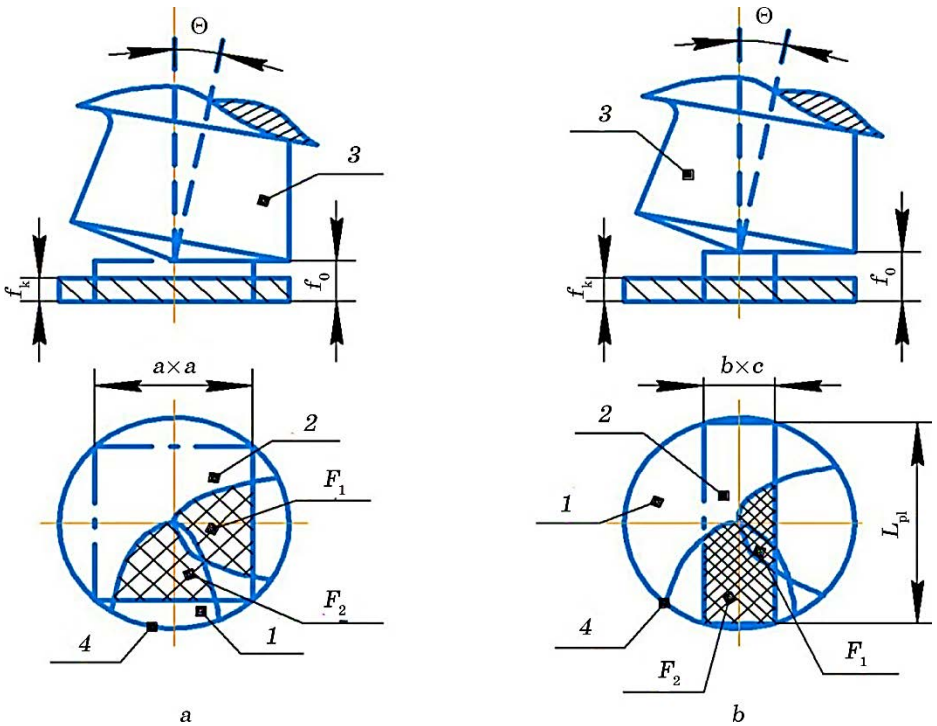

Fig. 15. Scheme of rolling stamping of flat workpieces (circles): *a*) punching from a sheet; *b*) punching from a strip. *1*—stamped circle; *2*—initial workpiece; *3*—punch; *4*—matrix.

lar to the border of the square or strip workpiece.

The ratio of the area of the contact spot in different directions is approximately 20% at the initial moment of stamping. As the stamp fills the circular cross-section of the stamped workpiece, the ratio decreases and when it is completely filled in all directions, it becomes equal (this is the final stage of stamping).

Correspondingly, the resistance of the metal and the contact pressure change due to the change in the contact areas in the local centre of plastic deformation, that is, the metal is easily stamped in the direction of the face. It explains that the appearance in the direction of the face, which is shown in work [20–23] based on the example of the loss of stability of the workpiece in the tangential direction perpendicular to the boundary.

The intensive flow of metal in the tangential direction in the corner zones of square or strip workpieces remained unclear.

In Figures 16–18, the nature of the flow of metal from its initial stage to the final output product is shown that shows how the metal is redistributed around the circle. Figure 17 shows the diagram of the

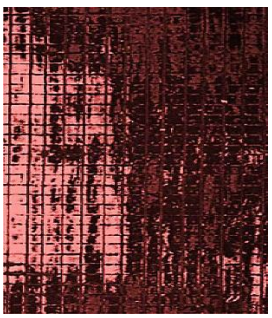

Fig. 16. Output blank from the strip.

Fig. 17. Intermediate shape of the blank when punching a circle from a strip in case of loss of stability (bend) in the region of the side face, parallel to the axis of the strips.

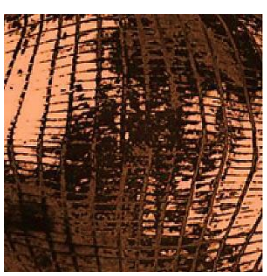

Fig. 18. The final shape of the workpiece.

areas of the contact spot during rolling stamping from a square blank, where their difference is clearly visible.

The difference in contact areas in the direction of the boundary and in the direction of the corner of the workpiece leads to an increase in the feed in the area of the faces, from which the tool already rolls onto the corner zone. This causes an intense tangential flow of metal in the corner zones of a square or strip workpiece, and sufficiently pronounced conditions perpendicular to the boundary disappear along stamp filling measures. The consequence of this is high accuracy in the

thickness of the workpieces [24, 25]. It was previously shown that, even on thin workpieces, the ratio $N/D = 0.02$ corresponds to the accuracy of cold-rolled sheet without calibration.

3. CONCLUSIONS

The stress–strain state of workpiece material is an important characteristic necessary for assessing deformability and determining force parameters. Among the effective methods of NDS analysis are the grid method, hardness measurement, and microstructural analysis.

Direct extrusion by the SHO method was considered by us using the example of forming end teeth of a gear sleeve. To increase the accuracy of determining deformation intensity in cross-sections of workpieces, a highly strengthening material, namely, copper M0b, was chosen for physical modelling.

As a result of constructing graduation graphs and measuring hardness in workpiece cross-sections, as well as grids on workpiece surfaces, the distribution character of stress and strain intensity, as well as the stress state index in the plastic area, was obtained. The most rigid stress state scheme is observed at the apex of the extruded teeth, but here the least deformation occurs. The largest deformations are formed at the base of the tooth, but the stress state is close to uniaxial compression.

Reverse extrusion by the SHO method was also modelled on copper M0b. NDS analysis showed that the most deformed zone is the thin-walled element zone, which is formed because of metal flow from the contact plastic spot area of the roller with the workpiece. Maximum deformations are observed in this zone, gradually decreasing as you move away from the contact surface.

The flange part of the workpiece is a zone of relatively uniform deformation. Dependences of the growth of deformation intensity on the periphery of the flange from the relative increase in its length were constructed.

Based on the analysis results, paths of material particle deformation in dangerous zones due to possible workpiece destruction were constructed, which were then used to assess workpiece material deformability.

The possibilities of direct extrusion are limited by the complexity of force transmission from the roller to the opposite end face of the workpiece and significant contact stresses. Therefore, this operation is more suitable for calibration or forming of small-size workpiece elements, which should be taken into account when developing corresponding SHO technological processes.

Further research in this direction will expand knowledge of material deformation mechanisms during stamping by extrusion and develop

new approaches to optimizing technological processes in the production of metal parts.

REFERENCES

1. V. Matviychuk, A. Shtuts, M. Kolisnyk, I. Kupchuk, and I. Derevenko, *Periodica Polytechnica Mechanical Engineering*, **66**, No. 1: 51 (2022).
2. V. Matviychuk and A. Shtuts, *Construction of Curve Boundary Deformations of Metals. In Traditional and Innovative Approaches to Scientific Research: Theory, Methodology, Practice* (Riga, Latvia: Baltija Publishing: 2022).
3. A. Shtuts, M. Kolisnyk, A. Vydmysh, O. Voznyak, S. Baraban, and P. Kulakov, *Key Engineering Materials*, **844**: 168 (2020).
4. A. A. Lebedev and V. M. Mikhalevich, *Strength of Materials*, **35**: 217 (2003).
5. V. Mykhalevych, Y. Dobraniuk, V. Matviichuk, V. Kraievskyi, O. Tiutiunnyk, O. Smailova, and A. Kozbakova, *Informatyka, Automatyka, Pomiary w Gospodarce i Ochronie Środowiska*, **13** (2023) (in Poland).
6. V. M. Mikhalevich, Y. V. Dobranuk, V. A. Kraevsky, and O. V. Mikhalevich, *Buletinul Institutului Politehnic din Iaşi*, **LIV(LVIII)**, Nos. 3–4: 49 (2008) (in Romania).
7. S. Neutov, M. Sydorchuk, and M. Surianinov, *Materials Science Forum*, **968**: 227 (2019).
8. V. Matviychuk, V. Mikhalevich, and A. Shtuts, *Vibrations in Engineering and Technology*, Iss. 1 (108): 63 (2023).
9. I. Kupchuk, M. Kolisnyk, A. Shtuts, M. Paladii, and A. Didyk, *Technical Science: Colloquium-Journal*, No. 16 (103): 40 (2021).
10. A. Shtuts, M. Kolisnyk, and V. Yavdyk, *MOTROL: Commission of Motorization and Energetics in Agriculture*, **20**, No. 1: 19 (2018).
11. M. Surianinov and O. Shyliaiev, *International Journal of Engineering and Technology (UAE)*, **7**, No. 2.23: 238 (2018).
12. I. Kupchuk, M. Kolisnyk, A. Shtuts, and M. Paladii, *Bulletin of the Transilvania University of Braşov. Series I: Engineering Sciences*, **14** (63), No. 2: 1 (2021).
13. V. A. Matviychuk, M. A. Kolisnyk, and A. A. Shtuts, *Technology, Energy, Transport of Agricultural Industry*, **3** (102): 77 (2018).
14. V. Fomin, M. Bekirova, M. Surianinov, and I. Fomina, *Materials Science Forum*, **968**: 383 (2019).
15. S. G. Karnaukh, O. E. Markov, L. I. Aliieva, and V. V. Kukhar, *The International Journal of Advanced Manufacturing Technology*, **109**, Nos. 9–12: 2457 (2019).
16. M. V. Lyubin and O. A. Tokarchuk, *Vibrations in Engineering and Technology*, **1**(92): 56 (2019).
17. N. R. Veselovska, V. V. Turich, and V. S. Rutkevich, *Vibrations in Engineering and Technology*, **2**(85): 51 (2017).
18. O. L. Haidamak, V. A. Matviychuk, and Y. S. Kucherenko, *Technology, Energy, Transport of Agricultural Industry*, **2**(109): 105 (2019).

Засновник: Національна академія наук України, Інститут металофізики ім. Г. В. Курдюмова НАН України
Видавець: ВД «Академперіодика» НАН України
Передплатний індекс/Subscription index: 74312 ISSN 1024-1809

Інформація для передплатників журналу «МЕТАЛОФІЗИКА ТА НОВІТНІ ТЕХНОЛОГІЇ»

Редакція журналу МфНТ повідомляє читачів про передплату (що починається з будь-якого місяця випуску). Журнал МфНТ входить за індексом **74312** до «Каталогу видань України». Рекомендуємо оформити передплату:

1) через ТОВ **«ПресЦентр Київ»** / LLC **'PresCentr Kyiv'** / (01019 Київ, Україна, а/с 185, тел./факс: +380 44 5361180 / +380 44 5361175, e-mails: podpiska1@prescentr.kiev.ua, market7@prescentr.kiev.ua, ksl1@prescentr.kiev.ua) чи то через Internet:

http://www.prescentr.kiev.ua/index.php?route=product/category&path=332_252_266;

2) через передплатну аґенцію «Меркурій» / Subscription agency 'Mercury' (49000 Дніпро, Слобожанський проспект, буд. 10, корп. 2, кв. 51; 03056 Київ, вул. Вадима Гетьмана, буд. 27, оф. 74, тел.: +380 93 3935740 / +380 44 2210557, e-mails: podpiska@mercury.net.ua, l.podbereznaja.mercury@gmail.com);

3) безпосереднім перерахуванням від **170 грн.** за один випуск до **2040 грн.** за один том (12 випусків за рік):

«отримувачу»: Інститут металофізики ім. Г. В. Курдюмова НАН України
на розрахунковий рахунок № UA058201720313291001201001901 в банку ГУДКСУ в м. Києві
Код банку: 820172
Код єдиного державного реєстру підприємств і організацій України (ЄДРПОУ): 05417331
Для «Постачальника» — Інституту металофізики ім. Г. В. Курдюмова НАН України
Свідоцтво платника податку на додану вартість (ПДВ) № 36283185, індивідуальний податковий номер (ІПН) 054173326066
Код призначення платежу: 25010100
призначення платежу: за журнал «Металофізика та новітні технології» (том(и), номер(и), рік(роки)) для РВВ ІМФ НАНУ
підстава: передоплата 100%.

INFORMATION FOR FOREIGN SUBSCRIBERS

Editorial Board of a Monthly Research Journal 'Metallophysics and Advanced Technologies' (transliteration: **'Metallofizika i Noveishie Tekhnologii')** (CODEN: MNTEEU; ISSN: 1024-1809) advertises the subscription on an annual basis. Orders should be placed through one of the methods described below. Besides the subscription *via* the LLC **'PresCentr Kyiv' / «ПресЦентр Київ»** (with address: UA-01019 Kyiv, Ukraine, P.B. 185, tel./fax: +380 44 5361180 / +380 44 5361175, e-mails: podpiska1@prescentr.kiev.ua, market7@prescentr.kiev.ua, ksl1@prescentr.kiev.ua) or *via* Internet:

http://www.prescentr.kiev.ua/index.php?route=product/category&path=332_252_266,

as well as besides the subscription *via* Subscription agency 'Mercury' / «Меркурій» (with juridical address: UA-49000 Dnipro, Slobozhansky Ave., Bldg. 10/2, apt. 51, postal address in Kyiv: UA-03056 Kyiv, Vadym Hetman Str., Bldg. 27, off. 74, tel.: +380 93 3935740 / +380 44 2210557, e-mails: podpiska@mercury.net.ua, l.podbereznaja.mercury@gmail.com), the Editorial Board will take orders sent directly to the Editorial Board. To obtain our journal, the persons and institutions, interested in this title, should made the definite payment sent, according to the order, to the account of the Publisher—G. V. Kurdyumov Institute for Metal Physics of the N.A.S. of Ukraine.

The journal frequency is 12 issues per year. The annual subscription rate for 'Metallophysics and Advanced Technologies' is 156 USD (or 132 EUR), including airmail postage, packing and handling charges. All other-currency payments should be made using the current conversion rate set by the Publisher (subscribers should contact the Editorial Board).

Subscription is valid after obtaining by the Editorial Board of banker's order. Banker's order should be sent to the address:

G. V. Kurdyumov Institute for Metal Physics, N.A.S. of Ukraine,
currency account No. UA603223130000025308000000067, MFO 322313,
in the Kyiv's Branch of JSC 'The State Export-Import Bank of Ukraine' (Public Joint Stock Company 'Ukreximbank') (11^{b} Bulvarno-Kudryavska Str., UA-04053 Kyiv, Ukraine)
simultaneously with written notice providing the Editorial Board with a copy of banker's order for subscription and detailed address for mailing.

Prepayment is 100%.

Address of the Editorial Board: G. V. Kurdyumov Institute for Metal Physics, N.A.S. of Ukraine, 36 Academician Vernadsky Blvd., UA-03142 Kyiv, Ukraine.
E-mail: mfint@imp.kiev.ua (with subject beginning by word 'mfint')
Fax: +380 44 4242561. Phone: +380 44 4249042, +380 44 4241221.

After receiving of banker's order, the Editorial Board will send the guarantee letter to the subscriber's address for mailing the journal for a corresponding term.

The Editorial Board of this journal hopes for effective co-operation with its present and future readers and requests to promote the maximum information about its contents to persons and organizations concerned.

Індекс 74312

ISSN 1024-1809. Metallophys. Adv. Technol. (Металофіз. новітні технол.; Metallofiz. Noveishie Tekhnol.), Vol. 47, No. 6 (2025)